



UNIVERSITÉ CATHOLIQUE DE LOUVAIN

École Polytechnique de Louvain

ICTEAM Institute

Antenna Group

Louvain-la-Neuve, Belgium

**Beam-Shaping Antenna Arrays for 5G Communication
System and Automotive Radar**

Husnain Ali KAYANI

Thesis presented for the Ph.D. degree in Engineering Sciences

Examining Committee

Advisor: Christophe CRAEYE, UCLouvain, Belgium

Jury: Danielle VANHOENACKER-JANVIER, UCLouvain, Belgium

Isabelle HUYNEN, UCLouvain, Belgium

Hendrik ROGIER, Ghent University, Belgium

Benoit POUSSOT, Université Paris-Est Marne-la-Vallée, France

Secretary: Denis FLANDRE, UCLouvain, Belgium

President: Jean-Pierre RASKIN, UCLouvain, Belgium

July 9, 2020

“The important thing is not to stop questioning. Curiosity has its own reason of existing.”

Albert Einstein

*To
My Parents and Siblings
For their everlasting love and unwavering support.*

“Run from what’s comfortable. Forget safety. Live where you fear to live.
Destroy your reputation. Be notorious.”

Rumi

Acknowledgements

First and foremost, I would like to extend my sincere gratitude to my thesis advisor, Prof. Christophe Craeye, for supervising me, and proposing exciting projects to work on. I greatly appreciate his enthusiasm, patience and relentless support in my doctoral journey. I could not have imagined having a better advisor and mentor for my Ph.D study. I am grateful to Prof. Danielle Vanhoenacker-Janvier and Prof. Denis Flandre for their guidance and advice. I also appreciate the comments from the other members of my doctoral examination committee, Prof. Isabelle Huynen, Prof. Hendrik Rogier, Prof. Benoit Poussot, and Prof. Jean-Pierre Raskin to improve this manuscript.

My appreciation also extends to my colleagues at UCLouvain for their support in this long incredible journey. I have learnt a great deal from them and shared wonderful moments as well. I always cherish our intriguing and thought-provoking discussions during the coffee breaks. I would like to thank Sumit Karki and Donia Oueslati for providing friendly and supportive environment in the office. I am extremely grateful to Quentin Guening, Khaldoun Alkhalifeh and Nicolas Goreux for their valuable contributions in different projects. I appreciate Thomas Pairon and Thomas Feuillen for their help with radars. I really want to thank Bui Van Ha, Denis Tihon, Modeste Bodehou, Inès Adouani and Jean Cavillot for their scientific collaborations. I would also like to thank Jose Ignacio Echeveste,

Rajkumar Jaiswar, Julian David and Kashif Nawaz for our discussions on different socio-political topics, Christopher Raucy for organizing different activities in the group and Maxime Drouguet for his advices in fabrication processes. I am also thankful to François Hubin and Brigitte Dupont for entertaining my requests related to different software packages and computing resources. I am really grateful to Pascal Simon for training me and providing support in RF and antenna measurements. I would like to thank Souley Djadjandi, David Spote and Benoît Hubert for tolerating my excessive requests related to fabrication and measurements. I appreciate the administrative support provided by Isabelle Dargent, Christel Derzelle, Viviane Sauvage and Marie-Christine Vandingenen.

Last but not least, I am indebted to my family for their love, sacrifice, and support. I would like to thank my father for inciting curiosity in me, my mother for inculcating in me her values, and my grandfather for shaping my personality. I would also like to thank my brothers Ahmed and Khubaib, and my sister Zoha for their moral support and care for me.

Abstract

The antenna systems are integral part of any wireless of communication system and they also impact the system's performance parameters, such as range, data rate, mobility, coverage, cost etc. In order to improve the performance of a wireless communication system, beam-shaping antenna arrays can be exploited. A beam-shaping antenna array is an antenna system in which the antenna's beam (radiation pattern) can be modified electronically.

Parasitic antenna arrays are one of the antenna systems which could be employed for beam-shaping in modern wireless communication systems. A parasitic antenna array or Electronically Steerable Parasitic Array Radiator (ESPAR) consists of one or few driven antennas and multiple parasitic elements with tunable impedance attached to their terminal. A strong mutual coupling exists between the radiating and parasitic elements. By varying the tunable impedances the antenna's total radiation pattern can be shaped electronically. In contrast to phased arrays, parasitic antenna arrays require inexpensive hardware to adapt the radiation pattern. However, a parasitic antenna array entails the design and computational challenges, which involve the computation of impedances attached to the parasitic elements to form a desired radiation pattern. In this thesis, an efficient spectral optimization method has been proposed to overcome the computational challenges of a parasitic array design. In this context, an attempt has been made also to analytically determine the tunable impedances to shape the different

beams. A beam-shaping parasitic antenna array has been designed for the base station of a 4G or 5G mobile communication system and the coverage has been improved in a given area by adapting the radiation pattern of a base station. A varactor diode has been utilized to design a tunable impedance circuit and a small prototype has been made to electronically adapt the radiation pattern.

The leaky waves can be excited in a planar structure to enhance the antenna gain. Therefore, a Fabry-Perot Cavity (FPC) based antenna is designed, which consists of a Partially Reflecting Surface (PRS) placed on top of a radiating element backed by a ground plane. A PRS layer is designed with a superstrate and array of parasitic elements. Although it is a leaky-wave antenna because PRS layer suppresses surface waves, it is also a printed parasitic antenna array. A strong mutual coupling exists between the radiating and parasitic elements. The parasitic elements of a PRS layer are connected with each other through dynamic loads, by tuning the loads different surface impedances exist on different parts of parasitic layer and hence beamforming is implemented. A printed ESPAR antenna based on a FPC has been designed for a radar application. It can steer the beam while maintaining a high gain.

Contents

Acknowledgements	iii
Abstract	v
Table of Contents	vii
List of Figures	xi
List of Tables	xix
Acronyms	xxi
1 Introduction	1
1.1 Principles of Beam-Shaping Antenna Arrays	3
1.1.1 Phased Arrays	3
1.1.2 Parasitic Antenna Arrays or Electronically Steerable Parasitic Array Radiator (ESPAR)	4
1.1.3 Fabry-Perot Cavity Based Antenna Array	6
1.2 Applications of Beam-Shaping Antenna Arrays	8
1.2.1 Beam-Shaping Parasitic Antenna Arrays for a Cellular Communication System	8

1.2.2	Beamforming Antenna Array for the Automotive Radar	11
1.3	Objectives and Novelties of the Thesis	11
1.4	Design Tools	12
1.5	Outline of the Thesis	13
2	Electromagnetic Model and Computation of Parasitic Loads in a Parasitic Antenna Array	15
2.1	Introduction	16
2.2	Open-Circuit To Embedded Pattern Approach	17
2.3	Simulations	19
2.4	Analytical Solution	22
2.5	Spectral Optimization	29
2.5.1	Harmonic Basis	29
2.5.2	Gaussian Basis	30
2.5.3	Comparison of Spectral Optimization with Genetic Algorithm	31
2.6	Conclusion	37
3	Parasitic Antenna Array	39
3.1	Introduction	40
3.2	Methodology	41
3.3	Objective Radiation Patterns	43
3.4	Parasitic Antenna Array	45
3.4.1	Driven Antennas of the Parasitic Antenna Array	45
3.4.2	Design of Parasitic Elements of the Parasitic Antenna Array	46
3.4.3	Electromagnetic Model for the Simulations	48
3.4.4	Computation of the Parasitic Loads	50
3.4.5	Simulation Results of the Parasitic Antenna Array	51
3.4.6	Realization of the Parasitic Radiators with Loads	60
3.4.7	Measurement Results of the Parasitic Antenna Array	61

3.5	Improved Coverage Results with Optimized Base Station . . .	69
3.6	Conclusion	74
4	Electronically Steerable Parasitic Array Radiator (ESPAR)	
	Antenna	75
4.1	Introduction	76
4.2	Varactor Diodes	78
4.2.1	Characterization of Varactor diodes and tunable impedance circuit	78
4.2.2	Characterization using microstrip test fixture	79
4.3	ESPAR Antenna for Cellular Communication	84
4.3.1	Driven antenna	86
4.3.2	ESPAR antenna	87
4.4	ESPAR Antenna for a Radar	98
4.4.1	Design of an ESPAR antenna	99
4.4.2	EM Model and Optimization	102
4.4.3	Simulation Results	104
4.5	Conclusion	118
5	Antenna Array for the Automotive Radar	119
6	Conclusions and Future Works	121
6.1	Conclusions	121
6.2	Future Works	123
A	Green's Functions in Layered Substrates	125
A.1	Introduction	125
A.2	Spectral analysis	126
A.3	Plane wave propagation	127
A.3.1	Definitions	127
A.3.2	Reflection coefficients at a single interface	130
A.3.3	Reflection coefficients on multiple interfaces	132

A.3.4	Propagation of plane waves in a multilayer slab	135
A.3.5	Waves emitted by a monotonic current sheet	137
A.3.5.1	On a single interface	138
A.3.5.2	In a multilayered medium	139
A.4	Green's functions in the spectral domain	140
A.4.1	Interaction on the same layer	141
A.4.2	Special cases	142
A.4.2.1	Homogeneous medium	142
A.4.2.2	Single layer substrate	142
B	Working Principle of the Antenna for the Automotive Radar	145
C	List of Publications and Research Talk	147
	Bibliography	157

List of Figures

1.1	Active Electronically Scanned Array (AESA) on an aircraft radar [1].	3
1.2	Phased arrays architecture: (a) Analog beam forming (b) Digital beam forming.	4
1.3	Parasitic antenna array or ESPAR antenna.	5
1.4	Schematic of an FPC based antenna using PRS layer.	7
1.5	Configuration of sector antennas for cellular communication [2].	9
1.6	Radiation pattern of Kathrein antenna [3].	9
2.1	Parasitic antenna array using bow-tie antenna.	19
2.2	E-field radiation pattern of parasitic antenna array with open-circuited parasitics at 1800 MHz.	20
2.3	E-field radiation pattern of parasitic array with short-circuited parasitics at 1800 MHz.	21
2.4	Circular array of seven dipoles.	23
2.5	Circular array of seven dipoles (Top view).	24

2.6	Comparison of different objective power patterns and the obtained power patterns from the ESPAR with complex and reactive loads, using analytical method, Frequency=1800 MHz, Phi [degrees] vs Linear Scale, (a) case I (0° tilt) (b) case II (15° tilt) (c) case III (30° tilt) (d) case IV (45° tilt).	26
2.7	Comparison of different objective power patterns (different phase) and the obtained power patterns from the ESPAR with reactive loads, using analytical method, Frequency=1800 MHz, Phi [degrees] vs Linear Scale, (a) case I (0° tilt) (b) case II (15° tilt) (c) case III (30° tilt) (d) case IV (45° tilt).	27
2.8	Graphical representation of harmonic basis.	30
2.9	Graphical representation of Gaussian basis.	31
2.10	(a) ESPAR antenna with cross dipole (active element) and half-wavelength dipoles (parasitic elements) (b) Top view. . .	32
2.11	Different objective power patterns and the obtained power patterns from the parasitic antenna array using spectral optimization and genetic algorithm, Frequency=1800 MHz, Phi [degrees] vs Linear Scale, (a) case I (0° tilt) (b) case II (22° tilt) (c) case III (30° tilt) (d) case IV (-14° tilt).	36
2.11	Different objective power patterns and the obtained power patterns from the parasitic antenna array using spectral optimization and genetic algorithm, Frequency=1800 MHz, Phi [degrees] vs Linear Scale, (e) case V (-18° tilt) (f) case VI (multi-beam).	37
3.1	Flow chart illustrating the proposed methodology to improve the coverage in a cellular communication by utilizing parasitic antenna array.	42
3.2	Parasitic antenna array design for base station: side view. . .	46
3.3	Parasitic antenna array design for base station: interior front view.	47
3.4	Parasitic antenna array design for base station: interior front view.	47

3.5	Parasitic antenna array design for base station: top view. . .	48
3.6	Base station antenna for a sector in a cellular communication [3].	51
3.7	3D Radiation pattern of base station antenna, Frequency=1800 MHz (MoM simulation).	52
3.8	Azimuthal power pattern of base station antenna, Frequency=1800 MHz (MoM simulation vs measurement).	53
3.9	(a) Base station antenna [3] and printed parasitic dipoles on a substrate with loads. (b) Interior front of printed parasitic dipoles on a substrate with loads.	54
3.10	(a) Fabricated prototype consisting of printed dipole on I-Tera with capacitors or inductors, the frame is made of AM50C material (b) Zoom view.	54
3.11	Azimuth power pattern of the parasitic antenna array for a certain set of loads with and without dielectric, MoM simulation, Frequency=1800 MHz.	55
3.12	Azimuthal objective power pattern and obtained simulated (MoM) power pattern from the parasitic antenna array, Case I, Frequency=1800 MHz.	56
3.13	Azimuthal objective power pattern and obtained simulated (MoM) power pattern from the parasitic antenna array, Case II, Frequency=1800 MHz.	57
3.14	Azimuthal objective power pattern and obtained simulated (MoM) power pattern from the parasitic antenna array, Case III, Frequency=1800 MHz.	58
3.15	Measurement set-up of the parasitic antenna array.	61
3.16	Schematic figure of the measurement set-up.	62
3.17	Comparison of azimuthal objective power pattern, obtained simulated (MoM, CST) and measured power patterns from the parasitic antenna array, Case I, Frequency=1800 MHz. . .	62

3.18	Comparison of azimuthal objective power pattern, obtained simulated (MoM, CST) and measured power patterns from the parasitic antenna array, Case II, Frequency=1800 MHz.	63
3.19	Comparison of azimuthal objective power pattern, obtained simulated (MoM, CST) and measured power patterns from the parasitic antenna array, Case III, Frequency=1800 MHz.	64
3.20	Variation of measured azimuthal power pattern of the parasitic antenna array versus frequency, Case I.	66
3.21	Variation of measured azimuthal power pattern of the parasitic antenna array versus frequency, Case II.	67
3.22	Variation of measured azimuthal power pattern of the parasitic antenna array versus frequency, Case III.	68
3.23	Measured reflection coefficient of BS antenna: isolated and with parasitic elements.	68
3.24	Geometry of the scenario with buildings (grey) and two base stations (blue dots-arrows) (a) Top view (b) Side view.	70
3.25	Azimuthal BS power pattern vs adapted BS power patterns (MoM) with parasitic elements, BS 1 and BS 2 are from Fig. 3.24, Frequency=1800 MHz.	71
3.26	Ray-tracing simulation of the amplitude of the electric field in dB μ V/m with the BS patterns (without parasitic elements).	72
3.27	Ray-tracing simulation of the amplitude of the electric field in dB μ V/m with the adapted BS patterns with parasitic elements.	72
3.28	CDF of the field level from BS antenna and from BS antenna with parasitic elements for BS 1.	73
3.29	CDF of the field level from BS antenna and from BS antenna with parasitic elements for BS 2.	73
4.1	Varactor capacitance vs biasing voltage [4].	78
4.2	Tunable variable impedance circuit.	79
4.3	50 Ω microstrip transmission line feeding to the varactor.	80

4.4	50 Ω microstrip transmission line feeding to the tunable impedance circuit.	81
4.5	Equivalent transmission-line model of the microstrip circuit used for the characterization of varactor diode and tunable impedance circuit.	81
4.6	Fringe capacitance at the open end of transmission line.	82
4.7	PCB of tunable impedance circuit used for characterization.	83
4.8	Measurement set-up using microstrip test fixture.	84
4.9	Measured impedance of varactor at 1800 MHz.	85
4.10	Measured impedance of tunable impedance circuit at 1800 MHz.	85
4.11	Driven antenna of ESPAR with a delta-gap feed (front view).	86
4.12	Reflection coefficient of the driven antenna with a delta-gap feed (CST simulation).	87
4.13	The balun feed from coax cable to the cross dipole antenna.	88
4.14	Reflection coefficient of the driven antenna with balun and coax feed (CST simulation).	88
4.15	Azimuthal power pattern of the driven antenna, Frequency=1800 MHz (CST simulation vs measurement).	89
4.16	(a) Parasitic radiators with a biasing circuitry (b) zoom version.	90
4.17	ESPAR antenna (Front view).	91
4.18	ESPAR antenna (Interior view).	92
4.19	Fabricated ESPAR antenna.	94
4.20	Experimental set up of the ESPAR antenna.	95
4.21	Comparison of azimuthal objective power pattern, obtained simulated (MoM) and measured power patterns from the ESAPR antenna, Case I, Frequency=1800 MHz.	96
4.22	Comparison of azimuthal objective power pattern, obtained simulated (MoM) and measured power pattern from the ESAPR antenna, Case II, Frequency=1800 MHz.	97
4.23	Measured reflection coefficient of Test Antenna, ESPAR antenna Case I and ESPAR antenna Case II.	98

4.24	3D figure of the printed ESPAR antenna designed at 24.125 GHz.	100
4.25	Cross section of the printed ESPAR antenna.	100
4.26	Active layer of the printed ESPAR antenna.	101
4.27	Parasitic layer of the printed ESPAR antenna.	101
4.28	Biasing of tunable impedance circuit for the printed ESPAR antenna.	102
4.29	Directivity pattern of the printed ESPAR antenna without any tunable reactive elements, H-Plane $\Phi = 0^\circ$, Method of moments (MoM) vs IE3D simulations at 24.5 GHz.	105
4.30	Directivity pattern of the printed ESPAR antenna without any tunable reactive elements, E-Plane $\Phi = 90^\circ$, Method of moments (MoM) vs IE3D simulations at 24.5 GHz.	105
4.31	3D radiation pattern of the printed ESPAR antenna, Beam scanned at $\theta = 0^\circ$, $\Phi = 0^\circ$, Method of moments (MoM) simulation at 24.5 GHz.	106
4.32	Directivity of the printed ESPAR antenna, Beam scanned at $\theta = 0^\circ$, H-Plane $\Phi = 0^\circ$, Method of moments (MoM) simulation at 24.5 GHz.	107
4.33	Directivity of the printed ESPAR antenna, Beam scanned at $\theta = 0^\circ$, E-Plane $\Phi = 90^\circ$, Method of moments (MoM) simulation at 24.5 GHz.	107
4.34	Directivity of the printed ESPAR antenna, Beam scanned at $\theta = 0^\circ$, H-Plane $\Phi = 0^\circ$, Method of moments (MoM) simulation at 24.5 GHz vs IE3D Simulation at 24.7 GHz. . .	108
4.35	3D radiation pattern of the printed ESPAR antenna, Beam scanned at $\theta = 4.5^\circ$, $\Phi = 0^\circ$, Method of moments (MoM) simulation at 24.5 GHz.	109
4.36	Directivity of the printed ESPAR antenna, Beam scanned at $\theta = \pm 4.5^\circ$, H-Plane $\Phi = 0^\circ$, Method of moments (MoM) simulation at 24.5 GHz.	110

4.37	Directivity of the printed ESPAR antenna, Beam scanned at $\theta = 4.5^\circ$, H-Plane $\Phi = 0^\circ$, Method of moments (MoM) simulation at 24.5 GHz vs IE3D Simulation at 24.7 GHz.	111
4.38	3D radiation pattern of the printed ESPAR antenna, Beam scanned at $\theta = 9^\circ$, $\Phi = 0^\circ$, Method of moments (MoM) simulation at 24.5 GHz.	111
4.39	Directivity of the printed ESPAR antenna, Beam scanned at $\theta = \pm 9^\circ$, H-Plane $\Phi = 0^\circ$, Method of moments (MoM) simulation at 24.5 GHz.	112
4.40	Directivity of the printed ESPAR antenna, Beam scanned at $\theta = 9^\circ$, H-Plane $\Phi = 0^\circ$, Method of moments (MoM) simulation at 24.5 GHz vs IE3D Simulation at 24.7 GHz.	112
4.41	Reflection coefficient (S_{11}) vs frequency for beams scanned at $\theta = 0^\circ$, $\theta = 4.5^\circ$ and $\theta = 9^\circ$, Method of moments (MoM) simulation.	113
4.42	Maximum directivity vs frequency for beams scanned at $\theta = 0^\circ$, $\theta = 4.5^\circ$ and $\theta = 9^\circ$, Method of moments (MoM) simulation.	113
4.43	Side lobe level (SLL) vs frequency for beams scanned at $\theta = 0^\circ$, $\theta = 4.5^\circ$ and $\theta = 9^\circ$, Method of moments (MoM) simulation.	114
4.44	Gain comparison of the printed ESPAR antenna, Beams scanned at $\theta = 0^\circ$, $\theta = 4.5^\circ$, $\theta = 9^\circ$, H-Plane $\Phi = 0^\circ$, Method of moments (MoM) simulation at 24.5 GHz.	116
A.1	Representation of the vector basis for the representation of plane waves in layered media.	129
A.2	Defintion and notation of reflection coefficients in terms of upward and downward plane waves accross a single interface.	130
A.3	Definition and numbering of the reflection coefficients in multilayer media.	132
A.4	Electric field translation in a multilayer medium.	136

A.5 Structure of the single layer substrate. The perfect electric conductors are marked with thick black lines. 143

List of Tables

2.1	Computation Time Comparison.	20
2.2	Complex loads computed for different radiation patterns, using the analytical method.	24
2.3	Reactive loads computed for different radiation patterns, using the analytical method.	25
2.4	Impedances computed for different radiation patterns by using spectral optimization with harmonic basis.	33
2.5	Impedances computed for different radiation patterns by using spectral optimization with Gaussian basis.	33
2.6	Genetic algorithm parameters [5].	34
2.7	Comparison of figure of merits of harmonic optimization with genetic algorithm.	35
3.1	Parasitic reactances computed using harmonic optimization for the Case I radiation pattern shown in Fig. 3.12.	59
3.2	Parasitic reactances computed using harmonic optimization for the Case II radiation pattern shown in 3.13.	59
3.3	Parasitic reactances computed using harmonic optimization for the Case III radiation pattern shown in Fig. 3.14.	60

3.4	Maximum gain and efficiency of the BS antenna with and without the parasitic elements, MoM simulation at 1800 MHz.	60
3.5	Maximum gain of the BS antenna with and without the parasitic elements, measured at 1800 MHz.	65
4.1	Parasitic reactances and DC biases for radiation pattern of ESPAR antenna prototype, Case I shown in Fig. 4.21.	90
4.2	Parasitic reactances and DC biases for radiation pattern of ESPAR antenna prototype, Case II shown in Fig. 4.22.	93
4.3	Maximum gain and efficiency of the test antenna with and without the parasitic elements, MoM simulation at 1800 MHz.	93
4.4	Maximum gain of the test antenna with and without the parasitic elements, measured at 1800 MHz.	93
4.5	Genetic algorithm parameters.	103
4.6	Parasitic loads for different beam scan angles.	106
4.7	Radiation parameters for different beam scan angles.	106
4.8	Parasitic loads for different beam scan angles, considering dielectric and varactor ohmic losses.	115
4.9	Radiation parameters for different beam scan angles, considering dielectric and varactor ohmic losses.	115
4.10	Comparison of the parameters of the designed ESPAR antenna with the similar antennas presented in the literature.	117

Acronyms

3D	Three Dimension
4G	Fourth Generation
5G	Fifth Generation
ADS	Advanced Design System
AESA	Active Electronically Scanned Array
AoA	Angle of Arrival
BPM	Binary Phase Modulation
BRIC	Brussels Regional Informatics Center
BS	Base Station
CDF	Cumulative Distribution Function
CST	Computer Simulation Technology
DAC	Digital-to-Analog Converter
DC	Direct Current
DSP	Digital Signal Processor
DUT	Device Under Test
EBG	Electromagnetic Band Gap
EM	Electromagnetic
ESPAR	Electronically Steerable Parasitic Array Radiator
FFT	Fast Fourier Transform
FIT	Finite Integration Technique
FMCW	Frequency-Modulated Continuous-Wave

FPC	Fabry-Perot Cavity
FSS	Frequency Selective Surface
GPS	Global Positioning System
HIEM	High Impedance Electromagnetic Surface
HPBW	Half Power Beam Width
ICNIRP	International Commission on Non-Ionizing Radiation Protection
IE3D	Integral Equation Three-Dimensional
IFA	Inverted-F Antenna
IoT	Internet of Things
LIDAR	Laser Identification Detection And Ranging
LNA	Low Noise Amplifier
LTE	Long-Term Evolution
MBF	Macro Basis Function
MIMO	Multiple-Input-Multiple-Output
MMIC	Monolithic Microwave Integrated Circuit
PA	Power Amplifier
PCB	Printed Circuit Board
PRS	Partially Reflecting Surface
RADAR	Radio Detection And Ranging
RAM	Random Access Memory
RF	Radio Frequency
Rx	Receive
SDR	Semi Definite Relaxation
SIMO	Single-Input-Multiple-Output
SLL	Side lobe level
SNR	Signal-to-noise Ratio
SRF	Self Resonance Frequency
TD	Time Domain
TDM	Time Division Multiplexing
Tx	Transmit
VNA	Vector Network Analyzer
WHO	World Health Organization
WLAN	Wireless Local Area Network

CHAPTER 1

Introduction

This introductory chapter discusses the motivation and structure behind this thesis work. The essence of this work deals with the design of beam-shaping antenna arrays for different wireless communication applications.

Nowadays, we are surrounded by wireless devices such as smart phones, laptops, television, wireless sensors, Global Positioning System (GPS) etc.; that means antennas have become an important component of our environment. Moreover antenna systems are being used in different walks of life, like remote sensing, radio astronomy, satellite communication, RADARs (Radio Detection And Ranging) and defence applications. In the future, antenna systems would be used in health care systems, Internet of Things (IoT), autonomous vehicles, vehicle-to-vehicle and vehicle-to-infrastructure communication systems. Therefore, there is a dire need to develop and optimize new antenna technologies, suitable for new applications and improving the performance of existing systems.

The antennas form an integral part of any wireless communication system. Wireless devices communicate with each other through Electromagnetic (EM) waves, transmitted and received by antennas. The antenna's performance parameters are critical to the performance of any wireless communication system, i.e. range, data rate, mobility, coverage, cost etc. The

required performance parameters of an antenna system are dependent on the application. Every application brings its own design challenges for its antenna system.

Over the past few decades, the use of antenna arrays (more than one antenna) for transmitting or receiving the information have received quite some attention. It has resulted into the development of antenna arrays for defence and space-borne applications. In recent years, due to high demands of data rate, better mobility and improved coverage, antenna arrays are finding their ways into modern mobile communication systems as well. A beam-shaping antenna array is an antenna system in which the antenna's beam (radiation pattern) can be modified electronically. Such antenna arrays are getting popular these days as they improve the coverage and data rate in mobile communication applications by adapting the beam according to the changing environment. Antenna array's radiation pattern can be modified to serve a certain area or specific users and follow them as they move. It would ensure a high performance communication even in a high mobile condition. Similarly, if a certain part of an area does not have a good coverage due to its terrain or surrounding buildings, a coverage can be improved by adapting the radiation pattern of antenna array. In radar applications, beam-agile antenna arrays bring many advantages for instance they are not required to be rotated mechanically, they have faster response time and better performance as compared to mechanically rotated radars. In the framework of this thesis, different types of beam-shaping antenna arrays have been studied, designed and tested for different applications.

In this chapter, first I will discuss the principles, literature review and challenges regarding the beam-shaping antenna arrays, employed in this thesis. Secondly, I will give a brief summary and literature review of the beam-shaping antenna arrays from the applications perspective i.e. 5G communication system and automotive radar. Moreover, I will shed some light on the constraints and design challenges of the respective antennas for the concerned applications.



Figure 1.1: Active Electronically Scanned Array (AESA) on an aircraft radar [1].

1.1 Principles of Beam-Shaping Antenna Arrays

1.1.1 Phased Arrays

Phased arrays consist of multiple antennas, each antenna transmits or receives signals. By manipulating the gain and phase shift of each antenna different beam shapes can be formed. A good performance can be achieved by phased arrays in terms of gain, side lobe level (SLL) suppression, bandwidth and beam control [6], because the amplitude and phase of the signal of each antenna can be controlled independently. Phased array systems have been in use in space and defence applications for many years. The Active Electronically Scanned Array (AESA) as shown in Fig.1.1 is used in modern combat aircraft.

Phased arrays can be divided into two categories, i.e. analog beamforming and digital beamforming phased arrays, as shown in Fig. 1.2. Both technologies can be used at transmitter or receiver to manipulate the shape of the radiation pattern of an antenna array. In analog phased arrays, high quality (broadband, accurate and high linearity) phase shifters, Power Amplifiers (PA) and Low Noise Amplifiers (LNA) are required for each antenna element. Similarly, each antenna element in digital phased arrays requires dedicated transceiver modules with PA, LNA along with a large bandwidth

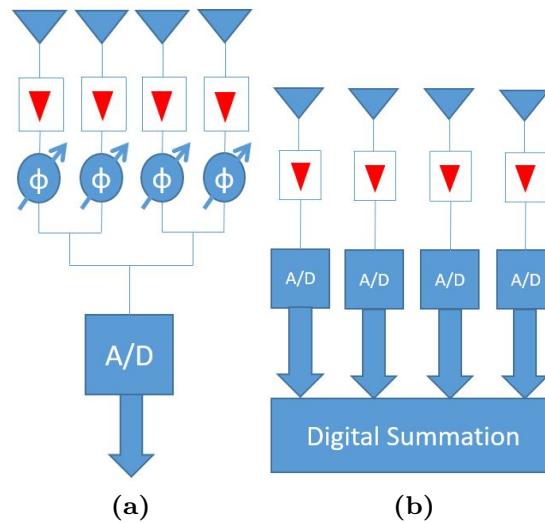


Figure 1.2: Phased arrays architecture: (a) Analog beam forming (b) Digital beam forming.

Digital Signal Processor (DSP). Therefore, in both cases phased arrays require each antenna element to have a dedicated active radio frequency (RF) circuitry, which makes it a very expensive technology to be employed in commercial civilian applications.

1.1.2 Parasitic Antenna Arrays or Electronically Steerable Parasitic Array Radiator (ESPAR)

A parasitic antenna array consists of one or few driven antennas, and mostly parasitic elements with tunable impedances (loads), as shown in Fig. 1.3. By varying the impedances, the radiation pattern of a parasitic antenna array can be manipulated [7], [8]. In a parasitic antenna array, all antennas are placed in close proximity to each other in order to have a stronger mutual coupling. Mutual coupling is the electromagnetic interaction between antenna elements in an array. Such interaction induces currents on parasitic elements which are not excited directly. In a simple configuration, analytical methods can be used to estimate the induced currents but in general, numerical methods are needed. The impact of mutual coupling on a radiation pattern can be varied by tuning the variable loads, it induces different current distributions on driven and parasitic elements and thus, different

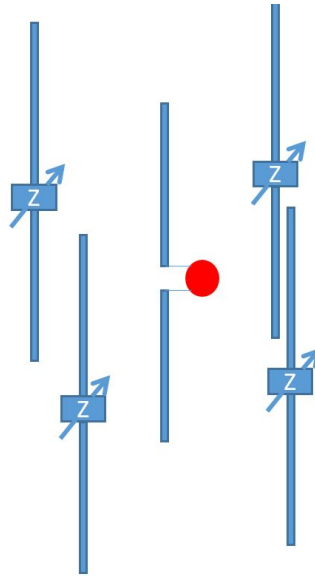


Figure 1.3: Parasitic antenna array or ESPAR antenna.

radiation patterns can be obtained.

Parasitic antenna arrays tend to be much cheaper than phased arrays, since they do not require expensive dedicated RF circuitry for each antenna element. Instead, they require less expensive tunable impedance circuitry for parasitic elements to carry out beam-shaping. It makes the parasitic antenna array a strong candidate for beam-shaping applications.

An Electronically Steerable Parasitic Array Radiator (ESPAR) is a parasitic antenna array in which variable impedances (loads) attached to the parasitic elements are tuned electronically to carry out beam-shaping [8]. An ESPAR antenna can be used to provide reconfigurability in terms of resonance frequency, polarization and radiation pattern [9]. PIN diodes [10], [11] or varactor diodes [8], [12] can be used as tunable impedances. PIN diodes provide only open (OFF) and short (ON) circuit impedances, while varactor diodes provide variable capacitive impedances. Therefore, the use of varactor diodes provides more degrees of freedom to shape the beam but it entails biasing and control challenges as well. Phased array theory cannot be applied directly to the parasitic antenna array since the loads are directly attached to the parasitic elements, which hence do not benefit from independent signal control. A previous approach to analyse parasitic antenna

arrays consisted of modelling the currents on all antennas as a function of the loads attached to the parasitic elements. However such a model, expressed in [8], [13], only holds for single-mode antennas, i.e. antennas for which the current distributions may be considered constant, within a multiplying factor [14], [15]. Only few antenna types satisfy this condition, for instance thin dipole antennas, except when placed in very dense arrays (spacing less than about $\lambda/4$). In [16] the developed array model works in agreement with the Method of Moments (MoM) simulations but the array model is specific to the IFA antenna array and cannot be applied to other types of antennas. Another approach could consist of performing the full-wave simulations in conjunction with the optimization algorithm [10] to find the optimized loads. In [17], at each iteration of the optimization the radiation pattern is represented by a quadratic approximation. The full-wave simulation for different combinations of loads makes the optimization process very time consuming. The use of open-circuit patterns in the calculation of total radiation pattern of parasitic antenna array, includes all the effects mutual coupling [7], [18], [19] and does not entail any underlying approximation. Moreover, this approach avoids launching full-wave simulations at each iteration and therefore it is computationally efficient. Hence, in this thesis, the open-circuit patterns are used to compute the parasitic antenna array radiation pattern efficiently.

1.1.3 Fabry-Perot Cavity Based Antenna Array

The use of leaky-wave antennas to enhance the gain is widely known. The weakly attenuated leaky waves are excited in a planar structure which leads to the enhancement of the gain at broadside [20], [21], [22]. For that purpose, various configurations have been employed, such as single or multi-dielectric layers are used on top of a radiator to create a resonance cavity, called Fabry-Perot Cavity (FPC). Such a resonance cavity is formed by placing a Partially Reflective Surface (PRS) on top of a radiator backed by a ground plane, with a spacing between the ground plane and the top layer [23], [24]. PRS can be formed by stacking quarter-wavelength dielectrics of high and low permittivity [20], [21], [22] or with a periodic screen [25]. PRS can also

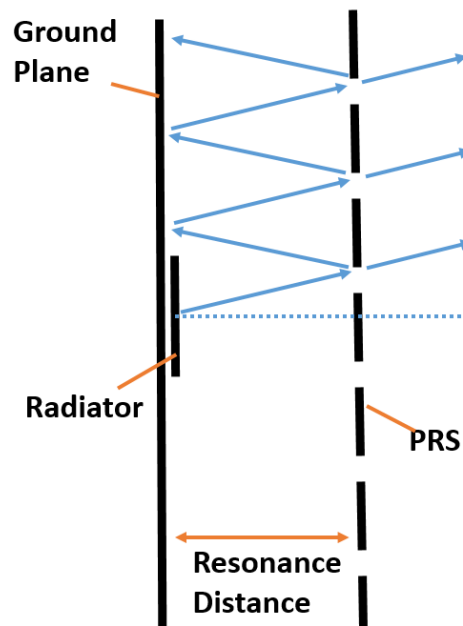


Figure 1.4: Schematic of an FPC based antenna using PRS layer.

be formed by using periodic arrays of dipoles or patches [23], [24], [26], also known as Frequency Selective Surfaces (FSS). Besides creating a resonant cavity, the PRS also collimates the waves coming from the fed antenna and hence increases the broadside gain of the antenna [27].

In FPC based antennas consisting of PRS layer, waves emerging from the driven antenna undergo multiple reflections between PRS and ground layer and travel long paths, as illustrated in Fig. 1.4. The path length, the total reflection from the ground plane and the phase of the reflection coefficient of the PRS layer introduce a phase shift. The resonance distance between the ground plane and PRS layer is such that the total phase shift provided by the ground plane, PRS layer and travelled path is an integral multiple of 2π . Hence, the resonance distance is a function of the wavelength and the reflection coefficient of PRS layer. The magnitude of the reflection coefficient of the PRS layer determines the maximum gain. The gain of the antenna consisting of the PRS layer increases and the bandwidth decreases with the increase in the magnitude of the reflection coefficient of the PRS layer. In order to increase both the gain and bandwidth, the reflection coefficient of the PRS layer must have a linearly increasing (with frequency)

phase and a constant magnitude, it results in the maximum gain within a certain frequency range.

In this thesis, the PRS layer consisting of a superstrate and an array of parasitic patches has been utilized. In FPC based antennas, the periodic parasitic layer is designed in a way to provide high impedance electromagnetic surface (HIEM) to suppress surface waves [28]. Although it is a leaky-wave antenna, it is also a printed ESPAR antenna. If the parasitic elements are connected with each other through tunable impedance circuits, electronic reconfigurability in terms of radiation pattern, frequency or polarization can be achieved. Moreover, antenna gain can be enhanced by tuning the parasitic impedances (loads) due to the suppression of surface waves. By reconfiguring the parasitic layer with tunable impedance circuits, different surface impedances exist on different parts of the parasitic layer and hence beamforming can be implemented [28]. A high-gain antenna with a reconfigurable operating frequency has been designed using a PRS layer in [29]. FPC based antennas are analyzed by determining the reflection coefficient of a PRS layer and fulfilling the resonance condition. However, a reconfigurable PRS antenna can be analyzed and designed from the ESPAR antenna perspective. The antenna based on a PRS layer has strong mutual coupling and contains multiple reflections between driven and parasitics elements. The radiation pattern can be reconfigured by varying the mutual coupling through tunable impedances. In this thesis, ESPAR antenna approach has been used to design FPC based antenna arrays.

1.2 Applications of Beam-Shaping Antenna Arrays

1.2.1 Beam-Shaping Parasitic Antenna Arrays for a Cellular Communication System

In mobile communication systems a coverage area is divided into a number of cells, each cell is served by a Base Station (BS). A number of BSs is grouped together to form a cluster, all the neighbouring cells in a cluster use different frequency bands to mitigate the interferences. However, these frequencies are reused in other clusters. The antennas that are used at the BS typically radiate in a sector of 60° , 90° or 120° to increase the



Figure 1.5: Configuration of sector antennas for cellular communication [2].

1850 – 1990 MHz: $+45^\circ$ – -45° Polarization

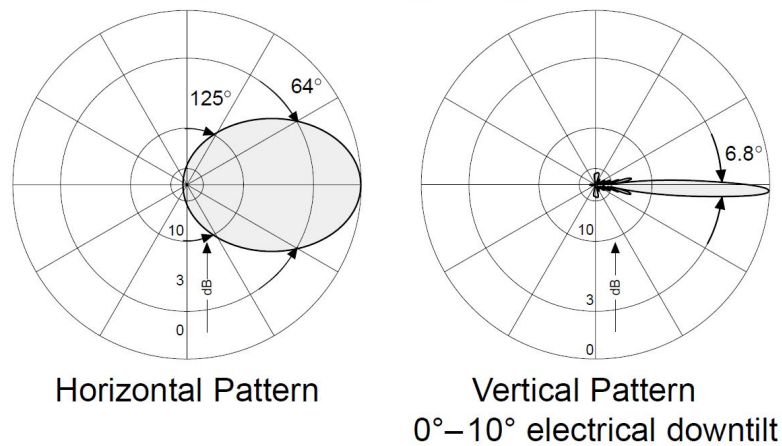


Figure 1.6: Radiation pattern of Kathrein antenna [3].

capacity. Moreover, to reduce the co-channel interference these directional sector antennas are placed at the edge of the cells. A typical configuration of a sector antenna is shown in Fig. 1.5.

The radiation pattern of a BS antenna [3], typically used for cellular communication is shown in Fig. 1.6. It is usually placed on a rooftop or a tower and tilted 10° downwards electrically or mechanically to provide coverage in a sector. This downward tilt allows to provide coverage on the ground and reduce the interference to the co-channel cells, which use the same frequency bands belonging to a neighbouring cluster. It is evident that

such BS antenna generally overexposes an area in the line of sight of the main beam and underexposes the rest of the area. Therefore, in order to achieve the required throughput in badly covered areas, a higher transmitted power is needed at the base station, it may lead to harmful RF exposure in certain areas. The use of micro cells network (with smaller antennas) can solve this problem but that raises important economical challenges. Another way to attain those different goals is to adapt the radiation pattern of existing base station antennas according to the needed power distribution versus position on the ground and it is the crux of this work.

If phased arrays are designed to implement beam-shaping for BS, they will require the use monolithic microwave integrated circuits (MMIC) which are provided by companies such as Analog Devices, Anokiwave, Qorvo, etc. and have multiple channels for transmit (Tx) and receive (Rx) operation; they provide gain and phase adjustment to each antenna to carry out beam-shaping. For instance, phased array MMIC ADAR1000 [30] from Analog Devices provides 4 Tx/Rx channels. However, the big drawback is that such transceiver MMICs are too expensive to be used in commercial civilian applications. On the other hand, if parasitic antenna arrays are utilized for beam-shaping application, they will require inexpensive varactor diodes or PIN diodes to carry out beam-shaping. Consequently, parasitic antenna arrays are employed in this thesis to adapt the radiation pattern of base station antennas. In the designed parasitic antenna array, the BS antenna [3] is used as a driven antenna and parasitic elements (dipoles) with impedances (capacitors or inductors) are placed in front of it to adapt its radiation pattern. The use of commercially available base station antenna eliminates the need to redesign the driven antenna of the parasitic antenna array, which is economical a posteriori adaptation.

In [31], only the beam width of the base station antenna is reconfigured by tuning varactor diodes attached to the parasitic elements. Antennas using frequency selective surface (FSS) with reconfigurable patterns have also been proposed [32], [33], in which PIN diodes (ON or OFF) are used for the reconfigurability of a beam. Reconfigurable transmitarrays have also been designed for beamforming applications [34]. The designs available in the literature can only scan the beam. However, we would like to design the

parasitic antenna array with a beam-shaping capability to improve coverage in a given area. In this thesis for the first time, to the author's best knowledge the parasitic antenna array has been designed and implemented for base stations (4G or 5G) to carry out beam-shaping. A tunable impedance circuit has been designed with the varactor diode MAVR-011020-1411 [4] and inductor to provide both capacitive and inductive impedances. The use of such tunable impedance circuit provides more degrees of freedom than the PIN diode and it allows us to shape the antenna radiation pattern. Moreover, a small prototype of an ESPAR antenna has been designed for a base station and beam-shaping is carried out electronically by tuning the impedances. In comparison to different mm-wave phased arrays presented in [6], a comparable performance can be achieved by the parasitic antenna array in terms of beam scanning range. However, the designed parasitic antenna array has drawbacks of having a narrow bandwidth and lower gain than the phased arrays. A lower gain is obvious due to the use of only few driven antenna elements in a parasitic antenna array. The narrow bandwidth is due to the change in the impedance of the parasitic loads with frequency, which varies the mutual coupling, and it leads to an unstable radiation pattern in a wide frequency band.

1.2.2 Beamforming Antenna Array for the Automotive Radar

This subsection is confidential due to a non-disclosure agreement with an industrial partner.

1.3 Objectives and Novelities of the Thesis

The main objective of the thesis is to design beam-shaping parasitic antenna arrays for cellular communication systems and beam scanning antennas for automotive radar applications. The parasitic antenna array has been designed for the base station of a cellular communication system to improve the radio coverage in a given area. Varactor diodes have been employed to electronically reconfigure the ESPAR antenna radiation pattern. Similarly, another ESPAR antenna based on an FPC with a reconfigurable PRS layer has been proposed for a radar application. Antenna arrays are utilized in

the automotive radar to implement digital beamforming. Hence, the antenna arrays have been designed for automotive radar in the 24 GHz and 76 GHz bands.

The novelties of the work that are detailed in this thesis are listed below:

- A computationally efficient spectral optimization method has been proposed to optimize the loads of the ESPAR antenna to implement beamforming and beam-shaping. It has been partly published in [19]. An attempt has been made to analytically determine the optimum loads in an ESPAR antenna.
- A parasitic antenna array has been designed for the base station of a mobile communication system to improve the coverage in a given area according to the needed power distribution versus position on the ground. This work has been published in [35].
- In order to adapt the radiation pattern electronically, an ESPAR antenna has been designed for a mobile communication by using varactor diodes. For that purpose, a tunable impedance circuit has been designed as well. This work has been published also in [35].
- A printed ESPAR antenna with parasitic patches on a superstrate is proposed for radar application. It can steer the beam from -9° to $+9^\circ$ around broadside of the array while maintaining a high gain. Varactor diodes can be biased by the current crossing all the connected parasitic elements. This work has been published in [36].
- Confidential
- Confidential

1.4 Design Tools

In the framework of this thesis, various tools have been employed for different purposes. The Method of Moments (MoM) has been exploited for the analysis and design of parasitic antenna arrays. For that purpose an in-house MoM code developed in C++ and MATLAB [37] has been utilized.

The MoM code helps us to optimize the parasitic loads in an efficient way by using open-circuit to embedded approach and proposed optimization methods. It helps to compute all the open-circuit patterns at once by utilizing the full-MoM impedance matrix. The commercial EM software, CST [38] has been utilized to validate the design of parasitic antenna array for a base station because the designed parasitic antenna array is a 3D antenna. In CST both frequency domain and time domain solvers have been employed for simulation. The Time Domain (TD) solver or the transient solver of the CST is based on the Finite Integration Technique (FIT) [38]. For the design of printed ESPAR antenna, the MoM code for layered-medium, developed in the lab has been used. The validation is carried out using the IE3D [39] software because the IE3D also uses the MoM for layered medium. In order to design antenna arrays for the automotive radar, the CST software is used because we did not need to optimize any parasitic loads. Moreover, for the circuit simulations and PCB design, the Advanced Design System (ADS) [40] software has been utilized.

1.5 Outline of the Thesis

The thesis is divided into multiple sections considering the antennas designed for different applications.

Chapter 1 sheds light on the objectives and motivation behind the thesis. It details the literature review of the work which is carried out in the framework of this thesis.

Chapter 2 presents the advantages of the Electromagnetic (EM) model and the proposed optimization method, utilized to design the parasitic antenna array. Furthermore, an analytical approach to design a parasitic antenna array has been explored as well.

Chapter 3 discusses in detail the methodology employed for the analysis and design of the parasitic antenna array for a cellular communication system. Moreover, it explains the designed prototype. The comparison between simulation and experimental results of designed prototypes is also shown here.

Chapter 4 explores Electronically Steerable Parasitic Array Radiators

(ESPAR) with the purpose of carrying out electronic beam-shaping. It presents two ESPAR antenna designs, one for Base Station (BS) application and the other one for radar. It also depicts the non-intrusive biasing of varactor diodes in printed ESPAR antenna.

Chapter 5 is related to the analysis and design procedure of antenna arrays employed in automotive radar. However, this chapter is confidential due to a non-disclosure agreement with an industrial partner.

Chapter 6 concludes the thesis and presents a perspective about future work regarding the design of parasitic antenna arrays for base station application and antenna arrays for automotive radar applications.

Appendix A details the Green's function in a layered medium, utilized in the method-of-moments (MoM) code. The MoM code has been used for the simulation of printed ESPAR antenna for a radar application in Chapter 4.

Appendix B describes the working principle and formulations which have been utilized to design antennas in Chapter 5. However, this chapter is confidential due to a non-disclosure agreement with an industrial partner.

CHAPTER 2

Electromagnetic Model and Computation of Parasitic Loads in a Parasitic Antenna Array

The radiation characteristics of a parasitic antenna array can be modified by varying the loads attached to the parasitic elements. In this thesis, the open-circuit pattern to embedded pattern approach is employed to compute the radiation pattern when dynamic loads are attached to the parasitic radiators. It provides results exactly (within machine precision) matching those of full-wave simulations without any approximation and it is computationally highly efficient in the optimization of loads.

An attempt has been made to determine the loads of a parasitic antenna array analytically. Besides, a spectral optimization technique is proposed to optimize the loads in order to obtain the desired radiation patterns. It has been observed that the spectral optimization performs better than the classical genetic algorithm in terms of the quality of solution and computation time, which makes the parasitic antenna array suitable for real-time applications. A comparison has been made between the spectral optimization technique and the genetic algorithm to emphasize the performance of

the proposed algorithm.

Section 2.1 provides an introduction regarding the EM modelling of loaded parasitic antenna arrays. Section 2.2 details the EM model that has been employed for the design and analysis of parasitic antenna arrays or ESPAR antennas in this thesis. Section 2.3 delineates the advantages offered by the proposed EM model. Section 2.4 explains the analytical method which has been developed to determine the loads in a parasitic antenna array. Section 2.5 details the proposed spectral optimization technique for determining the loads in a parasitic antenna array.

2.1 Introduction

The hardware required to develop parasitic antenna arrays is not very expensive but it costs computationally to determine the values of loads [18], since a proper modelling of the effects of mutual coupling is required. The approach used in this thesis consists of using a model for parasitic antenna arrays that does not entail any underlying approximation, such that it can be applied to any parasitic antenna array while preserving ultra-fast evaluation for efficient optimization. The open-circuit to embedded pattern model [7], [18] has been used to express the radiation pattern of the ESPAR antenna in terms of the loads attached to the parasitic elements. The relation between the radiation pattern and parasitic loads is non-linear, which makes it difficult to analytically determine the set of loads that produces the desired radiation pattern [8], [18]. An analytical method has been developed for the single-mode antennas in [13], it only controls the main beam direction and does not help in beam-shaping, SLL suppression and beam width control. In this thesis, an attempt has been made to determine analytically the loads of a parasitic antenna array, instead of using an optimization algorithm. It has been shown that it becomes difficult to analytically determine the realistic load values to form a desired radiation pattern.

In the literature, different deterministic [8], stochastic [41], [16], [10] and meta-heuristic [18] algorithms can be used to find the optimized set of loads. The deterministic algorithms converge faster but they are more likely to converge to a local minimum. Heuristic algorithms, such as the genetic

algorithm [42] can evade local minima but their computational complexity increases very rapidly with the increase of the number of parameters unknowns. The combination of deterministic and heuristic algorithms has been used in this context as well [18]. For parasitic antenna arrays, the strength of an optimization algorithm dictates the number of parasitic elements that can be realistically considered and in turn the beamforming and beam-shaping capabilities [18]. Therefore, there is a need for an optimization algorithm designed specifically for the radiation pattern manipulation of a parasitic antenna array. The optimization technique developed by me in [19], [35] uses the spatial harmonic decomposition of loads and it provides the optimum solution in a very short time. Here, this approach is generalized to form an efficient and robust method called the spectral optimization. This approach decomposes the loads into a number of discrete functions that span the whole array; the corresponding multiplying coefficients are optimized. It is combined with Nelder-Mead simplex method [37] to optimize two coefficients at a time at most, which in turn optimize the parasitic loads to form a desired radiation pattern. The proposed spectral method is investigated in detail and a performance comparison is made with the classical genetic algorithm [42], [5].

2.2 Open-Circuit To Embedded Pattern Approach

If the method of moments (MoM) is used for the full-wave simulation, for each set of parasitic loads the exact currents on all the antennas need to be computed to calculate the radiation pattern of the parasitic antenna array. This approach is time consuming, since the MoM involves the computation of the inverse (or LU decomposition) of the impedance matrix, which can be very large. The optimization of parasitic loads becomes very tedious because, for different combination of loads, the system of equations needs to be solved again. Therefore, in order to immensely speed up the computation without any approximation, a computationally efficient Electromagnetic (EM) model has been exploited. The open-circuit pattern of an antenna in an array does not depend on the loads while the embedded element pattern does. The embedded patterns correspond to patterns

obtained with the elements of interest fed with a unit-voltage Thevenin source, while the other elements are passively terminated. The open-circuit patterns suppose a unit-current source at the element of interest, while all other elements are open-circuited. So, the open-circuit patterns of all antennas (active or parasitic) are computed once and for all. The embedded element pattern of all the antennas are related to the open-circuit patterns through following equation [7], [43], [14]:

$$\mathbf{f}^e = (\mathbf{Z}^a + \mathbf{Z}^L)^{-1} \mathbf{f}^{O.C.} \quad (2.1)$$

Here \mathbf{f}^e are the embedded patterns, $\mathbf{f}^{O.C.}$ are the open-circuit patterns, \mathbf{Z}^L is the diagonal matrix containing the load impedances attached to the active and parasitic antennas, \mathbf{Z}^a is the N-port impedance matrix containing mutual coupling information. In \mathbf{f}^e and $\mathbf{f}^{O.C.}$ matrices each row corresponds to a given antenna and each column corresponds to a given direction. One should underscore that \mathbf{Z}^a does not contain all the mutual coupling information, the missing information being provided by the open-circuit patterns. Equation (2.1) is used for computation of embedded patterns for all the antennas. The load values for the driven antennas are usually fixed (50 Ω matched to the RF source), while the loads attached to the parasitic elements can be varied. By varying the entries of the \mathbf{Z}^L matrix the embedded element patterns can be adapted [18]. The total radiation pattern of the array is obtained as the superposition of the embedded patterns of the driven elements only. Hence, beamforming and beam-shaping can be implemented by just varying the loads attached to the parasitic elements. The matrix $(\mathbf{Z}^a + \mathbf{Z}^L)$ has dimensions equal to the number of loads, so its inverse can be computed much faster than that of the MoM impedance matrix. Since the open-circuit patterns and N-port impedance matrix are computed only once, the computation of embedded patterns for different sets of loads \mathbf{Z}^L is extremely quick and simple. Besides, all the open-circuit patterns can be computed at once with the MoM impedance matrix. A method-of-moments (MoM) code developed in-house is used for the simulation of the parasitic antenna array.

2.3 Simulations

Simulations have been carried out, considering a bow-tie log antenna operating at 1800 MHz (with 10:1 bandwidth) as an active element, while 30 parasitic dipoles (3 rows and 10 columns) are placed in front of it and a back reflector is used as shown in Fig. 2.1. The parasitic dipoles of length $3\lambda/4$ with diameter of 0.06λ and 0.24λ spacing among them, are placed at a λ distance from the bow-tie log antenna. Each dipole has a load attached to its terminals. A comparison between open-circuit to embedded

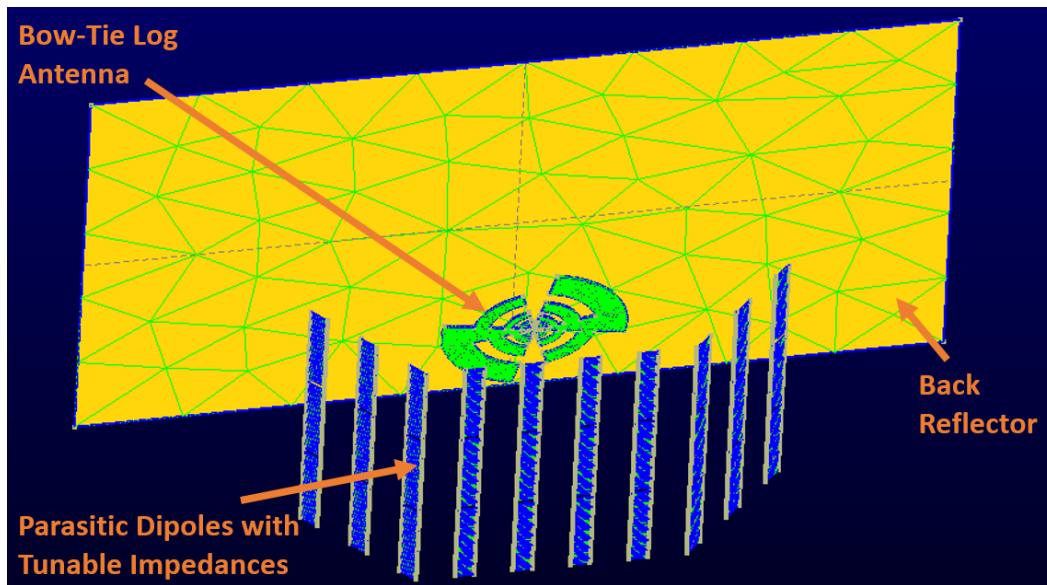


Figure 2.1: Parasitic antenna array using bow-tie antenna.

pattern approach and single-mode approximation is made, the best available single-mode approximation is used for parasitic dipoles by using macro-basis functions (MBF) [44] with only one MBF per parasitic element. The comparisons for the cases of open-circuited parasitics and short-circuited parasitics are shown in Fig. 2.2 and Fig. 2.3, respectively (no optimization is carried out at this point). The difference between the results obtained with those two approaches is larger for the case of open-circuited parasitics than for the case of short-circuited parasitics. This depicts the shortcomings of the single-mode approximation.

A comparison between computation time is made for the full-wave sim-

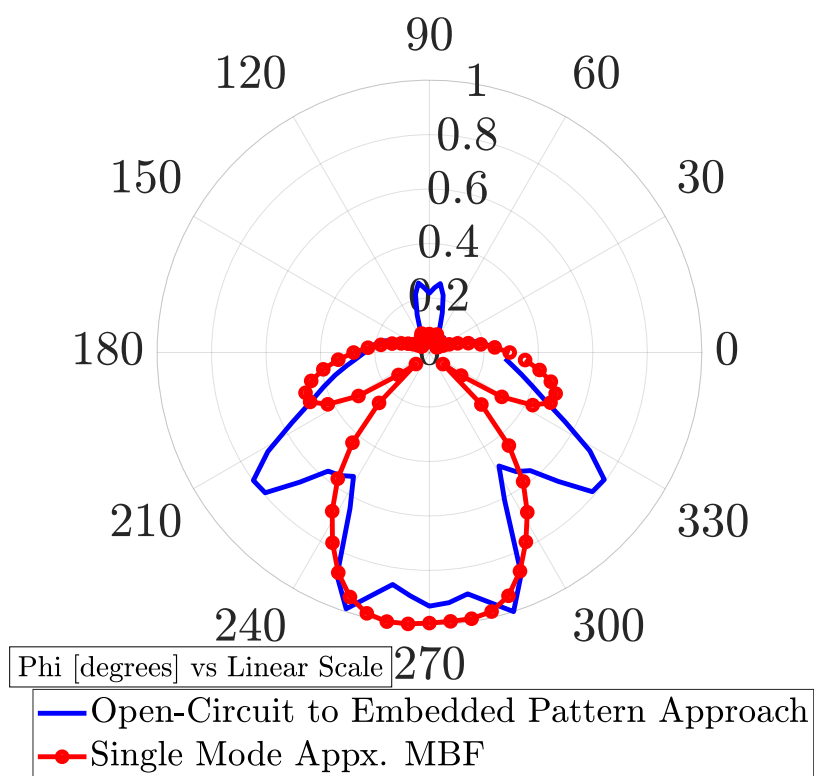


Figure 2.2: E-field radiation pattern of parasitic antenna array with open-circuited parasitics at 1800 MHz.

ulation and the open-circuit to embedded pattern approach to show its computational advantage during load optimization, keeping in mind that, down to machine precision, both approaches provide the same result. The simulations are executed on an i7 PC with 3.40 GHz processor, 16 GB RAM and 64-bit operating system.

Table 2.1: Computation Time Comparison.

Full-wave simulation computation time	Open-circuit pattern computation time (sec)	Embedded pattern from open-circuit pattern, computation time
30 mins and 4 secs	30 mins and 58 secs	4.8 msecs

It can be seen from Table 2.1 that the open-circuit pattern computation

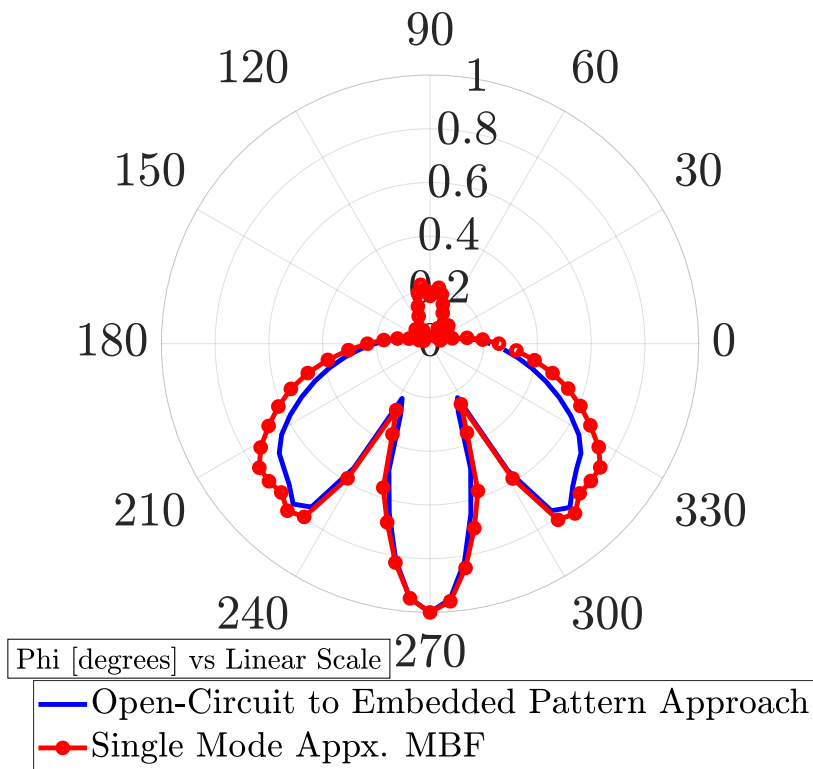


Figure 2.3: E-field radiation pattern of parasitic array with short-circuited parasitics at 1800 MHz.

time is similar to that of the full-wave simulations (order of half an hour) but the embedded pattern computation time is in the order of milliseconds. With the full-wave simulation, the computation of the cost function would take the same time for each set of loads. For instance, if 1000 combinations of loads are tried to reach the optimum set of loads, with the full-wave simulation the total computation time would be 501 hrs, 6 mins and 40 secs. While with the open-circuit to embedded pattern approach it would take 31 mins and 3 secs. The gain in computation time can be seen easily (here about 1000 times faster). This computation gain depends on the ratio of total number of basis functions (MoM) to the number of loads, and the number of iterations tried before the problem converges. For this array, the total number of basis functions involved in the MoM code are 8744.

2.4 Analytical Solution

Different optimization algorithms are utilized in order to determine the optimum set of loads of a parasitic antenna array to form a desired radiation pattern. This load optimization a computationally expensive method due to its iterative nature. Therefore, an effort has been made to develop an analytical method to determine the optimum set of loads of a parasitic antenna array.

Consider a parasitic antenna array, consists of a total N antennas with a single driven (active) antenna element and N-1 parasitic radiators. The EM model expressed in (3.9) can be rewritten only for the embedded pattern of a driven element as:

$$f^e = e_n^T (\mathbf{Z}^a + \mathbf{Z}^L)^{-1} \mathbf{f}^{O.C.} \quad (2.2)$$

Here, f^e is a vector containing only the embedded pattern the driven antenna and e_n is a Nx1 column vector with all entries zeros except a unit entry corresponding to the driven element port. We would like to form the objective radiation pattern (f^o) with the parasitic antenna array. The f^o pattern is known and (2.2) can be written as:

$$f^o = e_n^T (\mathbf{Z}^a + \mathbf{Z}^L)^{-1} \mathbf{f}^{O.C.} \quad (2.3)$$

Taking the transpose on both sides leads to

$$f^{o,T} = \mathbf{f}^{O.C.,T} (\mathbf{Z}^a + \mathbf{Z}^L)^{-1} e_n \quad (2.4)$$

It resembles with the linear system of equations of the form

$$b = \mathbf{A} w \quad (2.5)$$

with

$$b = f^{o,T} \quad (2.6)$$

$$\mathbf{A} = \mathbf{f}^{O.C.,T} \quad (2.7)$$

$$w = (\mathbf{Z}^a + \mathbf{Z}^L)^{-1} e_n \quad (2.8)$$

where b and \mathbf{A} are known and w needs to be determined. It can be seen that b is the objective radiation pattern, \mathbf{A} consists of all the open-circuit patterns and w consists of the N-port impedance and load matrix. The least-square solution to this linear system can be written as:

$$w = (\mathbf{A}^H \mathbf{A})^{-1} \mathbf{A}^H b \quad (2.9)$$

Once w is computed, based on (2.8) \mathbf{Z}^L can be obtained using

$$\mathbf{Z}^L w = e_n - \mathbf{Z}^a w \quad (2.10)$$

Through this methodology, parasitic loads of a parasitic antenna array

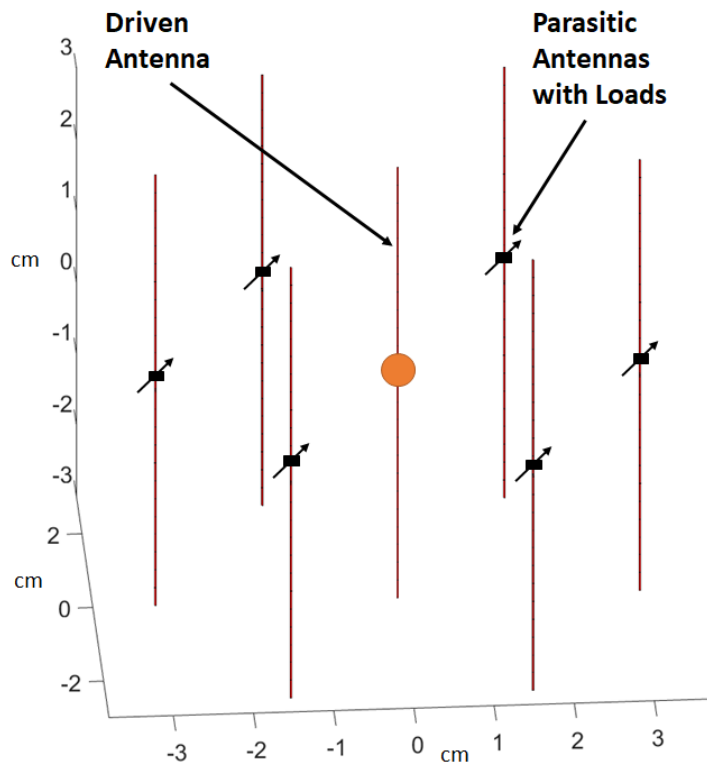


Figure 2.4: Circular array of seven dipoles.

can be computed analytically. For illustration, a circular array of 7 half-

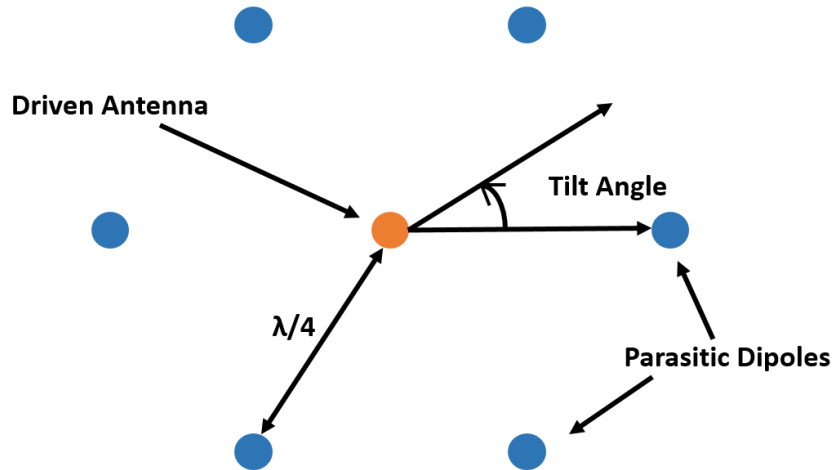


Figure 2.5: Circular array of seven dipoles (Top view).

wavelength dipole antennas is considered, it is operating at 2.5 GHz in the ISM band. The driven dipole antenna is surrounded by 6 parasitic dipole radiators with the loads attached to their terminals as shown in Fig. 2.4. The radius of the circular array is $\lambda/4$.

Table 2.2: Complex loads computed for different radiation patterns, using the analytical method.

	Case I (0° tilt)	Case II (15° tilt)	Case III (30° tilt)	Case IV (45° tilt)
Z_1	77-170i	-6-105i	-20-97i	36-133i
Z_2	-73-114i	1+0i	-21-5i	17+6i
Z_3	0-25i	-54+6i	-17+5i	-112+45i
Z_4	-77-51i	81-6i	-642-152i	-9-4i
Z_5	181-28i	-9-43i	9-77i	-100+7i
Z_6	-75-51i	29-31i	14-76i	76+140i
Z_7	4-23i	-81+30i	-175-1047i	-60-15i

The analytically determined complex loads to form different objective radiation patterns are given in Table 2.2 and the obtained radiation patterns are shown in Fig. 2.6. The objective radiation patterns are scanned at 0°, 15°, 30° and 45°. The tilt angle of the scanned beam is defined in the azimuth plane, as shown in Fig. 2.5. Due to the symmetry of the circular

Table 2.3: Reactive loads computed for different radiation patterns, using the analytical method.

	Case I (0° tilt)	Case II (15° tilt)	Case III (30° tilt)	Case IV (45° tilt)
Z_1	-249i	-95i	-60i	-181i
Z_2	378i	0i	-325i	13i
Z_3	-25i	-65i	282i	-270i
Z_4	-87i	+45i	-862i	-3i
Z_5	-264i	+6i	-82i	-136i
Z_6	-92i	-25i	-86i	158i
Z_7	-19i	-19i	-2236i	-428i

array, the radiation patterns can be scanned in other sectors by shifting the arrangement of the set of loads.

This method poses two problems. One is that the solution may contain parasitic loads with real parts, which can be negative as well. The negative real part of parasitic loads means the presence of generators at the ports of parasitic radiators, which is of course not acceptable in a parasitic antenna array. The second problem is that the solution may contain the impedance of a driven port other than 50Ω that could disturb the matching of the antenna. We tried to impose the condition on parasitic loads \mathbf{Z}^L to be with zero real parts and then determine the reactive loads to form the objective radiation pattern. After computing w from (2.9), the condition on loads to be only reactive is imposed as:

$$P = e_n - \mathbf{Z}^a w \quad (2.11)$$

$$x^L = \Im(Z^L) \quad (2.12)$$

$$\Re(P) = P_r = -x^L w^{im} \quad (2.13)$$

$$\Im(P) = P_i = x^L w^r \quad (2.14)$$

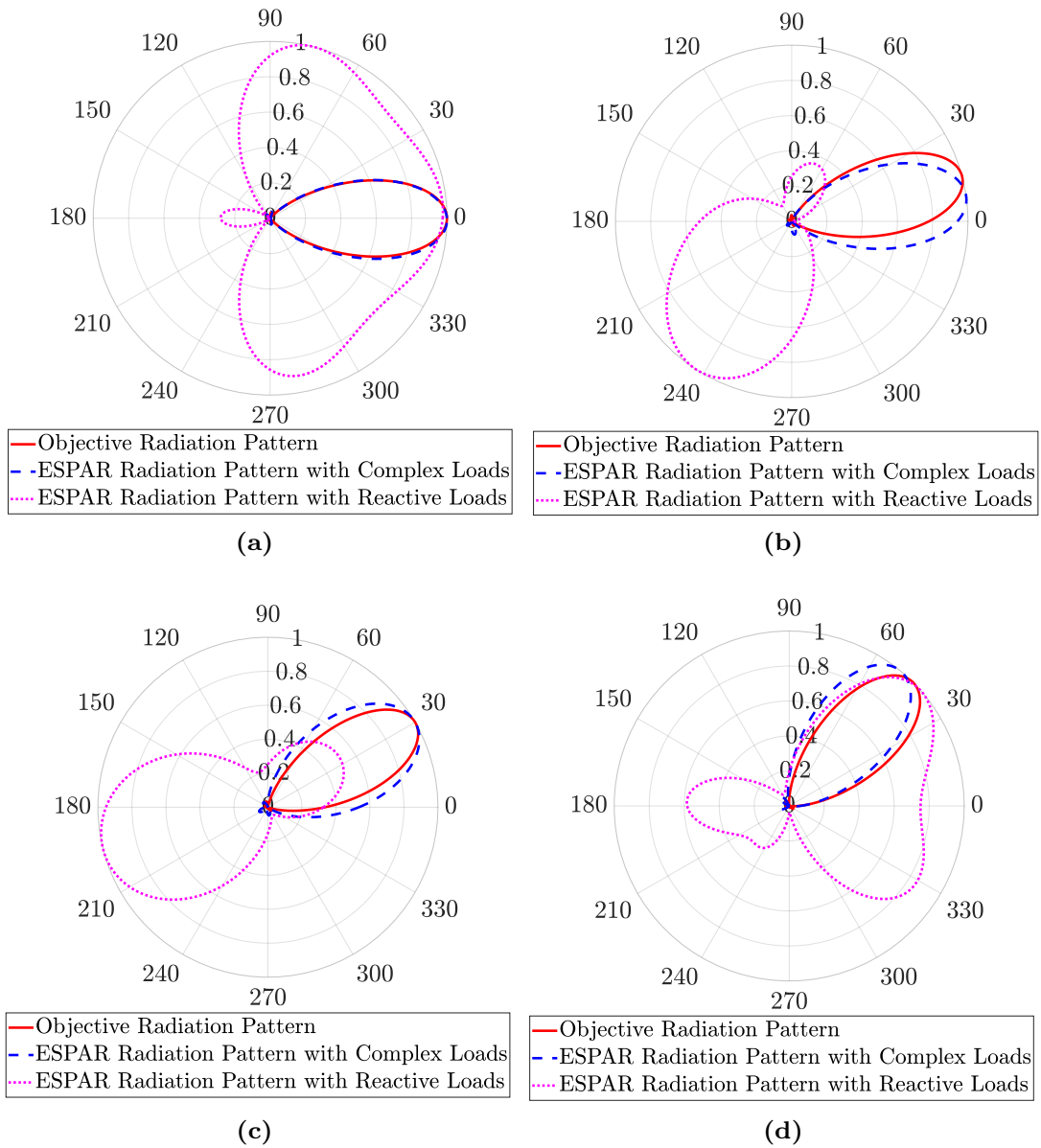


Figure 2.6: Comparison of different objective power patterns and the obtained power patterns from the ESPAR with complex and reactive loads, using analytical method, Frequency=1800 MHz, Phi [degrees] vs Linear Scale, (a) case I (0° tilt) (b) case II (15° tilt) (c) case III (30° tilt) (d) case IV (45° tilt).

which can be re-written as:

$$G_r = -P_r ./ w^{im} = x^L \quad (2.15)$$

$$G_i = P_i ./ w^r = x^L \quad (2.16)$$

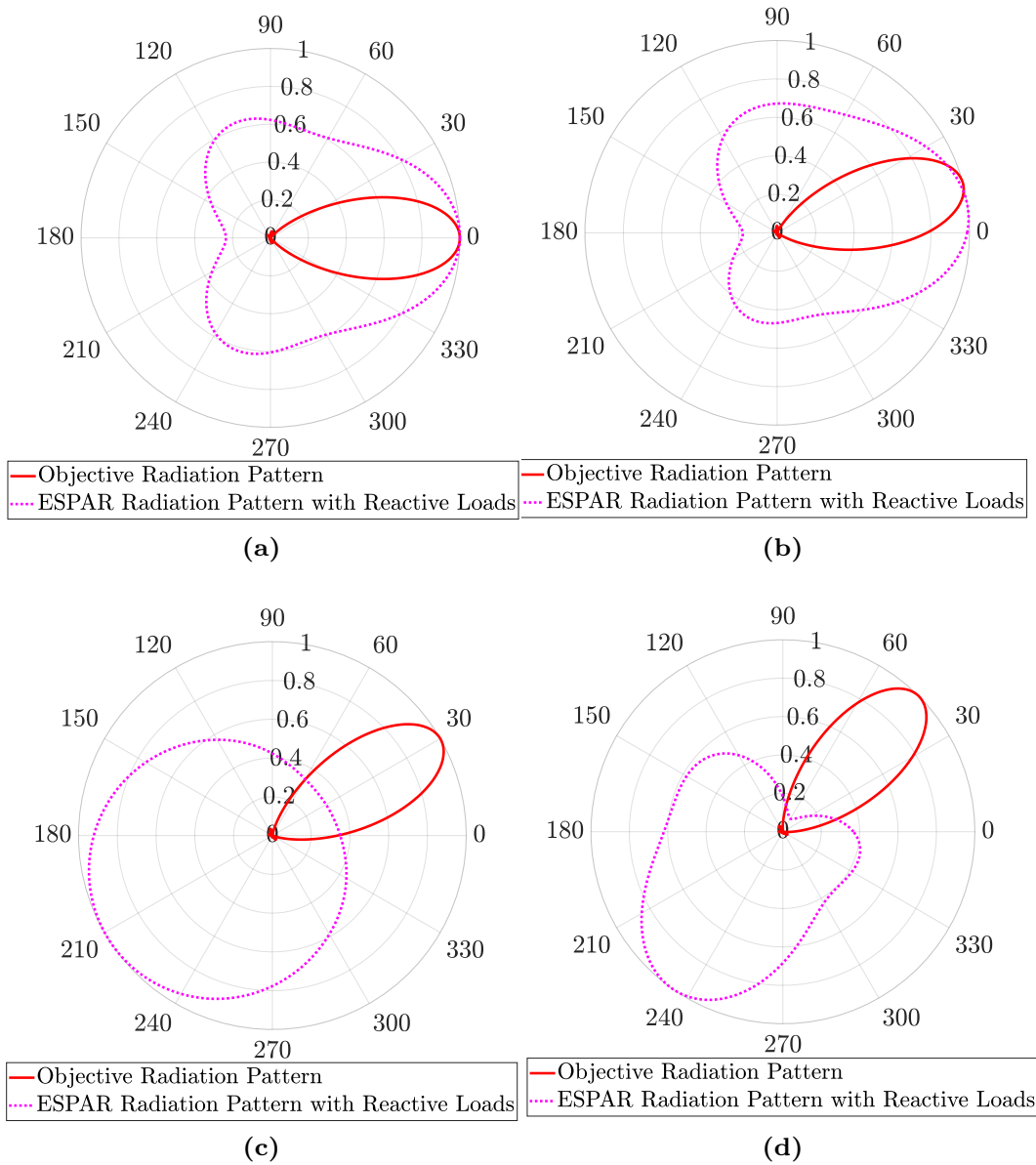


Figure 2.7: Comparison of different objective power patterns (different phase) and the obtained power patterns from the ESPAR with reactive loads, using analytical method, Frequency=1800 MHz, Phi [degrees] vs Linear Scale, (a) case I (0° tilt) (b) case II (15° tilt) (c) case III (30° tilt) (d) case IV (45° tilt).

Here ./ is the element by element division operator. The least-square solu-

tion to this linear system can be written as:

$$x^L = (\mathbf{R}^H \mathbf{R})^{-1} \mathbf{R}^H G \quad (2.17)$$

where

$$G = \begin{bmatrix} G_r \\ G_i \end{bmatrix} \quad (2.18)$$

$$\mathbf{R} = \begin{bmatrix} \mathbf{U} \\ \mathbf{U} \end{bmatrix} \quad (2.19)$$

$$\mathbf{U} = I_N \quad (2.20)$$

Here I_N is an identity matrix of size N . The reactive loads are computed for the circular array consisting of 7 half-wavelength dipoles and are given in Table 2.3. By using the explained analytical approach with the condition of loads being reactive only, we fail to yield the objective radiation patterns from the parasitic antenna array, as shown in Fig. 2.6. Actually, by using this approach, first we obtain the solution with complex loads and then we remove the real part of the complex loads in a least square manner to obtain only reactive loads. However, the removed (real) part of the complex loads contribute significantly to form the desired radiation pattern. That is the reason this approach of computing only reactive loads does not work.

When we put a complex objective radiation pattern in (2.3), we try to obtain the objective radiation pattern with a certain magnitude and phase pattern as well. In most applications the phase of the antenna radiation pattern is irrelevant. However, using this methodology by changing the phase of an objective radiation pattern, different results can be obtained, as shown in Fig. 2.7. By using different phase variation for the same objective patterns which are shown in Fig. 2.6, different radiation patterns are formed. So, the question is what should be the phase of the objective radiation pattern in (2.3) that would lead to the value of loads to form the radiation pattern closest to the objective radiation pattern in terms of magnitude. This problem has not been tackled in this thesis. The effort to develop an analytical method to compute the reactive loads to form the objective

radiation patterns from a parasitic antenna array has not been successful. Therefore, we have used the optimization techniques to design the parasitic antenna arrays.

2.5 Spectral Optimization

A spectral optimization is proposed, parasitic load values are decomposed into a given basis versus positions of parasitic elements, supposing they are distributed along a line or a circle. Then the coefficients in that basis are determined such that the obtained linear combination minimizes the cost function. Here, we have considered harmonic and Gaussian bases to optimize the parasitic loads of a parasitic antenna array.

2.5.1 Harmonic Basis

The harmonic basis is used to represent the parasitic load values of a parasitic antenna array. The optimum load configuration can be expressed as the summation of sines and cosines of different harmonics, as given in (2.21). The unknowns are the amplitudes a_p and b_p of the cosines and sines of each harmonic, which determine the optimum, purely reactive, load configuration for a desired radiation pattern. The graphical representation of the harmonic basis is shown in Fig. 2.8, only two harmonic bases are illustrated.

$$Z_{Lmin}^n = j \sum_{p=1}^N \left(a_p \cos \frac{2\pi np}{N} + b_p \sin \frac{2\pi np}{N} \right). \quad (2.21)$$

Here N is the total number of parasitic loads, p is the harmonic being optimized, n is the element index, a_p and b_p are the purely real amplitudes of cosines and sines, respectively. By construction, the harmonics considered form an orthogonal basis with respect to a dot product. The amplitudes of cosines and sines of each harmonic are optimized, such that the radiation pattern obtained with sum of harmonics minimizes the cost function. The harmonics are optimized one-by-one, starting with the lowest-order, since lower-order harmonics dictate the main lobe and the overall shape of the radiation pattern, while higher harmonics contribute to the finer details of the radiation pattern. In this way, joint optimization of all a_p and b_p

coefficients is circumvented. At each step only two coefficients of a single harmonic are optimized while coefficients of other harmonics are being frozen. Once amplitudes of cosines and sines have been optimized for each harmonic, subsequent optimization rounds may be run, starting again from lowest harmonics. (It has been noticed that running a few other rounds helps to further refine the optimum solution).

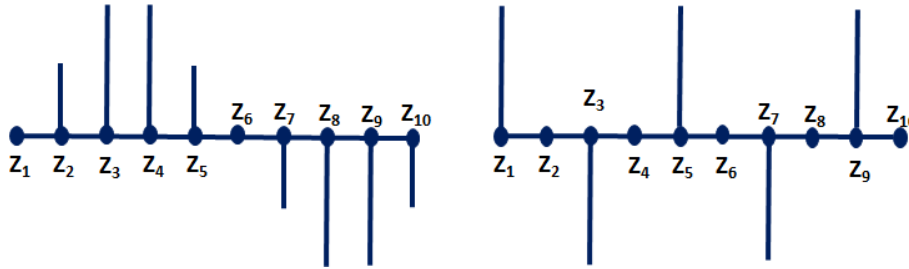


Figure 2.8: Graphical representation of harmonic basis.

By representing the optimum load in terms of summation of sines and cosines, the number of variables to be jointly determined has been reduced to only two, a_p and b_p . These two variables a_p and b_p can be optimized for each harmonic using any heuristic algorithm. For that purpose the Nelder-Mead simplex method [37] has been used here. Therefore, there will always be only two variables that need to be optimized for each harmonic, irrespective of the number of loads. This makes the optimization complexity less dependent on the number of loads which need to be optimized. However, it will still depend on the number of loads because the number of harmonics is equal to the number of loads.

2.5.2 Gaussian Basis

The parasitic loads can also be optimized by decomposing them into a Gaussian basis, as given in (2.22). Only two Gaussian bases are illustrated in Fig. 2.9. The Gaussian basis is defined such that the peak of each Gaussian function is shifted at the position of a given parasitic element. So, the size of the Gaussian basis is equal to the number of parasitic loads. For each basis, the variance of the Gaussian function is kept fixed. The variance is chosen according to the spacing between the parasitic loads. In this thesis,

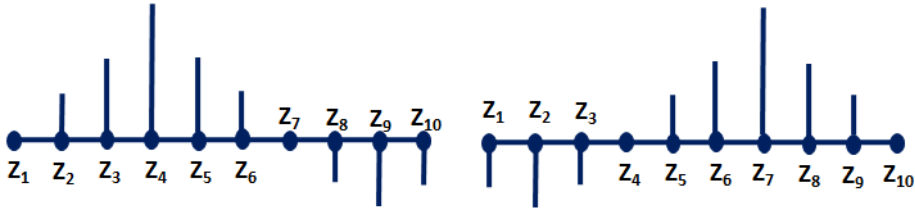


Figure 2.9: Graphical representation of Gaussian basis.

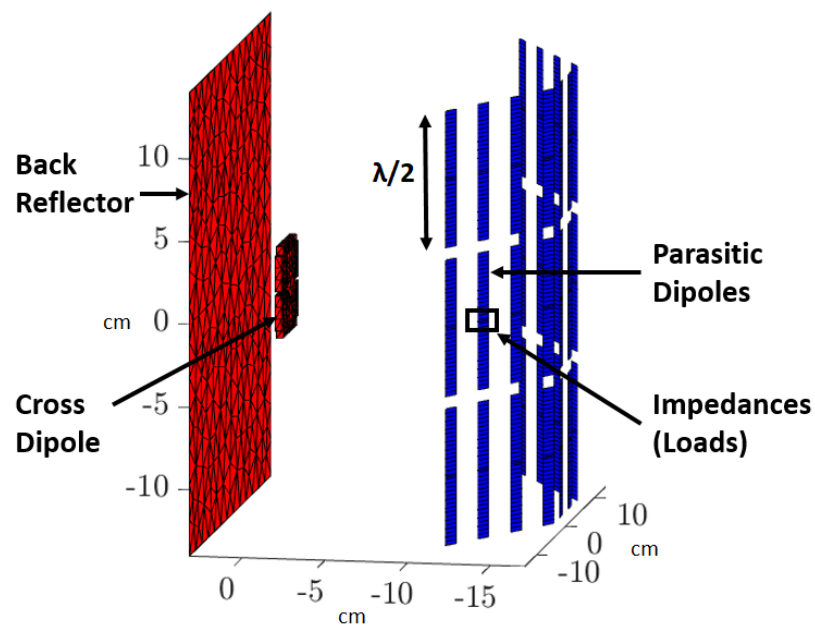
the variance is considered as (the fraction of wavelength) spacing between parasitic radiators. The weights w_p are optimized for each basis such that the sum of basis minimizes the cost function. Such a basis is not orthogonal, the Nelder-Mead simplex method [37] has been used for the determination of weights so as to optimize the radiation pattern. By using the Gaussian basis decomposition, only one parameter w_p needs to be optimized for each basis at one instant, irrespective of the number of loads. It makes this method computationally efficient as well. Similar to the harmonic basis, multiple iterations can be run to reach the minimum of the cost function.

$$Z_{Lmin}^n = j \sum_{p=1}^N w_p \exp\left(\frac{-(n - \mu_p)^2}{2\sigma^2}\right). \quad (2.22)$$

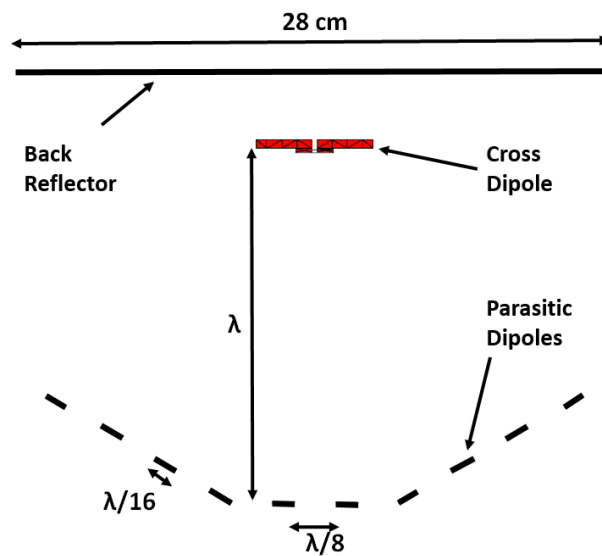
2.5.3 Comparison of Spectral Optimization with Genetic Algorithm

A comparison of the proposed spectral optimization method is made with the genetic algorithm [42], [5] in terms of computation time and minimum value of the cost function achieved. As an example, the active antenna considered is the one presented in [45] for a base station application operating at 1800 MHz. It has two ports with $+45^\circ$ and -45° polarization, the vertically polarized field can be transmitted by simultaneous excitation of both ports. Vertical dipoles are considered as parasitic radiators so that they do not deteriorate the polarization of the fields transmitted by an active element.

The half-wavelength ($\lambda/2$) parasitic dipoles of $\lambda/16$ width (with respect to 1800 MHz) are placed at a distance λ in front of the active antenna, as



(a)



(b)

Figure 2.10: (a) ESPAR antenna with cross dipole (active element) and half-wavelength dipoles (parasitic elements) (b) Top view.

shown in Fig. 2.10. The parasitic dipoles are separated from each other by a $\lambda/8$ distance. In total, 10×3 parasitic radiators are placed in front of the active antenna. There are three sets of dipoles, each arranged on

Table 2.4: Impedances computed for different radiation patterns by using spectral optimization with harmonic basis.

	Case I (0° tilt)	Case II (22° tilt)	Case III (30° tilt)	Case IV (-14° tilt)	Case V (-18° tilt)	Case VI (Multi-beam)
Z_1	-100i	-10i	+4i	-240i	+95i	-480i
Z_2	-16i	+401i	+205i	-16i	-500i	+430i
Z_3	-160i	+36i	+75i	-161i	+12i	+249i
Z_4	+98i	+31i	-32i	+57i	+480i	-419i
Z_5	+198i	-107i	-57i	+119i	+362i	+31i
Z_6	-215i	+106i	-234i	-104i	-360i	+330i
Z_7	+105i	+120i	+262i	+46i	-19i	-500i
Z_8	+74i	-217i	-21i	-6i	-48i	+6i
Z_9	-186i	-13i	-430i	+191i	-138i	+500i
Z_{10}	+31i	-329i	+148i	+17i	-33i	-409i

Table 2.5: Impedances computed for different radiation patterns by using spectral optimization with Gaussian basis.

	Case I (0° tilt)	Case II (22° tilt)	Case III (30° tilt)	Case IV (-14° tilt)	Case V (-18° tilt)	Case VI (Multi-beam)
Z_1	+255i	+3i	-7i	-199i	-500i	-145i
Z_2	+75i	+500i	+498i	-32i	+21i	-55i
Z_3	+438i	0i	+42i	-151i	+500i	-125i
Z_4	-282i	-63i	+29i	+73i	-164i	+124i
Z_5	-5i	-140i	-72i	+108i	-51i	+500i
Z_6	-61i	+500i	-163i	-127i	-99i	+80i
Z_7	+5i	-12i	+30i	+79i	+26i	-175i
Z_8	-135i	-145i	-169i	+14i	+72i	-22i
Z_9	-12i	-20i	-24i	+129i	+114i	+297i
Z_{10}	-126i	-219i	-249i	+38i	+24i	-500i

a flat panel, as shown in Fig. 2.10(b) which provides a top view of the design. The two panels on left and right are tilted at an angle of 30° towards the active element in order to maintain a similar radial distance between all the parasitic dipoles and the active antenna. Each dipole has a load at its terminals. Here, only azimuthal beamforming is considered.

Table 2.6: Genetic algorithm parameters [5].

Parameters	Values
Number of maximum generations (iterations)	1000
Number of initial points	2000
Number of sons for each generation	100
Reproduction probability	0.8
Recombination Probability	0.9
Mutation Probability	0.1
Immigration Probability	0.8
Lower bound for initial points	-250 i Ω
Higher bound for initial points	250 i Ω

Therefore, identical impedances are considered in any given column (three dipoles here). Hence, in total, 10 different loads need to be optimized to implement the beamforming and beam-shaping. For this example, the total number of basis functions involved in the MoM code is 2235. The cost function is defined as the mean-square-error between the parasitic antenna array radiation pattern $\mathbf{f}(\theta, \phi)$ and the objective radiation pattern $\mathbf{f}_{obj}(\theta, \phi)$.

$$\arg \min_{Z_1, \dots, Z_N} \int_0^{2\pi} \int_0^\pi \mathbf{a}(\theta, \phi) [|\mathbf{f}(\theta, \phi)| - |\mathbf{f}_{obj}(\theta, \phi)|]^2 \sin \theta d\theta d\phi$$

Here, $\mathbf{a}(\theta, \phi)$ is a weighting function which is used to give more significance to the main lobe than side lobes of the radiation pattern in the cost function. The active antenna (crossed dipole) is oriented towards the azimuth angle $\phi = 270^\circ$; different beam shapes and beam tilts are obtained by optimizing the loads attached to the parasitic radiators ($\lambda/2$ dipoles). The values of parasitic reactances determined to obtain different desired patterns using the proposed algorithm, are given in Tables 2.4 and 2.5. The radiations patterns show stability over the variation of ± 1 cm ($\pm \lambda/16$) in the relative positioning of active antenna and parasitic radiators and $\pm 5 \Omega$ variation in the optimized impedances.

A comparison of the proposed spectral optimization method with the classical genetic algorithm [5] approach has been made to evaluate its performance in terms of computation time and minimum achieved value of the cost function. For the genetic algorithm, the parameters given in Ta-

Table 2.7: Comparison of figure of merits of harmonic optimization with genetic algorithm.

	Figure of Merits	Harmonic Basis	Gaussian Basis	Genetic Algorithm
Case I	No. of Times Cost Function is Evaluated	10005	7922	72000
	Time (sec)	4.87	3.75	74.48
	Minima Value	0.15	0.11	0.24
Case II	No. of Times Cost Function is Evaluated	8148	8181	72000
	Time (sec)	4	3.92	70.06
	Minima Value	0.29	0.20	0.77
Case III	No. of Times Cost Function is Evaluated	21615	7937	186000
	Time (sec)	10.4	3.97	176.8
	Minima Value	0.3	0.18	0.75
Case IV	No. of Times Cost Function is Evaluated	1622	4037	106000
	Time (sec)	1	2.11	103.74
	Minima Value	0.16	0.18	0.59
Case V	No. of Times Cost Function is Evaluated	13441	8285	386000
	Time (sec)	6.34	4.05	362.4
	Minima Value	0.19	0.22	0.54
Case VI	No. of Times Cost Function is Evaluated	25490	8334	2000000
	Time (sec)	12.5	3.66	1909
	Minima Value	0.26	0.06	0.46

ble 2.6 have been used to reach the minima of a cost function. The performance comparison between the spectral optimization and genetic algorithm in terms of radiation patterns are given in Fig. 2.11, and the comparison of corresponding figures of merit are given in Table 2.7. The comparison shows that, in nearly all cases, the spectral optimization requires fewer iterations and computation time than the genetic algorithm, to obtain better minima of the cost function. For the different cases considered here, on the average, there is a 2.9 times reduction in the value of cost function's minima and 49 times the average reduction in computation time. Therefore,

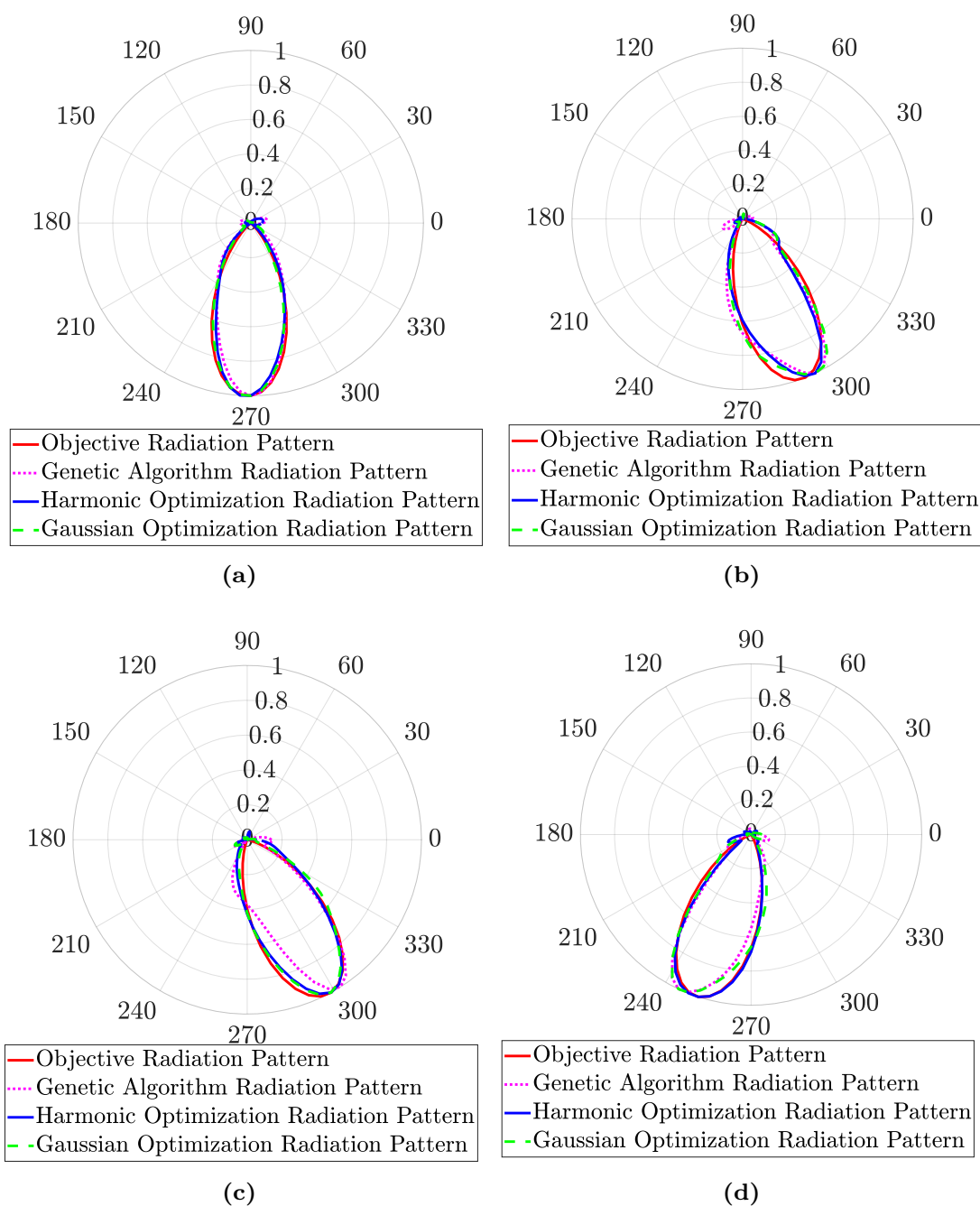


Figure 2.11: Different objective power patterns and the obtained power patterns from the parasitic antenna array using spectral optimization and genetic algorithm, Frequency=1800 MHz, Phi [degrees] vs Linear Scale, (a) case I (0° tilt) (b) case II (22° tilt) (c) case III (30° tilt) (d) case IV (-14° tilt).

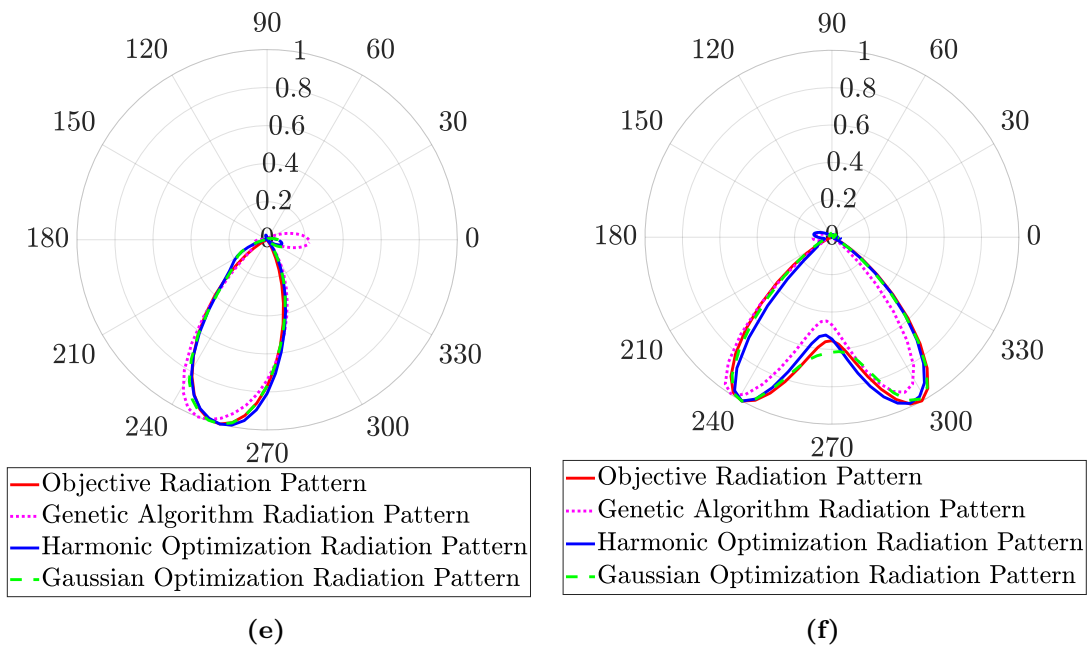


Figure 2.11: Different objective power patterns and the obtained power patterns from the parasitic antenna array using spectral optimization and genetic algorithm, Frequency=1800 MHz, Phi [degrees] vs Linear Scale, (e) case V (-18° tilt) (f) case VI (multi-beam).

spectral optimization proves to be computationally efficient for the design of electronically steerable parasitic array radiators (ESPAR).

2.6 Conclusion

For ESPAR antennas, the open-circuit to embedded pattern approach is a very fast way to compute the exact radiation pattern with the dynamic parasitic loads, without any approximation. Regardless of the optimization algorithm, this approach immensely accelerates the optimization process to find the set of loads producing a radiation pattern as close as possible to a given objective pattern. An analytical method has been explored to determine the loads to form the desired radiation patterns. However, it yields the unrealistic load values to produce the desired radiating patterns. Moreover, the phase profile of the objective radiation patterns also plays a role in the analytical method and the optimum phase profile needs to be determined for

the different desired radiation patterns. A spectral optimization algorithm has been proposed; it decomposes the parasitic loads into discrete basis functions, and the related coefficients are determined to minimize the cost function. The comparison of results obtained with the proposed algorithm with those from a genetic algorithm shows that in average it converges to a slightly better solution (2.9 times reduction in the value of cost function's minima) in 49 times shorter time.

CHAPTER 3

Parasitic Antenna Array

This chapter expresses the work which involves the adaptation of the radiation pattern of a base station antenna by the use of parasitic antenna array to improve the coverage in cellular communication systems, such as 4G or 5G systems. It details the overall employed methodology of the work and explains each step that has been involved in that methodology.

First, based on the cell's geographic topology and the requirements of different radiation power exposure, and using ray-tracing simulation, the desired antenna radiation patterns are determined and represented with spherical harmonics. Secondly, those patterns are implemented in a prototype in the 1800 MHz band using parasitic radiators, loaded with different impedances, placed in front of the existing cellular base station antenna. The developed prototypes have been tested in the laboratory and the measurements are in a good agreement with the simulation results.

Section 3.1 introduces the work that is discussed in this chapter. Section 3.2 details the methodology followed in the work, that is how we go from the coverage improvement in an area to the design of a parasitic antenna array for the base station. Section 3.3 explains the procedure to compute the objective radiation patterns for base stations by using the propagation tools. It has been mainly done by Quentin Gueuning under the supervision

of Claude Oestges. Section 3.4 describes the design procedure of the parasitic antenna array and presents the simulation and experimental results. Section 3.5 shows propagation simulation results to verify that coverage has been improved.

3.1 Introduction

The proliferation of mobile communication technologies has increased the human exposure to Radio Frequency (RF) radiation. The mostly followed standards for Base Station (BS) radiation are published by the International Commission on Non-Ionizing Radiation Protection (ICNIRP) [46], recognized by the World Health Organization (WHO). In a cellular communication system, a BS generally overexposes an area in the line of sight of the main beam and underexposes the rest of the area. In order to improve the coverage in a given area without the risk of potential RF exposure, the radiation pattern of a base station antenna can be adapted according to its environment. In this domain the use of parasitic elements appears as an under-exploited degree of freedom, although it can help to attain lower RF exposure levels for the general public without any major economic impact nor significant reduction of throughput. In this work, parasitic radiators are used in front of the existing base station antennas to modify their radiation patterns, in order to approximately obtain a specific level of field-strength distribution over the coverage area. So, the idea is first to obtain the desired base station radiation pattern, based on propagation simulations in a given area. Then the second step consists of implementing that desired radiation pattern by placing the parasitic radiators with loads in front of the existing base stations.

In [47], the desired (objective) radiation pattern simply consists of an inverse squared cosine function that compensates for the propagation losses for receivers lying within a plane directly below the base station. Moreover, optimization constraints have been added to reduce the interference by limiting the power sent toward nearby cells. In contrast, [48] uses ray-tracing simulations to produce site-specific antenna patterns which enhance the coverage and the delay spread of the channels within a single cell. Hence, the

patterns are shaped according to the geometry of the surrounding streets and buildings. However, since they are obtained from the union of a finite number of small sectors in which the field amplitude is assumed constant, the desired patterns can be discontinuous and highly directive. In this work, Quentin Gueuning has implemented a method similar to [48], except that the patterns are represented through a small set of spherical vector wave functions and that the optimization variables are their associated expansion coefficients. It ensures that the solutions are physical since they satisfy Maxwell's equations and that they are sufficiently smooth to be used for base station antennas of limited size. In this work, the maximum electric field strength of 3 V/m (129.5 dB μ V/m) is considered at 1800 MHz to compute the desired radiation patterns for the base station. It is the maximum allowed electric field strength in Brussels, Belgium.

The next step is to implement the objective radiation patterns by parasitic antenna array at the base station level. The driven antennas (here the existing base station antennas) and parasitic radiators with loads are collectively referred to as a parasitic antenna array. The parasitic antenna array has been designed using the efficient methodology along with harmonic optimization technique explained in Section 2.2 and 2.5.1, respectively. The prototypes have been fabricated; they consist of parasitic radiators and loads in front of the base station antenna, operating at 1800 MHz, to accommodate with the higher frequency band of existing base station antennas.

3.2 Methodology

A two step methodology is employed in this work. In the first step an objective (desired) radiation pattern is computed depending upon the cell's environment, i.e. streets, buildings etc. in order to improve the coverage in that cell while maintaining a total radiated power level below a certain threshold. In the second step the base station's radiation pattern is adapted by parasitic elements to obtain the objective radiation pattern. The methodology employed in this work is illustrated by the flow chart shown in Fig. 3.1. The addressed optimization problem has been divided into two parts. The ray tracing simulations have been carried out for the given geometry of the

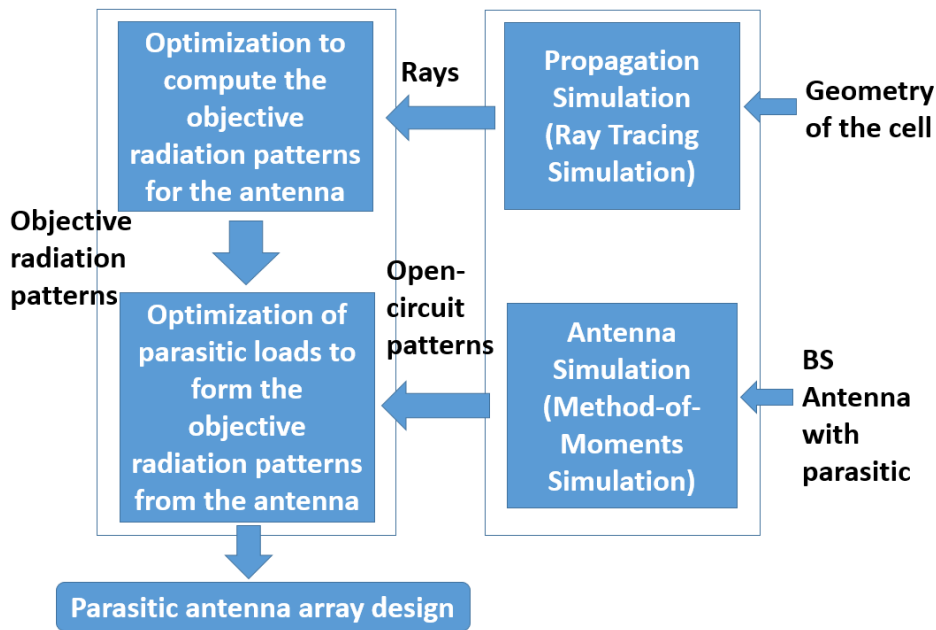


Figure 3.1: Flow chart illustrating the proposed methodology to improve the coverage in a cellular communication by utilizing parasitic antenna array.

cell, using an in-house code. Then the first optimization has been carried out to obtain the objective radiation patterns of the base station antennas, considering the power constraints. The second optimization problem entails the computation of loads of the parasitic antenna array to form the objective radiation patterns, from the existing 4G or 5G base station antennas. An in-house code for the method-of-moments (MoM) has been used for the antenna simulation [49] and then a second optimization process is carried out. In the end, the design of the parasitic antenna array is obtained. This whole process improves the coverage of the cell, by adapting the radiation pattern. The first step is implemented by Quentin Gueuning under the supervision of Claude Oestges. My work deals with the second step which involves the design of beam-shaping parasitic antenna array for BS of a cellular communication system.

3.3 Objective Radiation Patterns

In this section, the formulation of an optimization problem will be presented, based on ray-tracing simulations, which will be solved numerically in order to find the desired (objective) pattern. The determination of objective radiation patterns using ray-tracing simulation has been developed by Quentin Gueuning [35]. The objective pattern is the one that allows to keep the field level below a certain threshold value in a cell while optimizing the throughput. Later, this pattern will be used as an objective function to determine the loads of the parasitic antenna array.

Firstly, let us assume that the three-dimensional objective pattern of the antenna can be decomposed into

$$\mathbf{f}_{obj}(\theta, \phi) = \sum_{n=1}^{2(N+1)^2-2} x_n \mathbf{f}_n(\theta, \phi) \quad (3.1)$$

where x_n are unknown expansion coefficients and \mathbf{f}_n are the vector spherical wave functions [50]. The spherical wave function is defined as:

$$\mathbf{f}_n^m(\theta, \phi) = \sqrt{\frac{2n+1}{4\pi} \frac{(n-m)!}{(n+m)!}} P_n^m(\cos(\theta)) e^{jm\theta} \quad (3.2)$$

Here, $m = (-n, \dots, 0, \dots, n)$ and $P_n^m(\cos(\theta))$ are the associated Legendre polynomials. The antenna radiated power is given by:

$$P = \frac{\mathbf{x}^* \mathbf{x}}{2} \quad (3.3)$$

where \star stands for the transpose conjugate and the coefficients of (3.1) have been stacked into a column vector \mathbf{x} . Typically, a smooth radiation pattern is desired for the design of an antenna. Hence, N will be kept low; i.e. from 2 to 5. Otherwise to form a sharp pattern we will require a larger antenna [51]. The details of the spherical wave functions are given in [52].

Secondly, a ray-tracing simulation leads classically [53] to the following

representation of the electric field at an observation point \mathbf{r} :

$$\mathbf{E}(\mathbf{r}) = \sum_{l=1}^{L(\mathbf{r})} \mathbf{D}_l(\mathbf{r}) \mathbf{f}(\theta_l, \phi_l) \quad (3.4)$$

where $L(\mathbf{r})$ is the number of rays propagating from the antenna to the observation point, (θ_l, ϕ_l) are the departure angles of ray l from the antenna and \mathbf{D}_l is a 3×3 matrix that accounts for electromagnetic interactions with the geometry of the buildings.

Then, by inserting (3.1) into (3.4), the field intensity (in W/m^2) associated to each ray is expressed through a quadratic form as:

$$I_l(\mathbf{r}) = \mathbf{x}^* \mathbf{Q}_l(\mathbf{r}) \mathbf{x} \quad (3.5)$$

where \mathbf{Q}_l is a $N \times N$ matrix and its element ij is given by:

$$Q_l^{ij}(\mathbf{r}) = \frac{1}{2\eta} \mathbf{f}_i^*(\theta_l, \phi_l) \mathbf{D}_l^*(\mathbf{r}) \mathbf{D}_l(\mathbf{r}) \mathbf{f}_j(\theta_l, \phi_l) \quad (3.6)$$

where η is the free-space impedance. Knowing that the phase of each ray field cannot be predicted due to the inaccuracy of the geometrical modelling of the buildings, it is reasonable to assume that rays reaching an observation point \mathbf{r} are uncorrelated. Hence, in the mean sense, the total intensity is given by the sum of that of each rays:

$$\mathbf{Q}(\mathbf{r}) = \sum_l \mathbf{Q}_l(\mathbf{r}) \quad (3.7)$$

From there, an optimization problem is formulated for enhancing the coverage of a base station within a certain surrounding built area Ω . More precisely, the objective is to maximize the field intensity I within Ω while keeping the power P radiated by the antenna constant. This is formulated

as:

$$\begin{aligned} \min_{\mathbf{x}} \quad & -\mathbf{x}^* \sum_i \mathbf{Q}(\mathbf{r}_i) \mathbf{x} \\ \text{s.t.} \quad & P = \frac{\mathbf{x}^* \mathbf{x}}{2} \end{aligned} \quad (3.8)$$

where $\mathbf{r}_i \in \Omega$. In Section 3.5, the numerical solution of (3.8) has been obtained with the help of the interior point algorithms implemented in Matlab [37] language by Quentin Gueuning.

3.4 Parasitic Antenna Array

The objective here is to carry out the beam-shaping and obtain the objective radiation patterns from the existing base station antennas without replacing them. Therefore, parasitic radiators with different loads are placed in front of the existing base station antenna to form the parasitic antenna array. The set of parasitic loads which form different objective radiation patterns are computed efficiently, which is crucial to the design process of a parasitic antenna array.

3.4.1 Driven Antennas of the Parasitic Antenna Array

The driven antennas considered here are the base station antennas, typically used for Long-Term Evolution (LTE) communication system. Such base station antenna consists of 10 crossed dipoles vertically stacked with dual polarization of $+45^\circ/-45^\circ$ [3]. For transmission, the base stations transmit vertically polarized waves by simultaneously exciting the $+45^\circ/-45^\circ$ arms of each crossed dipole. In this work the transmission scenario is considered with vertical polarization only. The antenna also has a back reflector; it transmits only in a sector of about 64° in a horizontal plane (half power beam-width) and about 6.8° in a vertical plane (half power beam-width). The narrow beam in the vertical plane is achieved through beamforming, using a corporate feeding network implemented with coaxial cables. The design details of the base station antenna itself are not given here for confidentiality reasons. The frequency of operation considered is 1800 MHz, as

it is in use for LTE mobile communication. The bandwidth requirement for LTE applications is usually 20 MHz [54].

3.4.2 Design of Parasitic Elements of the Parasitic Antenna Array

The parasitic radiators considered are printed half-wavelength vertical dipoles. Hence, they only impact the directional distribution of fields transmitted by the driven antennas; not their polarization. The parasitic elements themselves need to be essentially resonant to have sufficient impact on the radiation patterns. Moreover, as open radiating structures, their intrinsic bandwidth is not extremely narrow (about 2%) such that that the bandwidth of the parasitic elements is not critically limiting the bandwidth of the whole system.

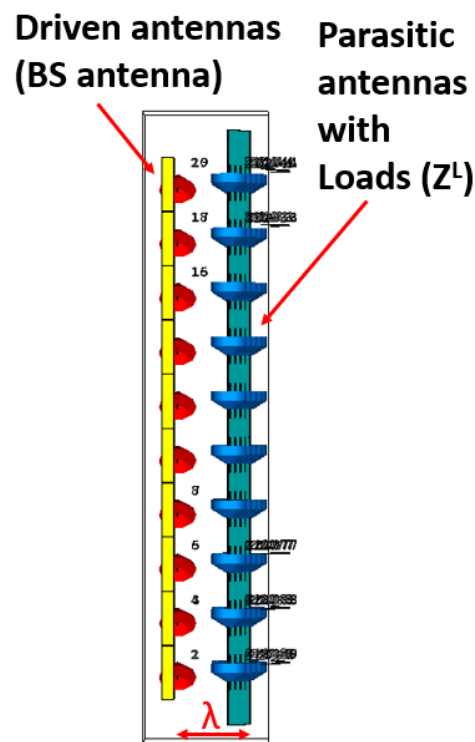


Figure 3.2: Parasitic antenna array design for base station: side view.

It has been noticed that, if parasitic dipoles are placed at a distance smaller than a half-wavelength ($\lambda/2$), they disrupt the matching of exist-

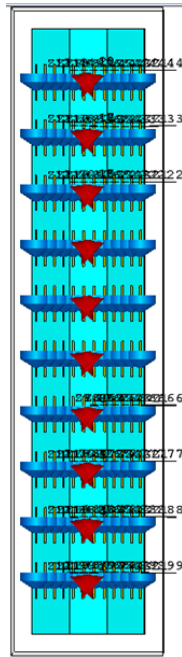


Figure 3.3: Parasitic antenna array design for base station: interior front view.

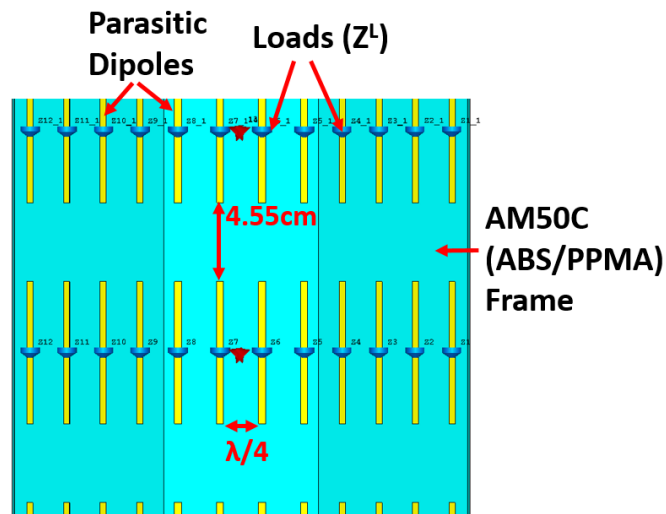


Figure 3.4: Parasitic antenna array design for base station: interior front view.

ing base station antennas. A distance between $\lambda/2$ and λ is appropriate to have a strong mutual coupling between driven (active) and parasitic elements without significantly affecting the matching of the driven elements.



Figure 3.5: Parasitic antenna array design for base station: top view.

Therefore, the parasitic dipoles are placed at a distance λ from the BS antenna, as shown in Fig. 3.2. The parasitic dipoles are placed at a $\lambda/4$ distance from each other, as depicted in Fig. 3.4. In front of each driven crossed dipole of the BS antenna, 12 parasitic dipoles are placed, therefore a total of 12×10 parasitic dipoles and loads are placed in front of the 10 driven elements (BS antenna), as shown in Fig. 3.3. The vertical distance between the rows of parasitic dipoles is 4.55 cm, where each row of 12 parasitic dipoles is aligned in front of each driven element of the base station antenna, as shown in Fig. 3.4. There are three sets of parasitic dipoles, each made of a flat panel containing 4×10 dipoles as shown in Fig. 3.5 which provides a top view of the antenna array. The two panels on left and right sides are tilted at an angle of 30° towards the driven elements (BS antenna) in order to maintain a similar radial distance between all the parasitic dipoles and the driven antennas.

3.4.3 Electromagnetic Model for the Simulations

A computationally efficient Electromagnetic (EM) model, detailed in Section 2.2, is exploited here to design the parasitic antenna array. It employs the open-circuit pattern to embedded pattern transformation. The open-circuit patterns of all antennas (active or parasitic) are computed once and for all. Then all the embedded patterns for a given set of loads can be computed using (3.9). It utilizes the open-circuit patterns of all driven and parasitic elements, as well as the array impedance matrix, to include all the mutual coupling information. The embedded element pattern of all the antennas are computed from the open-circuit patterns through following equation [7], [43], [14]:

$$\mathbf{f}^e = (\mathbf{Z}^a + \mathbf{Z}^L)^{-1} \mathbf{f}^{O.C.} \quad (3.9)$$

Here \mathbf{f}^e are the embedded patterns, $\mathbf{f}^{O.C.}$ are the open-circuit patterns, \mathbf{Z}^L is a diagonal matrix containing the load impedances attached to the driven and parasitic elements, \mathbf{Z}^a is the N -port impedance matrix containing mutual coupling information. In \mathbf{f}^e and $\mathbf{f}^{O.C.}$ matrices, each row corresponds to a given antenna and each column corresponds to a given direction. Since, the radiation pattern of the array is obtained by the superposition of the embedded patterns of the driven elements only, beam-shaping can be implemented by just varying the loads attached to the parasitic radiators. The \mathbf{Z}^a matrix and open-circuit patterns of all the antennas are computed once and saved in memory. Only the embedded patterns are to be recomputed by superposition according to (3.9), for different load terminations. It makes this approach computationally efficient for the calculation of \mathbf{Z}^L , as there is no need to re-simulate the whole array for different load terminations. The parasitic loads are the main dynamic design parameters of a parasitic antenna array which form different radiation patterns.

A method-of-moments (MoM) code developed in-house is used for the simulation of the parasitic antenna array, the code computes the equivalent electric currents on a metallic structure and the equivalent electric and magnetic currents on a dielectric structure of the antenna array [49], [55]. Equivalence principle is the basis of the MoM code in which an object is replaced by fictitious electric and magnetic currents flowing on a surface enclosing the object. On a metallic structure, the tangential electric field is zero which means the equivalent magnetic currents are zero as well. Hence, only equivalent electric currents (which in our case are physical currents) are sufficient to compute the fields radiated by a metallic object. However, in case of a dielectric object, boundary conditions suggest the continuity of tangential electric and magnetic fields on the surface of a dielectric object. Therefore, both equivalent electric and magnetic currents are required to determine the scattered fields by a dielectric object. In MoM simulation, a delta-gap excitation has been used for the feeding of the antenna. First, electric and magnetic currents are determined using the MoM simulation and then the scattered fields are computed using Kottler's formula [56]. The antenna geometry and mesh are created using the Gmsh [57] software.

3.4.4 Computation of the Parasitic Loads

The computation (optimization) of loads in a parasitic antenna array is a non-linear problem, which makes it really difficult to efficiently find the set of loads that yields the desired radiation pattern. Therefore the optimization algorithm is crucial to the design of parasitic antenna arrays. The mean-square-error between the parasitic antenna array radiation pattern and the objective radiation pattern is used as a cost function; it is minimized by varying the loads in order to obtain the radiation pattern with desirable characteristics. The parasitic loads considered are purely imaginary (capacitive or inductive) because the real part of the impedance introduces losses. If $\mathbf{f}(\theta, \phi)$ is an array radiation pattern, $\mathbf{f}_{obj}(\theta, \phi)$ is an objective radiation pattern and $\mathbf{a}(\theta, \phi)$ is a weighting function, then the cost function is defined as:

$$\arg \min_{Z_1, \dots, Z_N} \int_0^{2\pi} \int_0^\pi \mathbf{a}(\theta, \phi) [|\mathbf{f}(\theta, \phi)| - |\mathbf{f}_{obj}(\theta, \phi)|]^2 \sin \theta \, d\theta \, d\phi$$

Here, only azimuthal beamforming is considered, therefore, in every column identical loads are considered. Hence, in this design, there are 12 different parasitic loads in each column of a given row while in one column all 10 rows have the same load. The harmonic optimization presented in Section 2.5.1 is used to minimize the cost function efficiently. It considers the loads along a line or a circle, and the load values are decomposed into spatial harmonics according to the positions of the parasitic elements. The optimum load configuration can be expressed as a summation of sines and cosines of different harmonics, as given in (3.10). For each harmonic, the amplitudes of sines and cosines are optimized, such that the radiation pattern obtained with the sum of harmonics minimizes the cost function. The equations (3.9) and (3.10) are used in conjunction to determine (optimize) the parasitic loads \mathbf{Z}^L to obtain different objective radiation patterns.

$$Z_{Lmin}^n = j \sum_{p=1}^N \left(a_p \cos \frac{2\pi np}{N} + b_p \sin \frac{2\pi np}{N} \right) \quad (3.10)$$



Figure 3.6: Base station antenna for a sector in a cellular communication [3].

Here N is the total number of parasitic loads, p is the harmonic being optimized, n is the element index, a_p and b_p are the purely real amplitudes of cosines and sines, respectively.

3.4.5 Simulation Results of the Parasitic Antenna Array

The base station antenna [3] shown in Fig. 3.6 is simulated using MoM; the 3D and the 2D radiation patterns at 1800 MHz are shown in Fig. 3.7 and 3.8, respectively. This antenna is used to cover a sector of a base station, it has a back reflector which makes its radiation pattern directive in the azimuth plane. There are multiple antennas stacked vertically inside the casing, which makes it even more directive in the elevation plane.

The parasitic antenna array consisting of a base station antenna (driven antennas) and printed parasitic dipoles with loads on their terminals is shown in Fig. 3.9. The dielectric material AM50C (ABS/PPMA) ($\epsilon_r = 2.89$ and $\tan \delta = 0.005$ at 1800 MHz) of 3 mm thickness has been used to make the frame for parasitic dipoles as shown in Fig. 3.4. The parasitic antenna array with a certain set of loads is simulated with MoM code when dielectric material is considered and when it is ignored; the comparison of the radiation patterns is shown in Fig. 3.11. The difference signifies the importance of considering the dielectric in EM simulations. Therefore, the parasitic antenna array is simulated using the MoM code which takes dielectric material into account. The parasitic loads values are determined to obtain

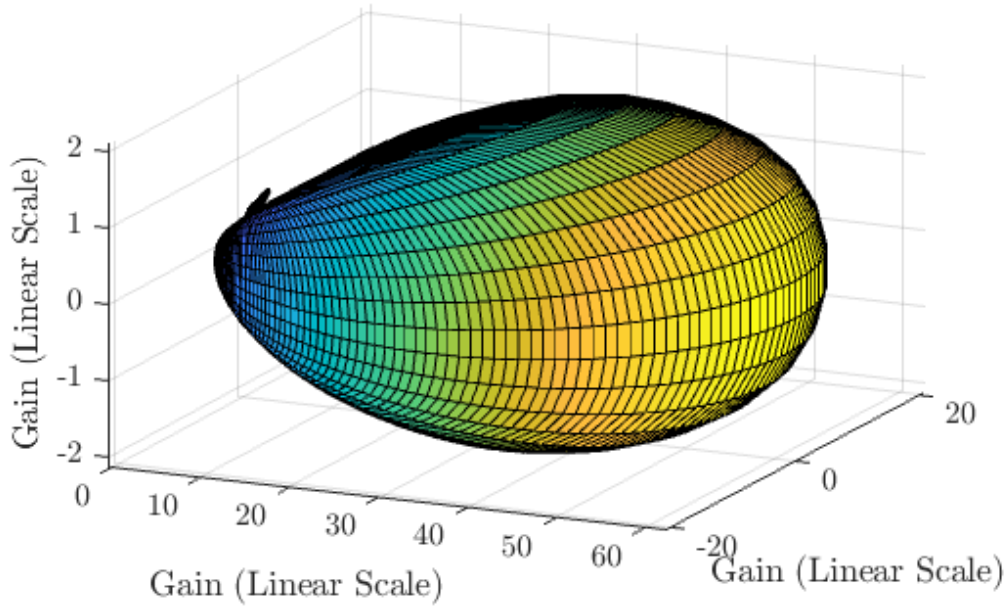


Figure 3.7: 3D Radiation pattern of base station antenna, Frequency=1800 MHz (MoM simulation).

different objective radiation patterns. The loads values are determined by using EM model in conjunction with the harmonic optimization explained in Subsection 3.4.3 and Subsection 3.4.4, respectively. The simulation results are shown in Fig. 3.12, Fig. 3.13 and Fig. 3.14. The corresponding optimized loads Z^L are given in Table 3.1, 3.2 and 3.3, respectively. The base station antenna is facing towards $\phi = 270^\circ$, and by changing the loads attached to the parasitic radiators beamforming and beam-shaping is achieved. Case I and Case II contains two of the optimized objective patterns obtained through the propagation tools described in Section 3.3. In Case III the objective pattern is synthesized to check the beam-shaping capabilities of the parasitic antenna array. The relative errors between the objective and obtained patterns (simulations) are -10.5 dB, -9.4 dB and -11.3 dB for Case I, Case II and Case III, respectively. The relative errors have been computed using the following relation:

$$Error_{dB} = 10 \cdot \log_{10} \left[\frac{\int_0^{2\pi} (|\mathbf{F}_{obj}| - |\mathbf{F}_{obtained}|)^2 d\phi}{\int_0^{2\pi} |\mathbf{F}_{obj}|^2 d\phi} \right] \quad (3.11)$$

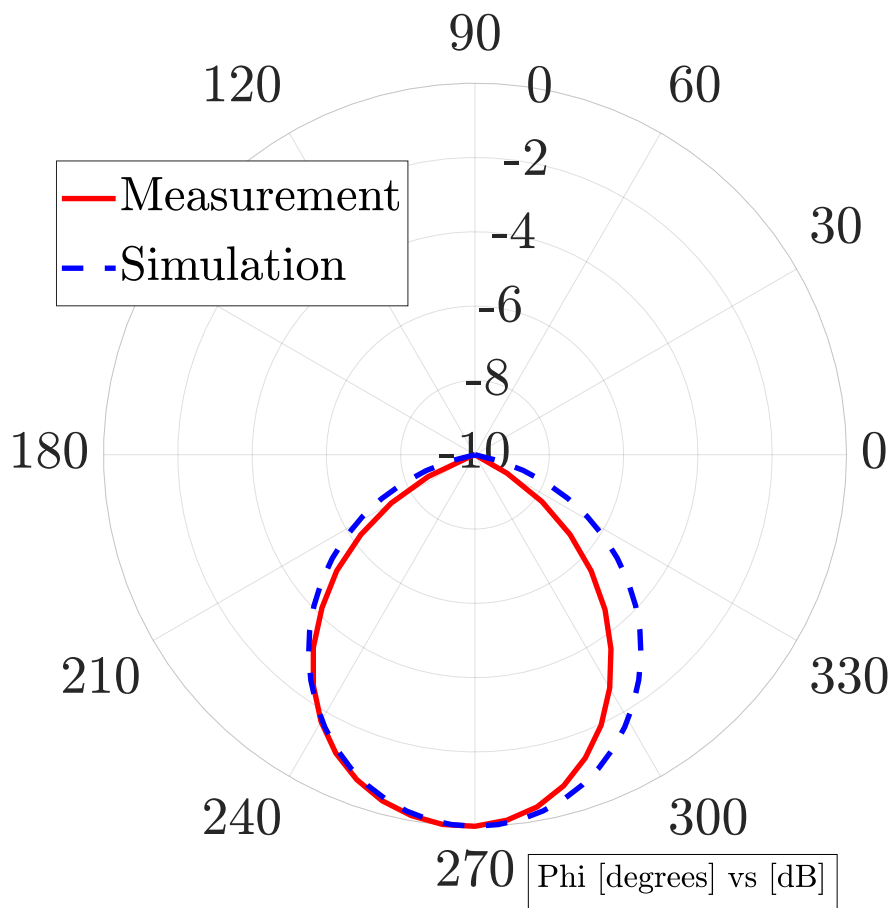


Figure 3.8: Azimuthal power pattern of base station antenna, Frequency=1800 MHz (MoM simulation vs measurement).

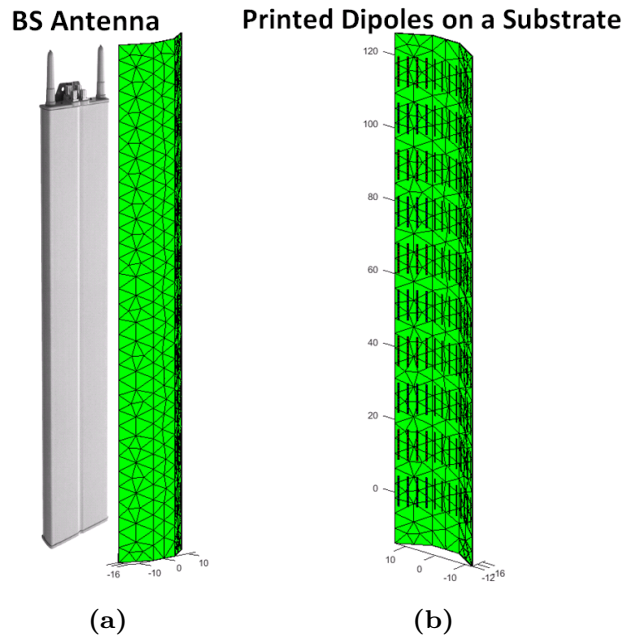


Figure 3.9: (a) Base station antenna [3] and printed parasitic dipoles on a substrate with loads. (b) Interior front of printed parasitic dipoles on a substrate with loads.

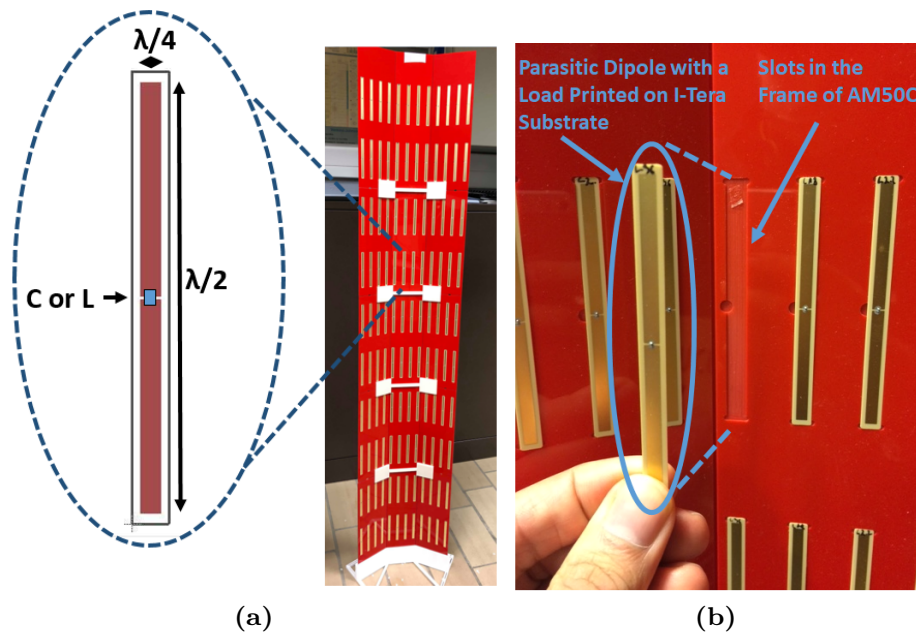


Figure 3.10: (a) Fabricated prototype consisting of printed dipole on I-Tera with capacitors or inductors, the frame is made of AM50C material (b) Zoom view.

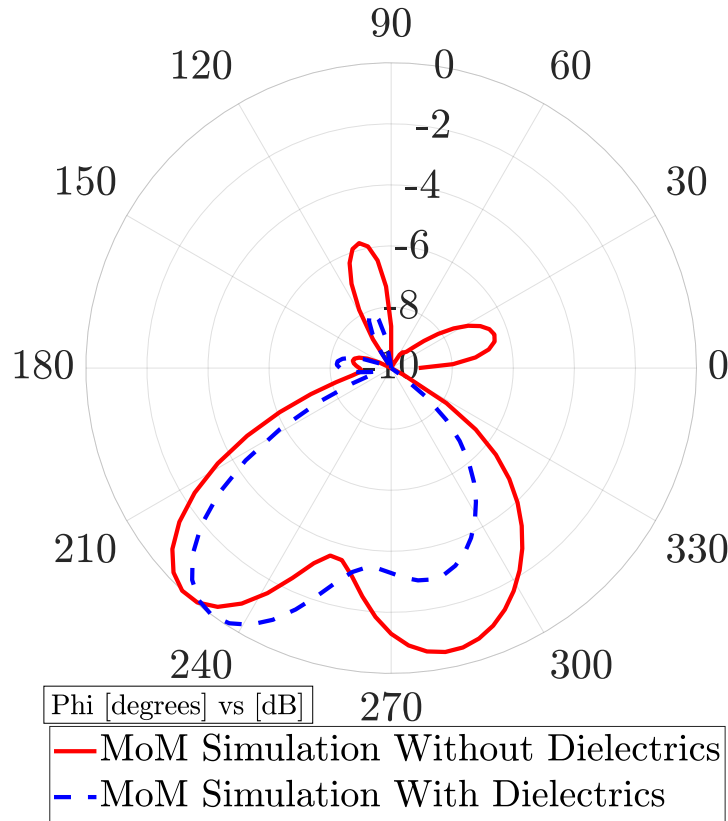


Figure 3.11: Azimuth power pattern of the parasitic antenna array for a certain set of loads with and without dielectric, MoM simulation, Frequency=1800 MHz.

For the design of the parasitic antenna array, the losses in the structure are taken into account. The comparisons of the maximum gain and efficiency (MoM simulation) of the BS antenna with and without the parasitic elements are given in Table 3.4. It can be seen that more gain can be obtained with the use of parasitic elements, if the objective pattern is narrow with low side lobe levels and the dielectric losses and the ohmic losses in the parasitic loads are not significant. In order to scan a beam at wider angles with low SLLs, parasitic elements should surround the driven antenna at wider angles. A rule of thumb we have established through simulations is that a beam can be scanned with low SLLs in the range of $\pm(\alpha - HPBW/2)$, where α is the widest angle at which a parasitic element is placed from broadside and HPBW is the half power beam width of the

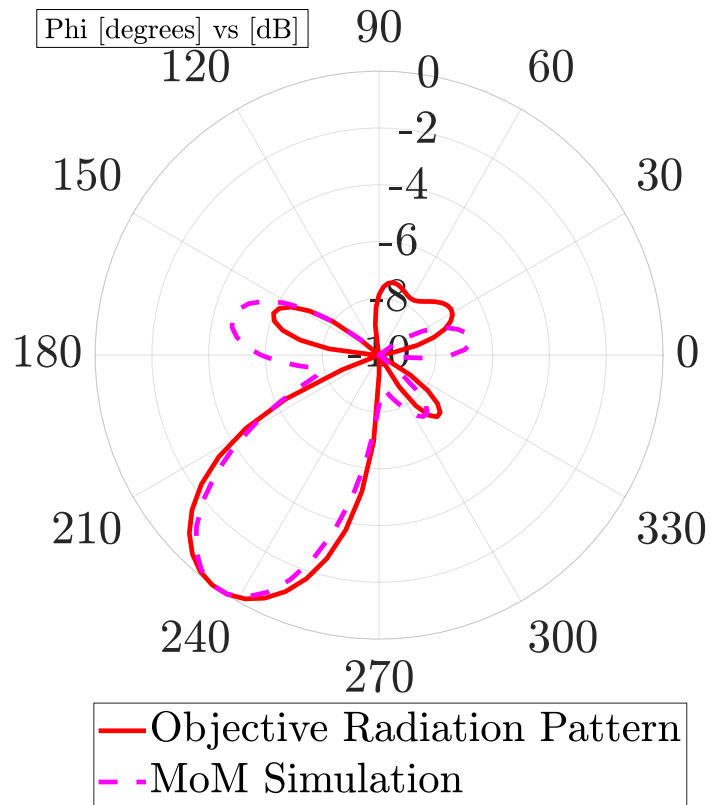


Figure 3.12: Azimuthal objective power pattern and obtained simulated (MoM) power pattern from the parasitic antenna array, Case I, Frequency=1800 MHz.

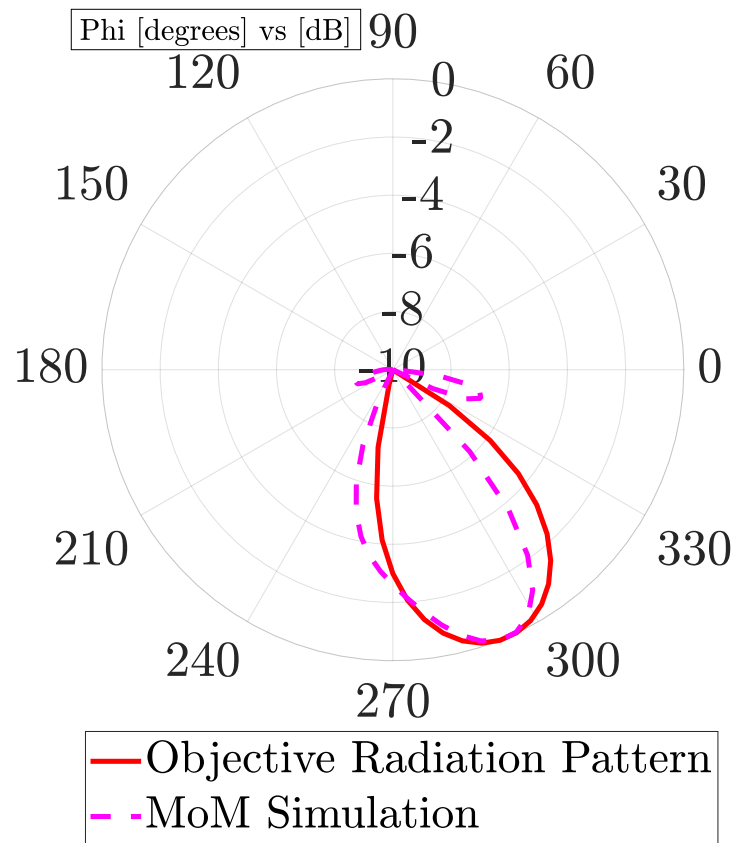


Figure 3.13: Azimuthal objective power pattern and obtained simulated (MoM) power pattern from the parasitic antenna array, Case II, Frequency=1800 MHz.

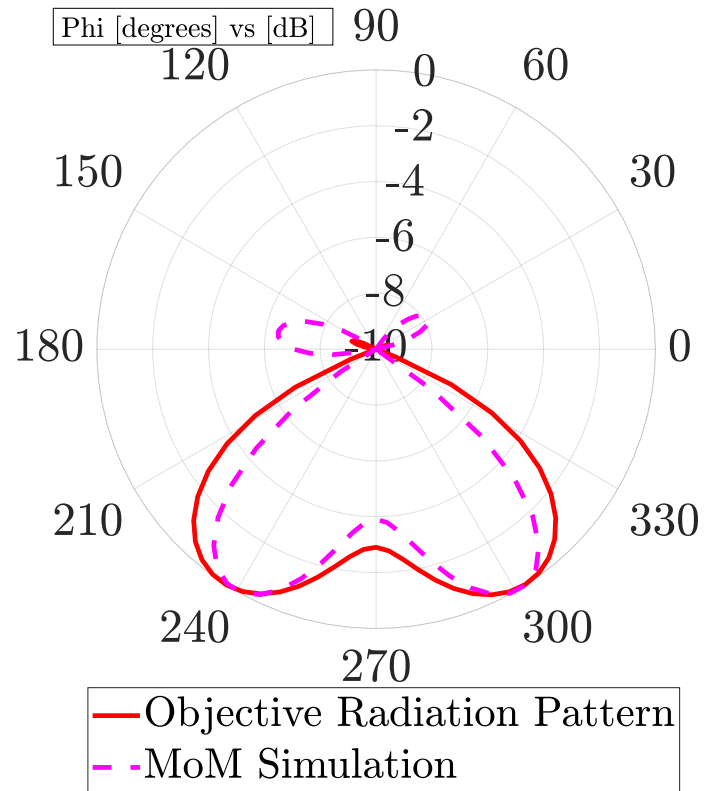


Figure 3.14: Azimuthal objective power pattern and obtained simulated (MoM) power pattern from the parasitic antenna array, Case III, Frequency=1800 MHz.

Table 3.1: Parasitic reactances computed using harmonic optimization for the Case I radiation pattern shown in Fig. 3.12.

Case I	
Parasitic Reactance	Component
308i	27.23nH
305i	26.96nH
292i	25.81nH
264i	23.34nH
181i	16nH
172i	15.2nH
115i	10.16nH
265i	23.43nH
159i	14.05nH
-108i	0.818pF
-75i	1.17pF
-41i	2.15pF

Table 3.2: Parasitic reactances computed using harmonic optimization for the Case II radiation pattern shown in 3.13.

Case II	
Parasitic Reactance	Component
12i	1.06nH
-21i	4.2pF
227i	20nH
248i	21.9nH
38i	3.35nH
-520i	0.170pF
-370i	0.238pF
150i	13.26nH
-53i	1.67pF
-504i	0.175pF
-374i	0.236pF
87i	7.7nH

scanned beam.

Table 3.3: Parasitic reactances computed using harmonic optimization for the Case III radiation pattern shown in Fig. 3.14.

Case III	
Parasitic Reactance	Component
-476i	0.1857pF
-352i	0.251pF
-43i	2.075pF
552i	48.79nH
516i	45.65nH
444i	39.28nH
31i	2.73nH
-251i	0.352pF
-16i	5.46pF
-136i	0.648pF
61i	5.38nH
-331i	0.267pF

Table 3.4: Maximum gain and efficiency of the BS antenna with and without the parasitic elements, MoM simulation at 1800 MHz.

	Maximum Gain [dB]	Efficiency [%]
BS antenna	17.83	98
BS antenna Case-I	18.4	73
BS antenna Case-II	18.75	52
BS antenna Case-III	17.9	80

3.4.6 Realization of the Parasitic Radiators with Loads

The parasitic dipoles are printed on I-Tera substrate ($\epsilon_r = 3.38$ and $\tan \delta = 0.0028$ at 2 GHz) [58], the capacitors and inductors computed from the optimized impedances are soldered across the dipole terminals. A frame of material AM50C (ABS/PPMA) ($\epsilon_r = 2.89$ and $\tan \delta = 0.005$ at 1800 MHz) of 3 mm thickness is built with slots in it to place the parasitic elements. Then printed dipoles on the I-Tera with capacitors or inductors are placed into the frame as shown in Fig. 3.10. The frame is placed at a distance λ from the base station antenna to obtain the objective radiation pattern.

Since the fixed capacitors and inductors are placed onto the dipole terminals, only a fixed beam scanning is obtained with this prototype (no elec-

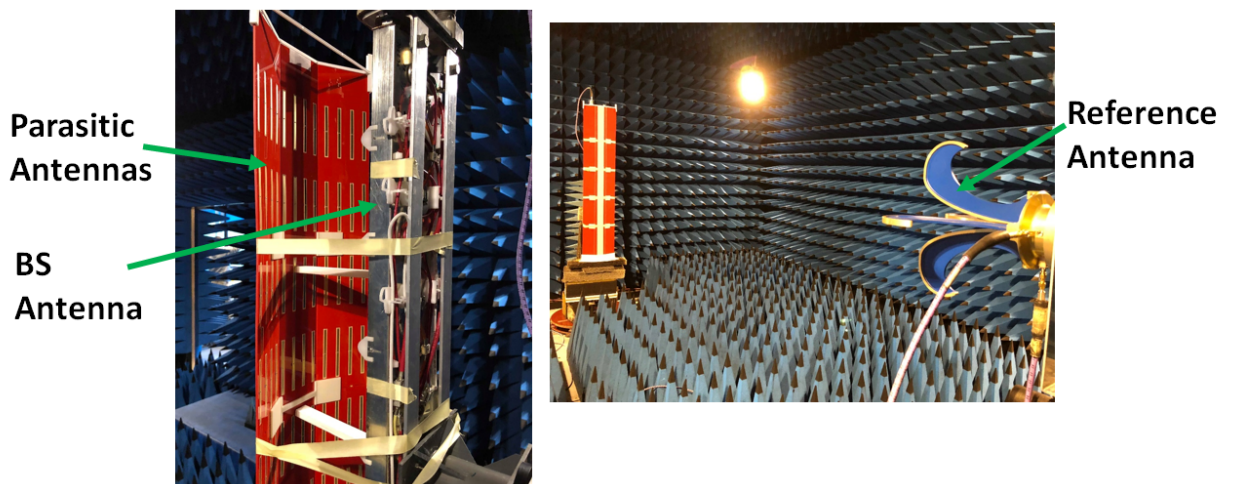


Figure 3.15: Measurement set-up of the parasitic antenna array.

tronic scanning). Three different prototypes are fabricated, requiring three different sets of loads, to obtain three different radiation patterns from the same base station antenna. In order to achieve the electronic beam scanning, varactors are required to provide the dynamic impedances, which will be explained in Chapter 4. For the proposed parasitic antenna array, 120 varactors will be required which entails the challenge of their biasing. In a given column, the loads are identical, because azimuthal beamforming is considered here. Therefore, if varactors are utilized, all the varactors in a single column will require a common biasing voltage. Moreover, in order to minimize the scattering from the biasing lines of varactors, biasing lines can be run through the parasitic dipoles from top to bottom of the array and we will need inductors/chokes to cut RF field.

3.4.7 Measurement Results of the Parasitic Antenna Array

The radiation pattern of the base station antenna is measured in an anechoic chamber and its comparison with the simulation results is shown in Fig. 3.8. After that, the radiation patterns of parasitic antenna array are measured by placing the prototypes in front of the base station antenna as shown in Fig. 3.15. The schematic of the measurement set-up is shown in Fig. 3.16. The measured radiation patterns obtained with the three different prototypes are compared with the simulated patterns (MoM and CST [38])

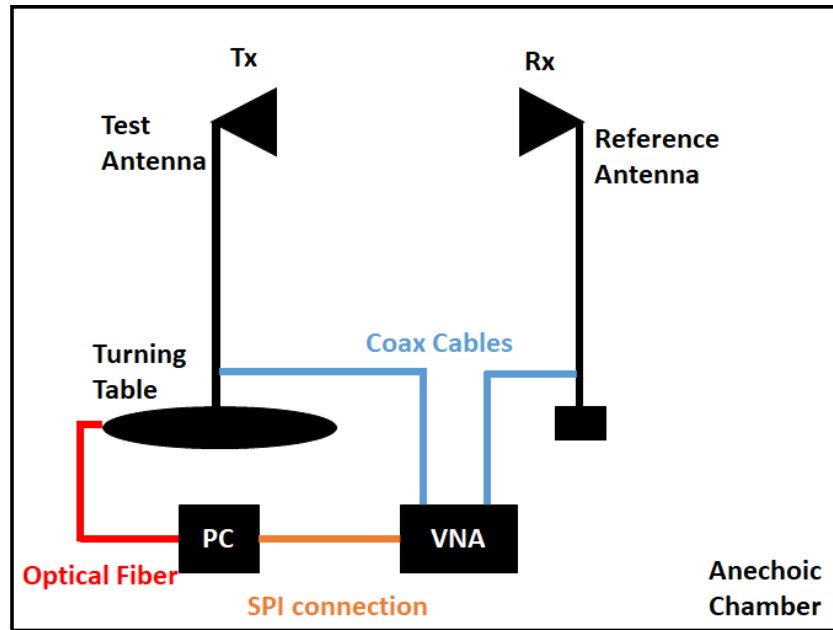


Figure 3.16: Schematic figure of the measurement set-up.

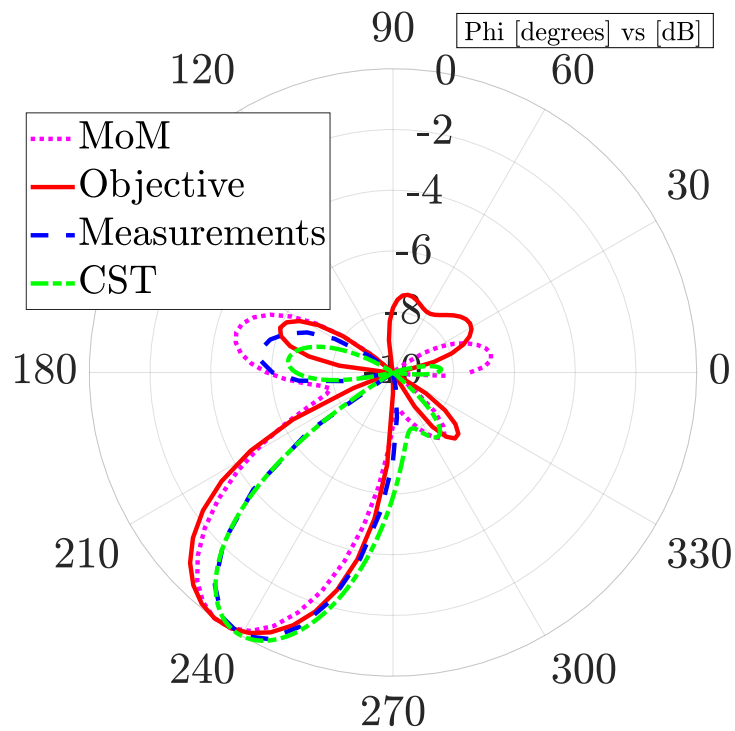


Figure 3.17: Comparison of azimuthal objective power pattern, obtained simulated (MoM, CST) and measured power patterns from the parasitic antenna array, Case I, Frequency=1800 MHz.

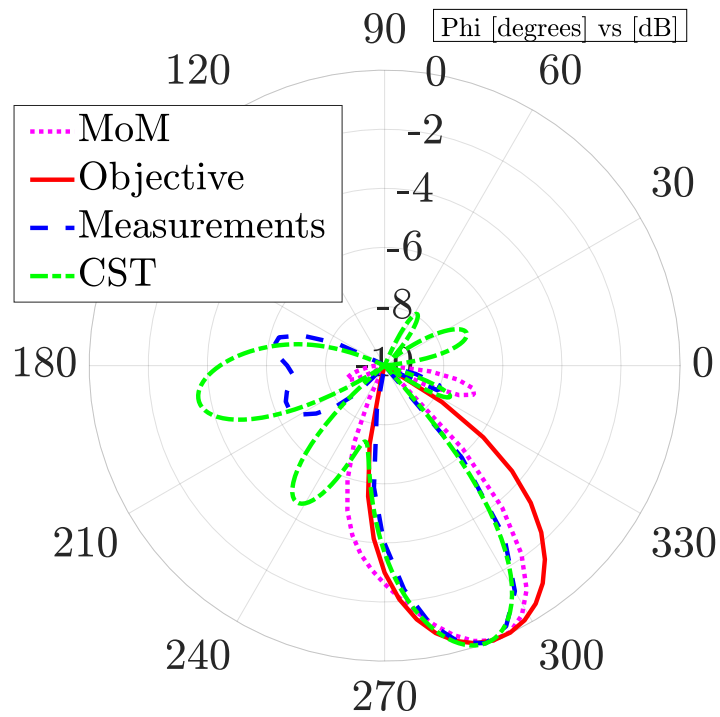


Figure 3.18: Comparison of azimuthal objective power pattern, obtained simulated (MoM, CST) and measured power patterns from the parasitic antenna array, Case II, Frequency=1800 MHz.

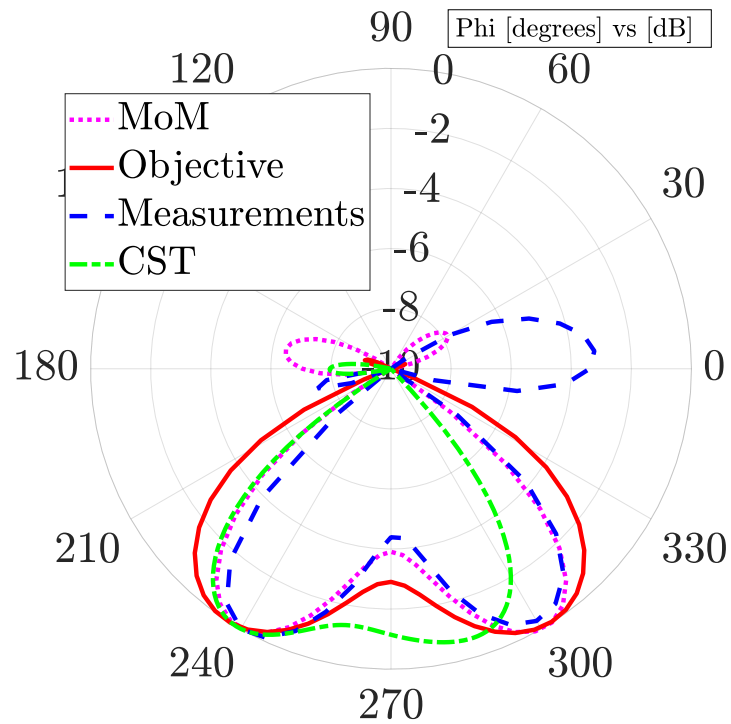


Figure 3.19: Comparison of azimuthal objective power pattern, obtained simulated (MoM, CST) and measured power patterns from the parasitic antenna array, Case III, Frequency=1800 MHz.

Table 3.5: Maximum gain of the BS antenna with and without the parasitic elements, measured at 1800 MHz.

	Maximum Gain [dB]
BS antenna	16.11
BS antenna Case-I	16.91
BS antenna Case-II	16.55
BS antenna Case-III	16.31

and with the the objective radiation patterns, as shown in Fig. 3.17, 3.18 and 3.19. This comparison shows a good agreement between the objective patterns, simulated patterns (MoM) and measured patterns. Slightly higher side-lobe levels in measured patterns can be attributed to inaccuracies in the alignment of parasitic elements with respect to driven elements. The relative errors (3.11) between the objective patterns and obtained patterns (measurements) are -8.35 dB, -7.4 dB and -8.56 dB for Case I, Case II and Case III, respectively. The radiation patterns are measured across the bandwidth of 20 MHz to cater for LTE applications [54]. The stability of radiation patterns versus frequency can be appreciated in Fig. 3.20, 3.21 and 3.22.

The measured maximum gains of the BS antenna with and without parasitic elements are given in Table 3.5. The measured maximum gains are less than those of the simulations, given in Table 3.4. However, a slight variation in the parameters of link budget can make the measured maximum gain and efficiency higher or lower. The radiation patterns are measured only in the horizontal plane. In order to measure the efficiency, we need to measure the 3D patterns. The set-up we have in the anechoic chamber, it is difficult to measure the 3D patterns because the antennas are cumbersome and heavy for our tuning table in the lab.

One of the issues in the design of parasitic antenna array is the deterioration of the reflection coefficient S_{11} of the driven antenna in the presence of parasitic elements, due to strong mutual coupling. Here, since the parasitic elements are placed at a one-wavelength distance, the deterioration of the reflection coefficient of a base station antenna is not significant, and S_{11} is still under -10 dB from 1.6 GHz to 2.5 GHz. Fig. 3.23 gives the comparison

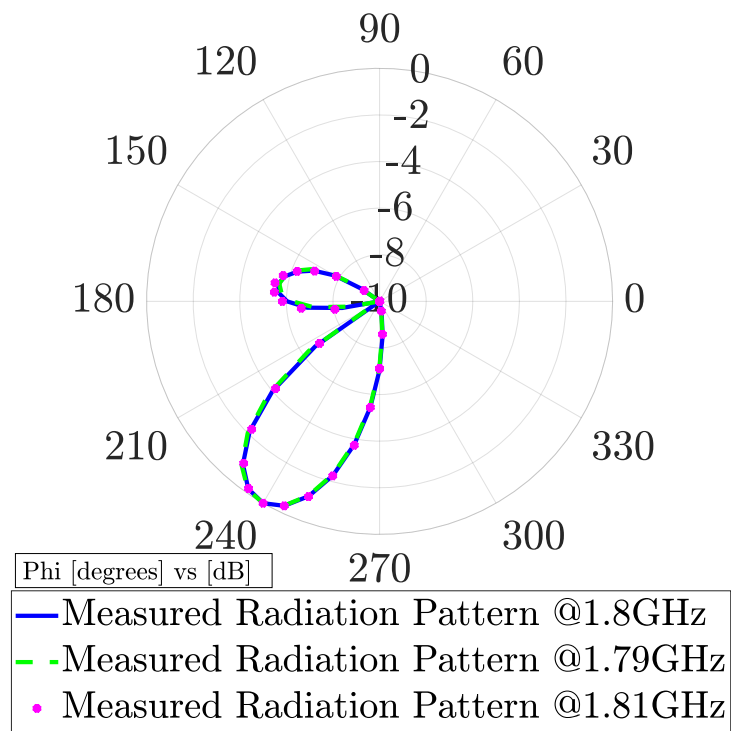


Figure 3.20: Variation of measured azimuthal power pattern of the parasitic antenna array versus frequency, Case I.

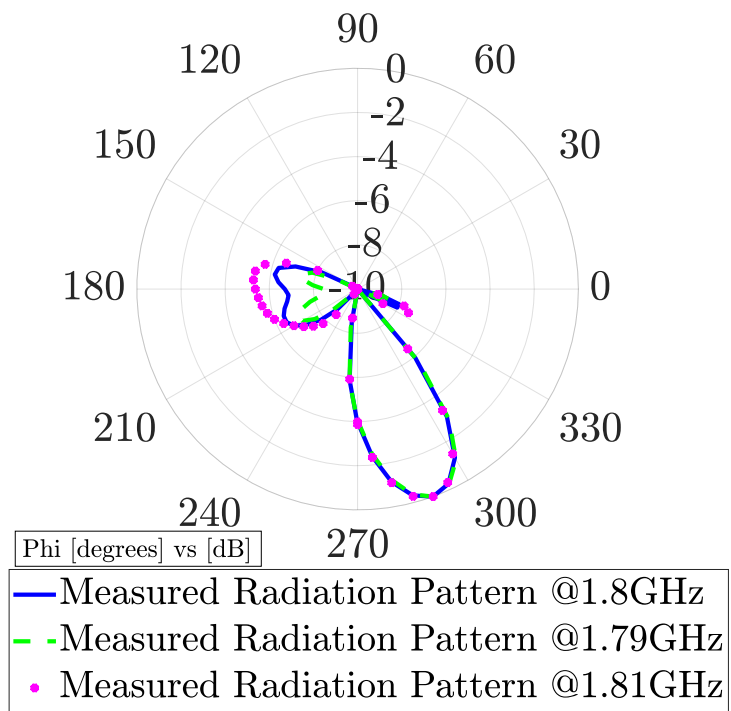


Figure 3.21: Variation of measured azimuthal power pattern of the parasitic antenna array versus frequency, Case II.

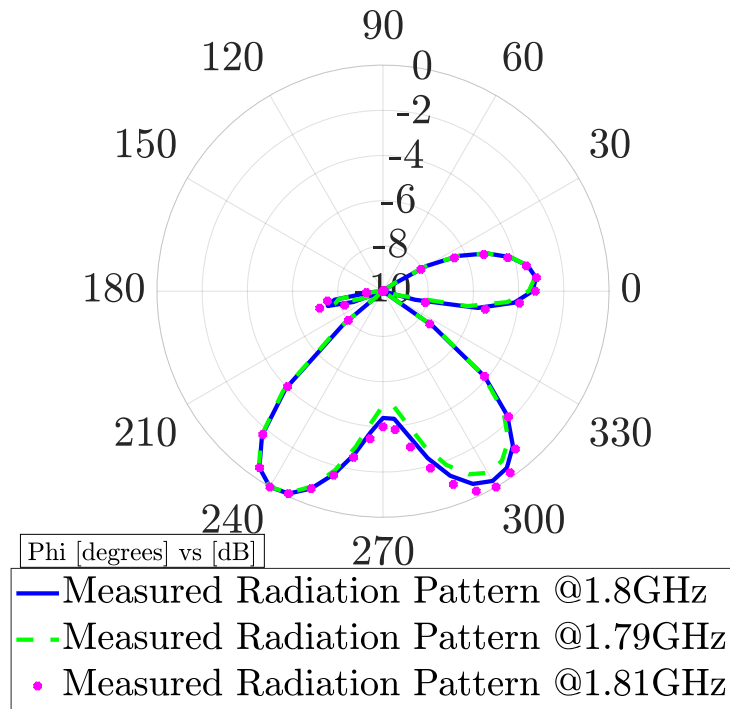


Figure 3.22: Variation of measured azimuthal power pattern of the parasitic antenna array versus frequency, Case III.

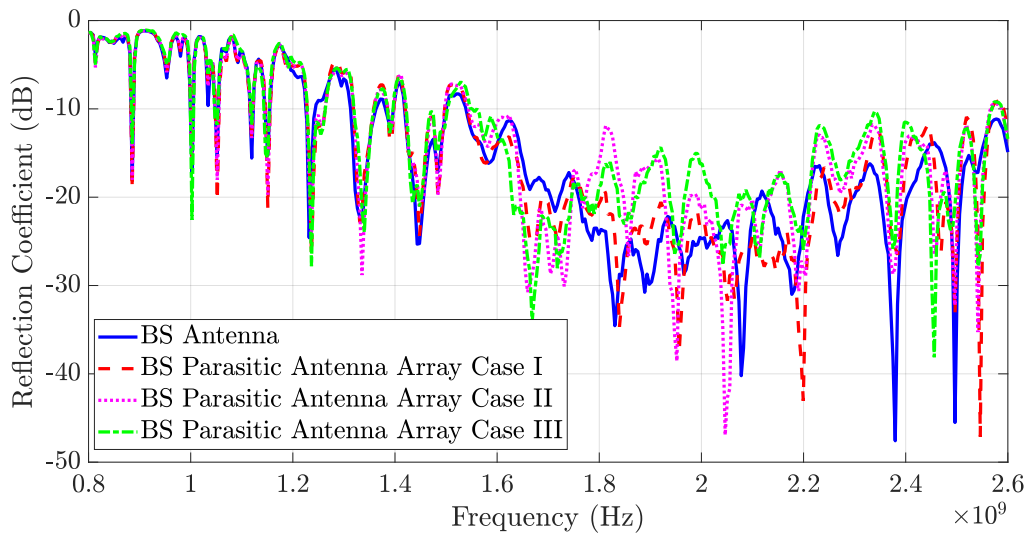


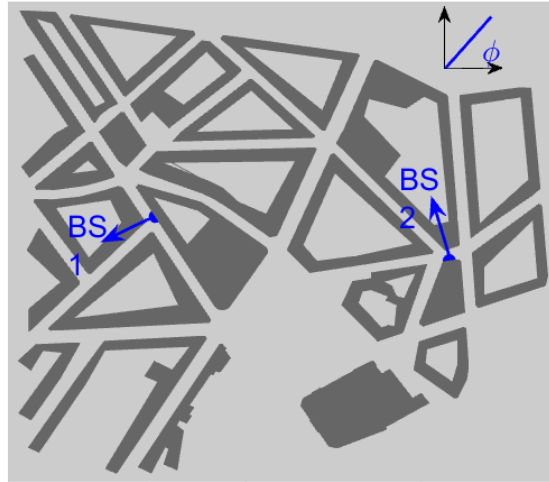
Figure 3.23: Measured reflection coefficient of BS antenna: isolated and with parasitic elements.

of the measured reflection coefficient of the base station antenna with and without the parasitic elements (three prototypes).

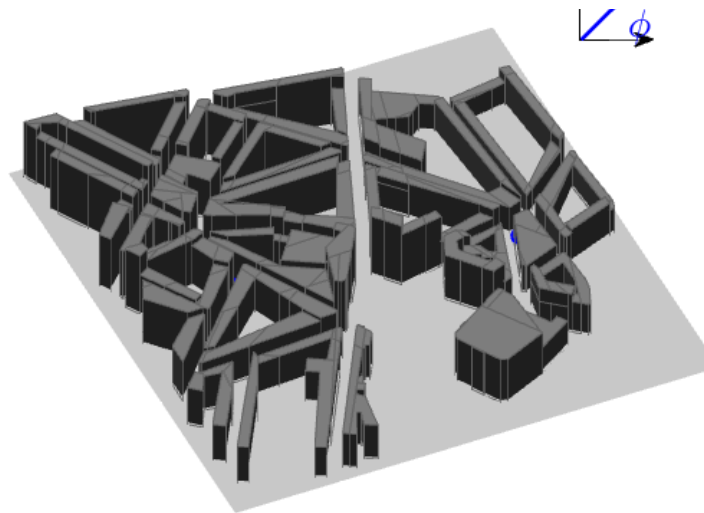
3.5 Improved Coverage Results with Optimized Base Station

In this section, we will compare the level of the electric field (in $\text{dB}\mu\text{V}/\text{m}$), in a realistic built environment, computed from in-house ray-tracing simulations using the pattern of the initial base station antenna (without parasitic elements) and the adapted patterns (with parasitic elements). The ray-tracing simulations are carried out by Quentin Gueuning. The top and side views of the simulated area, as well as the position and orientation of two base stations (BS) are shown in Fig. 3.24. The observation points lie in a horizontal plane at 2 m above the ground, considering that mobile users will put mobile terminals right next to their ears. The 3D model of the area is taken from Brussels Regional Informatics Centre (BRIC). The relative permittivity and the conductivity of the concrete walls and ground are set to $\epsilon_r = 4.44$ and $\sigma = 0.01$, respectively [59]. The expansion order N of the objective pattern (3.1) is set to 3 and the radiated power per antenna is 0.1 W. Only contributions from line-of-sight and first-order reflections are considered in the ray-tracing simulations. The field level obtained with the initial BS pattern (without parasitic elements) and with the adapted patterns (with the parasitic elements) are illustrated in Fig. 3.26 and Fig. 3.27, respectively. One can see that, across the simulated area, for the same radiated power, the field level obtained with the BS with the parasitic elements is slightly higher than that when using only the BS pattern. The reason for that improvement is that the parasitic elements have shaped and rotated the radiation patterns of the two BSs, in order to better illuminate the nearest surrounding street, as compared to the initial BS antenna pattern, as shown in Fig. 3.25.

Finally, a comparison is made in Fig. 3.28 and Fig. 3.29 between the Cumulative Distribution Functions (CDFs) of the field levels obtained with the initial pattern and the adapted radiation patterns (MoM simulations) for both BSs. Here, the CDF gives the probability to obtain less than or



(a)



(b)

Figure 3.24: Geometry of the scenario with buildings (grey) and two base stations (blue dots-arrows) (a) Top view (b) Side view.

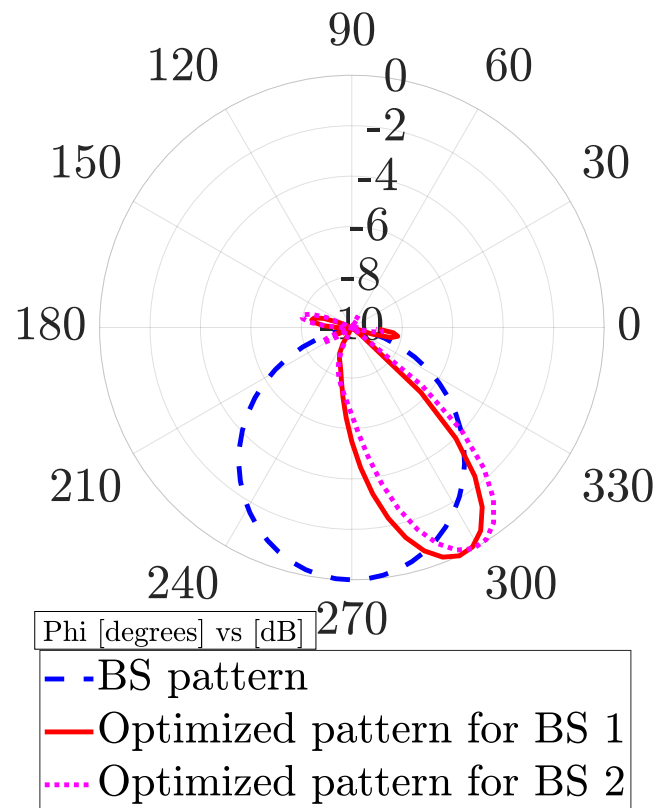


Figure 3.25: Azimuthal BS power pattern vs adapted BS power patterns (MoM) with parasitic elements, BS 1 and BS 2 are from Fig. 3.24, Frequency=1800 MHz.

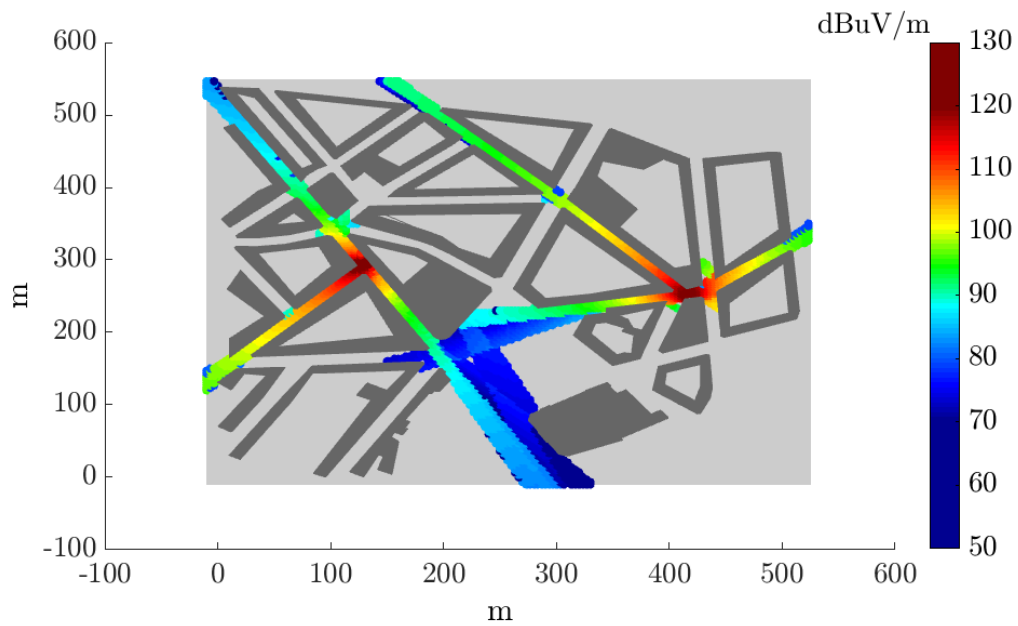


Figure 3.26: Ray-tracing simulation of the amplitude of the electric field in $\text{dB}\mu\text{V}/\text{m}$ with the BS patterns (without parasitic elements).

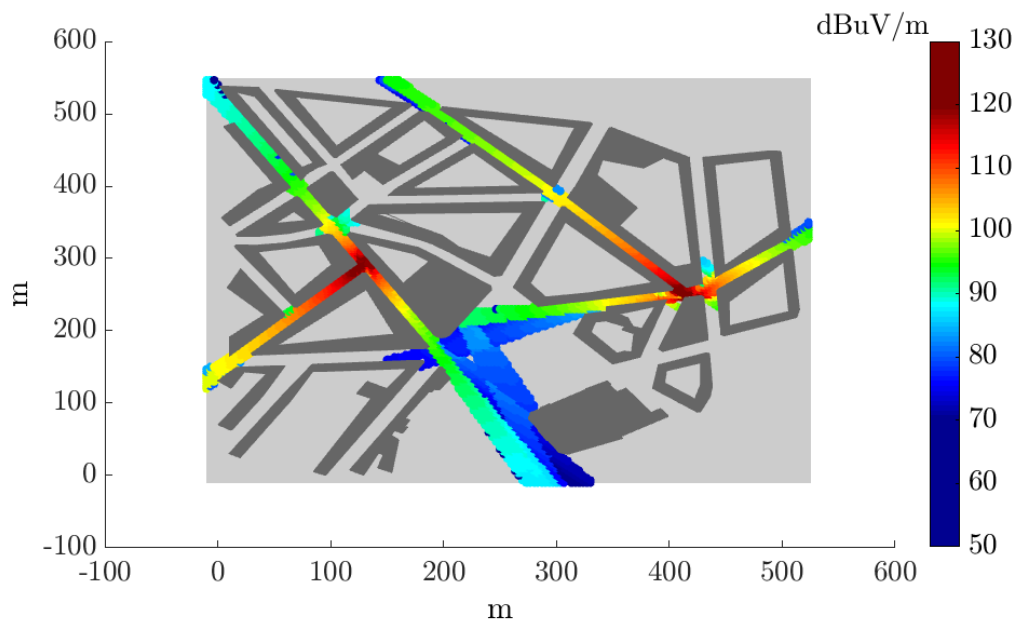


Figure 3.27: Ray-tracing simulation of the amplitude of the electric field in $\text{dB}\mu\text{V}/\text{m}$ with the adapted BS patterns with parasitic elements.

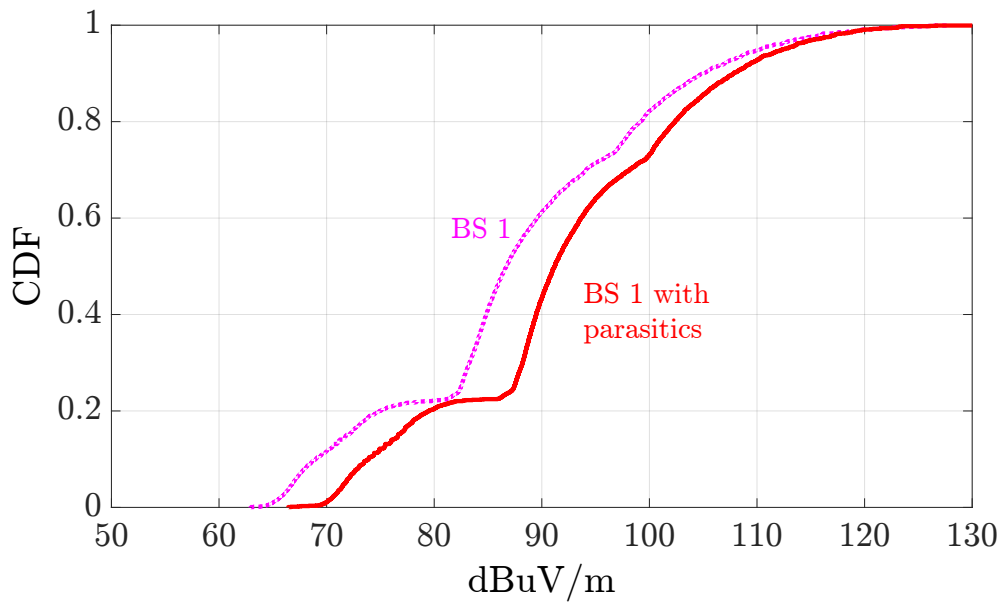


Figure 3.28: CDF of the field level from BS antenna and from BS antenna with parasitic elements for BS 1.

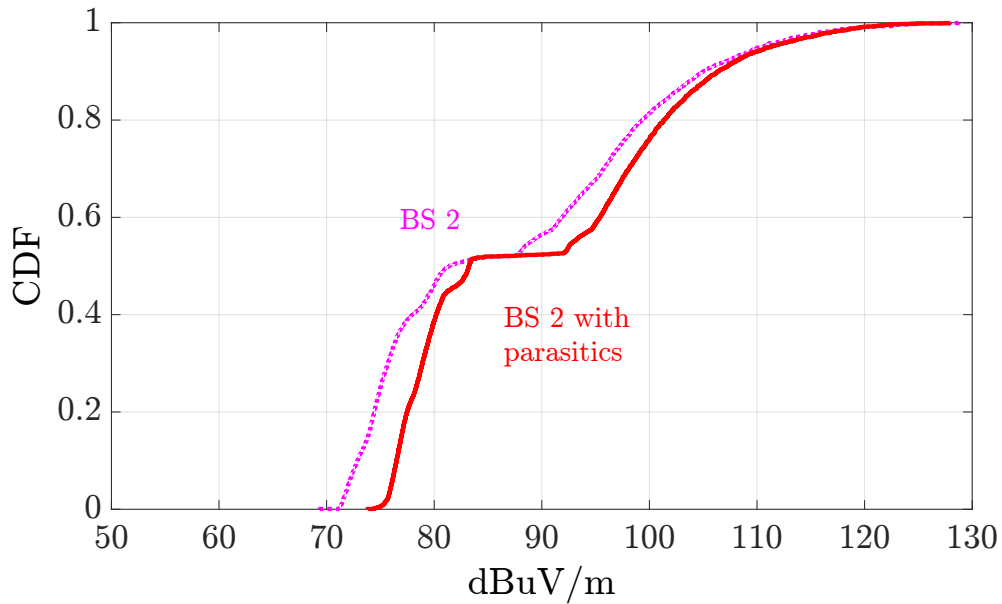


Figure 3.29: CDF of the field level from BS antenna and from BS antenna with parasitic elements for BS 2.

equal to a certain value of an electric field in an area. The comparison of CDF shows the improvement of the radio coverage since the CDFs associated to the adapted patterns are shifted to the right of the CDF of the initial BS pattern by approximately 3-4 dB. It means that for any given probability, the adapted patterns provide more electric field strength in the area.

3.6 Conclusion

A parasitic antenna array has been designed and tested in the laboratory to implement beamforming and beam-shaping for 4G and 5G communication base station antennas. It is shown that such beamforming and beamshaping can also be employed to adapt the RF power exposure level in a given area. The overall problem has been split in two parts: a propagation-oriented optimization problem which uses ray-tracing simulations to produce objective patterns that enhance the field coverage while respecting a prescribed tolerance of field levels over a given area, and a design-oriented optimization problem which finds the loads of parasitic radiators to adapt the pattern of a base station antenna such that it is as close as possible to the objective pattern. The EM model and the harmonic optimization technique utilized here can be efficiently combined for the design of parasitic antenna arrays. Ray-tracing simulations have been performed for a realistic scenario and they highlight an improvement in the coverage thanks to the adapted radiation patterns of the base station comprising of the parasitic antenna array. The simulation and experimental results for designed parasitic antenna array prototypes are also in a good agreement.

CHAPTER 4

Electronically Steerable Parasitic Array Radiator (ESPAR) Antenna

This chapter showcases the work done for the development of Electronically Steerable Parasitic Array Radiator (ESPAR) antenna. In ESPAR antenna the impedances attached to the parasitic radiators are tuned electronically to carry out beam-shaping. By tuning the impedances, mutual coupling among the elements of the ESPAR antenna varies and therefore different radiation patterns are formed. The varactor diodes [4] have been utilized to provide electronically tunable impedances.

A prototype of ESPAR antenna has been built at 1800 MHz for the BS of a cellular communication system. If ESPAR antenna with varactor diodes is to be developed for the design shown in Fig. 3.9, it would require 120 varactors. In order to simplify the verification, we have built a smaller prototype to show beam scanning capability of the ESPAR antenna.

ESPAR antennas can also be utilized for other applications which involve beamforming, for instance wireless local area network (WLAN) application

[10], internet of things (IoT) [60] and radars etc. Another prototype of ESPAR antenna printed on a layered medium has been designed at 24.5 GHz for the radar in which a high directivity is maintained while carrying out beam scanning.

Section 4.1 presents the introduction of the work that is discussed in this chapter. Section 4.2 explains the characterization of varactor diodes and their utilization in ESPAR antenna. Section 4.3 details the design and analysis of a prototype which has been developed to show beamforming for a cellular communication system. A comparison between simulation and experimental results is given as well. Finally, section 4.4 gives a description of a prototype which has been designed for the radar application. The simulation results are also given here.

4.1 Introduction

PIN diodes [9], [10], [11] and varactor diodes [8], [12] are generally used in ESPAR antennas for electronic beamforming. PIN diodes provide ON (short circuit) or OFF (open circuit) states, while varactor diodes provide tunable capacitive reactances. Therefore, the use of varactor diodes provides more degree of freedoms to shape the beam but it entails biasing and control challenges as well. In order to obtain also an inductive impedance, a fixed inductor is placed in series with the varactor diode. A varactor diode and a designed tunable impedance circuit are characterized at 1800 MHz to obtain a profile of tunable impedances versus biasing voltage.

A small prototype of an ESPAR has been designed for a cellular communication to improve a coverage. For a driven antenna, an antenna similar to the BS antenna [3] but with only one element is designed. The parasitic dipoles with varactors are used in front of it to carry out the beam-shaping.

ESPAR antennas consisting of patch antennas have been proposed in [28] and [10], they consist of a driven patch antenna on a bottom layer and multiple parasitic patches on a top layer. The parasitic patches are interconnected with each other through RF switches. Such antennas with electrically small (less than $\lambda/10$) parasitic patches are referred to as parasitic pixel antenna [28], [9]. The use of bigger pixels does not provide enough

beam scanning capability in all planes [61]. In pixel antennas, the distance between driven and parasitic layers can be adjusted to provide a trade-off between frequency and radiation pattern reconfigurability. Small distance (less than $\lambda/20$) provides more tunable frequency range and vice versa [9]. In this thesis, I have utilized a parasitic layer but it is not a pixel layer which means the parasitic patches are not electrically small. Moreover, the parasitic patches are connected with each other through tunable impedances (loads). It is difficult to design a high gain printed ESPAR antenna with a beam steering capability while keeping the driven antenna matched and side lobes suppressed. The design challenges include the optimization of parasitic loads and biasing of tunable impedances. In the literature [28], [10], most researchers have used commercial EM solvers to optimize the parasitic loads. It involves full-wave simulation at each iteration of the optimization which makes this approach very time consuming. I have used an efficient methodology to design a printed ESPAR antenna, it involves computing all the open-circuit patterns by using in-house developed MoM code for a layered medium. This methodology has been well explained in Section 2.2.

In a printed ESPAR antenna proposed in [10], a maximum gain of 6.5 dB has been achieved with the side lobe level (SLL) of -3 dB, while carrying out beam scanning at discrete angles ($+30^\circ, 0^\circ, -30^\circ$). A pixel antenna presented in [28] can provide a gain of 8 dB and beam scanning at discrete angles ($+30^\circ, 0^\circ, -30^\circ$) with the side lobe level (SLL) of -7 dB. In [10], [28], RF switches are utilized to interconnect the parasitic patches. A varactor diode has been used for a beam-steering in [12], but it is used to connect the driven patch with the parasitic patches, located on the same layer. The antenna design proposed in [12] provides a maximum gain of 7.5 dB with a scanning range of $\pm 15^\circ$. Higher directivity, in the order of 20 dB, can be achieved by highly-reflective frequency selective surface (FSS) with a patch antenna [62], without scanning the beam. In this thesis, an ESPAR antenna based on an FPC has been designed for a radar application, it can provide a high gain of 13 dB while carrying out beam-scanning in the range of $\pm 9^\circ$ with the side lobe level (SLL) of -9 dB. The use of tunable impedance circuit provides more degrees of freedom to scan the beam at different angles without significant loss in directivity. It also provides a continuous beam

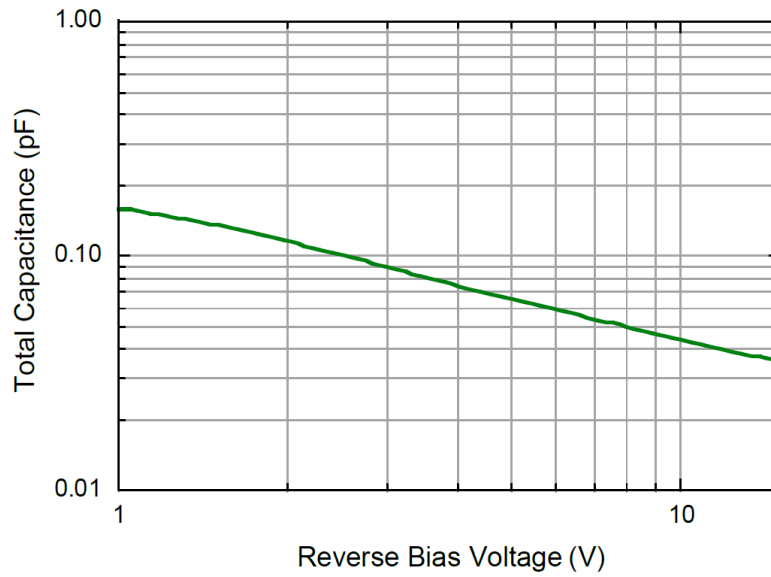


Figure 4.1: Varactor capacitance vs biasing voltage [4].

scanning angle within a certain range, rather than at discrete angles, as was the case for [10] and [28]. Besides, a method has been proposed to bias the varactor diodes in such a way that the biasing lines do not cause unwanted scattering.

4.2 Varactor Diodes

In order to steer the beam electronically in a parasitic antenna array, an impedance is needed that can be varied electronically. Therefore, a varactor diode is used here in reverse biased condition; its capacitance varies by changing the DC bias voltage.

4.2.1 Characterization of Varactor diodes and tunable impedance circuit

The MAVR-011020-1411 diode [4] is used because of its suitable range of capacitance ($0.19 \text{ pF} - 0.025 \text{ pF}$). Its data sheet gives the range of capacitance with respect to variable DC bias at 1 MHz as shown in Fig. 4.1. For our application it needs to be characterized at 1800 MHz to find out the exact impedance provided by it at the terminals of the parasitic elements.

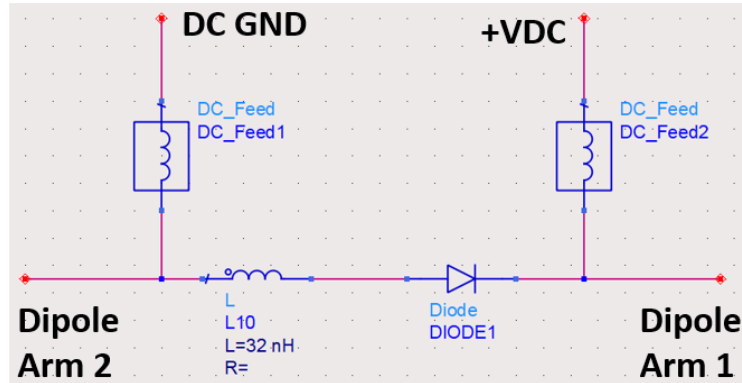


Figure 4.2: Tunable variable impedance circuit.

Since a varactor diode gives only a variable capacitive impedance, a fixed inductor is placed in series with the varactor diode in order to cover both positive and negative reactances. Large inductors are placed in series with DC feed to block the RF currents flowing on the DC bias lines, in order to minimize the scattering from the DC bias lines. Although the DC bias lines are made very thin and RF chokes are used to minimize the scattering, they are still included in the EM simulation and the load optimization procedure, to take into account the residual scattering. The schematic of tunable impedance circuit which provides both capacitive and inductive impedances is shown in Fig. 4.2. The capacitive reactance range provided by a varactor diode at 1800 MHz is estimated from ADS [40] simulations. An inductor of 32 nH is used in series with the varactor diode such that the circuit can provide a suitable range of capacitive and inductive reactances.

4.2.2 Characterization using microstrip test fixture

For the characterization of the varactor diode and tunable impedance circuit, a transmission line theory formulation has been utilized. A circuit has been fabricated which consists of a 50Ω microstrip transmission line connected to the one end of Device Under Test (varactor diode or tunable impedance circuit). The other end of DUT is grounded through a via. The circuits have been fabricated on I-Tera substrate ($\epsilon_r = 3.38$ and $\tan \delta = 0.0028$ at 2 GHz) [58] because the same substrate has been used later on for the fabrication of parasitic dipoles which will have tunable impedance

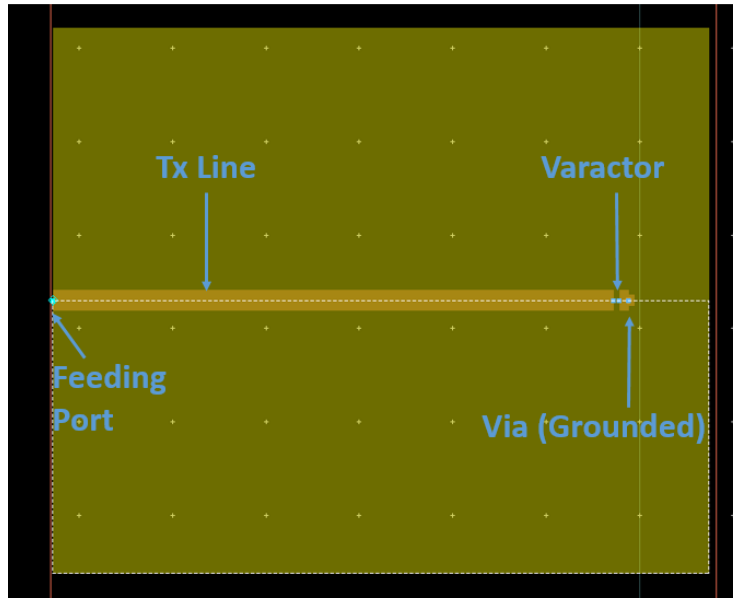


Figure 4.3: $50\ \Omega$ microstrip transmission line feeding to the varactor.

circuits on their terminals. The layout of the characterization circuit for the varactor diode, as well as the tunable impedance circuit are shown in Fig. 4.3 and Fig. 4.4, respectively. The equivalent transmission-line model is shown in Fig. 4.5.

By connecting the Vector Network Analyzer (VNA) at a microstrip feeding port shown in Fig. 4.3 and Fig. 4.4, Γ_{in} is measured. Then Γ_L is computed from Γ_{in} using (4.1). This relation is a general expression and includes the effect of mismatch and losses of $50\ \Omega$ feeding transmission line. The two port S-parameters of the feeding transmission line are measured separately which characterizes the transmission line completely.

$$\Gamma_L = \frac{S_{11} - \Gamma_{in}}{-\Gamma_{in}S_{22} + S_{11}S_{22} - S_{12}S_{21}} \quad (4.1)$$

Then Z_L is computed from Γ_L using (4.2).

$$Z_L = Z_o \frac{1 + \Gamma_L}{1 - \Gamma_L} \quad (4.2)$$

The computed Z_L is the impedance of the DUT (varactor diode or tunable impedance circuit). But this impedance includes the effect of fringe capaci-

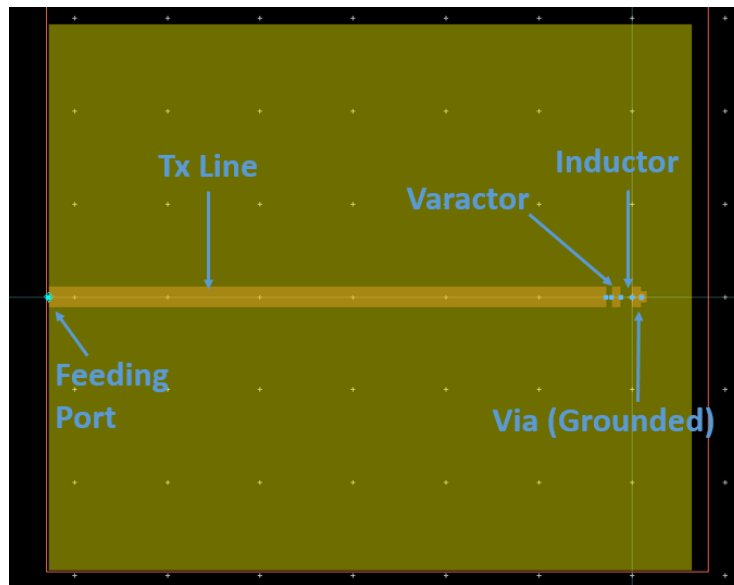


Figure 4.4: $50\ \Omega$ microstrip transmission line feeding to the tunable impedance circuit.

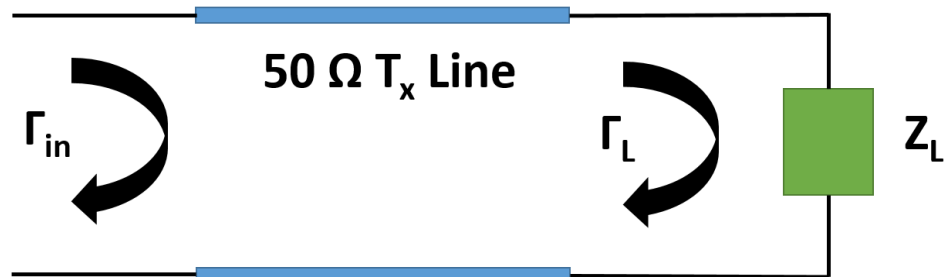


Figure 4.5: Equivalent transmission-line model of the microstrip circuit used for the characterization of varactor diode and tunable impedance circuit.

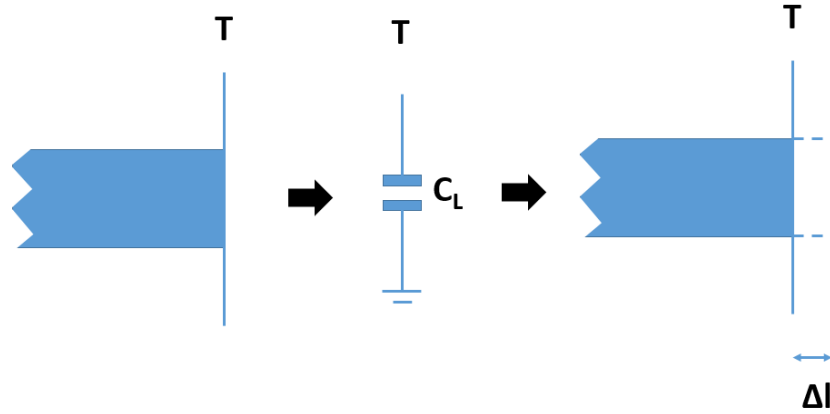


Figure 4.6: Fringe capacitance at the open end of transmission line.

tance at the end of transmission line where the DUT is connected as shown in Fig. 4.6. Physically this effect is because the fields do not stop abruptly at the open end of transmission line instead they extend slightly further due to the effect of the fringing field. This fringe capacitance can be represented as extended transmission line of length Δl , given by the relation (4.3).

$$C_L = \frac{\Delta l \sqrt{\epsilon_{r,eff}}}{cZ_o} \quad (4.3)$$

In order to estimate Δl , the accurate formulations provided by [63] are used, which are given from (4.4) to (4.9). The fringe capacitance computed from these formulations is $0.00726pF$. The impact of the fringe capacitance is removed from the measurements to compute the impedance Z_L of the DUT.

$$\frac{\Delta l}{h} = \frac{ACE}{D} \quad (4.4)$$

$$A = 0.434907 \frac{(\epsilon_{r,eff}^{0.81} + 0.26)((W/h)^{0.8544} + 0.236)}{(\epsilon_{r,eff}^{0.81} + 0.189)((W/h)^{0.8544} + 0.87)} \quad (4.5)$$

$$B = 1 + \frac{(W/h)^{0.371}}{2.358\epsilon_r + 1} \quad (4.6)$$

$$C = 1 + \frac{0.5274 \arctan [0.084(W/h)^{1.9413/B}]}{\epsilon_{r,eff}^{0.9236}} \quad (4.7)$$

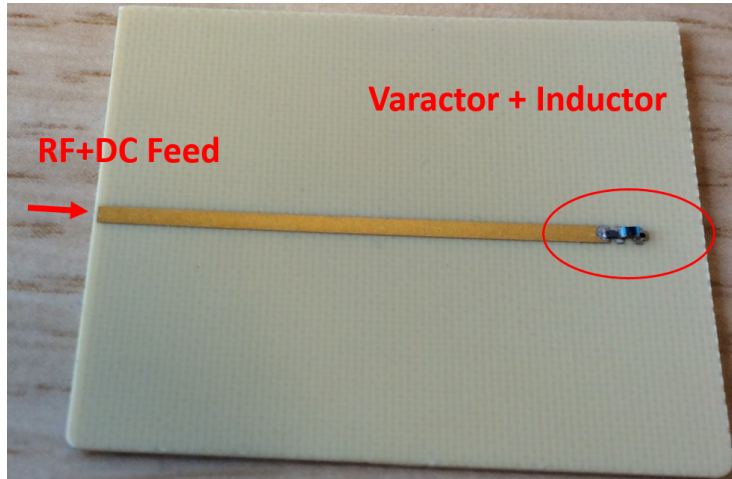


Figure 4.7: PCB of tunable impedance circuit used for characterization.

$$D = 1 + 0.0377 \arctan [0.067(W/h)^{1.456}] \times [6 - 5 \exp(0.036(1 - \epsilon_r))] \quad (4.8)$$

$$E = 1 - 0.218 \exp(-7.5W/h) \quad (4.9)$$

The other important factors which are present in the measurements and need to be de-embedded include the effects of SMA connector and transition from coax cable (coming from the VNA) to microstrip PCB. These factors can add extra line length, as well as parasitic components which are not included in our transmission line model shown in Fig. 4.5. In order to circumvent this problem, a microstrip test fixture has been used in which classical calibration is carried out at the end of the SMA connector's pin. The SMA connectors are not soldered to the PCB in fact, they come with the test fixture such that connector's pin clamps onto the PCB. A microstrip calibration kit has been used to shift the reference plane to the beginning of microstrip transmission line.

The PCBs of varactor diode and tunable impedance circuit are fabricated for the characterization as shown in Fig. 4.7. The experimental set-up for the characterization of tunable impedance circuit is shown in Fig. 4.8. The DC bias of the varactor diode and tunable impedance circuit is given through the VNA along with the RF signal. After moving the measurement reference plane to the beginning of the microstrip transmission line, Γ_{in} is measured by the VNA. Then Γ_L is computed using (4.1) and Z_L is computed

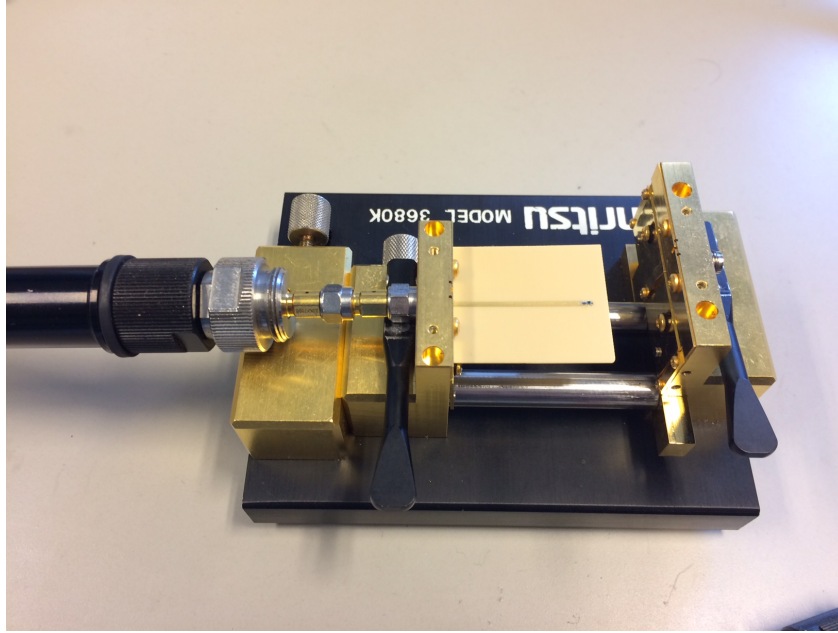


Figure 4.8: Measurement set-up using microstrip test fixture.

using (4.2). After that, the fringe capacitance of $0.00726pF$, computed from relations (4.3) to (4.9), is removed from Z_L to compute the impedance of the DUT i.e. varactor diode or tunable impedance circuit. For different DC bias voltages the same procedure is repeated to measure the impedance of the DUT. The variation of impedance of the varactor diode and tunable impedance circuit with the DC bias are given in Fig. 4.9 and Fig. 4.10, respectively. Fig. 4.9 shows the variation of capacitive impedance of the diode versus DC bias voltage. It can be seen from Fig. 4.10 that by changing the DC bias both capacitive and inductive impedances can be realized with the designed tunable impedance circuit. It provides a suitable range of variable capacitive and inductive impedance, as required for the ESPAR antenna to implement beamforming.

4.3 ESPAR Antenna for Cellular Communication

An ESPAR antenna prototype has been designed to implement beamforming for a cellular communication system. This prototype consists of a driven antenna and 4 parasitic dipole radiators with a tunable impedance circuit to implement beamforming.

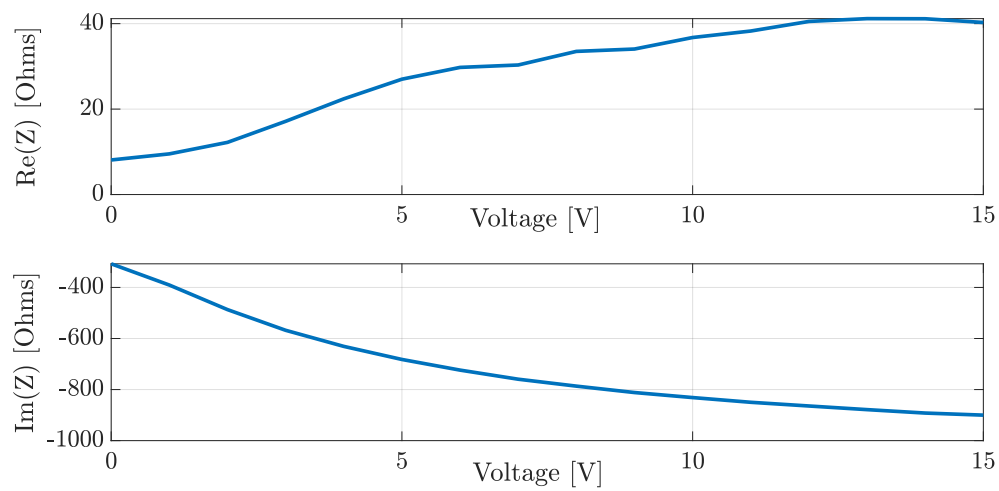


Figure 4.9: Measured impedance of varactor at 1800 MHz.

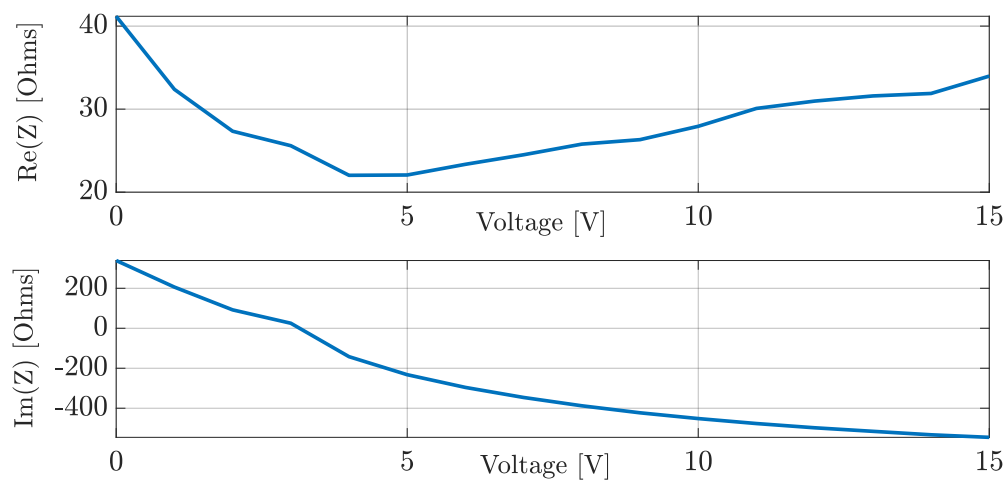


Figure 4.10: Measured impedance of tunable impedance circuit at 1800 MHz.

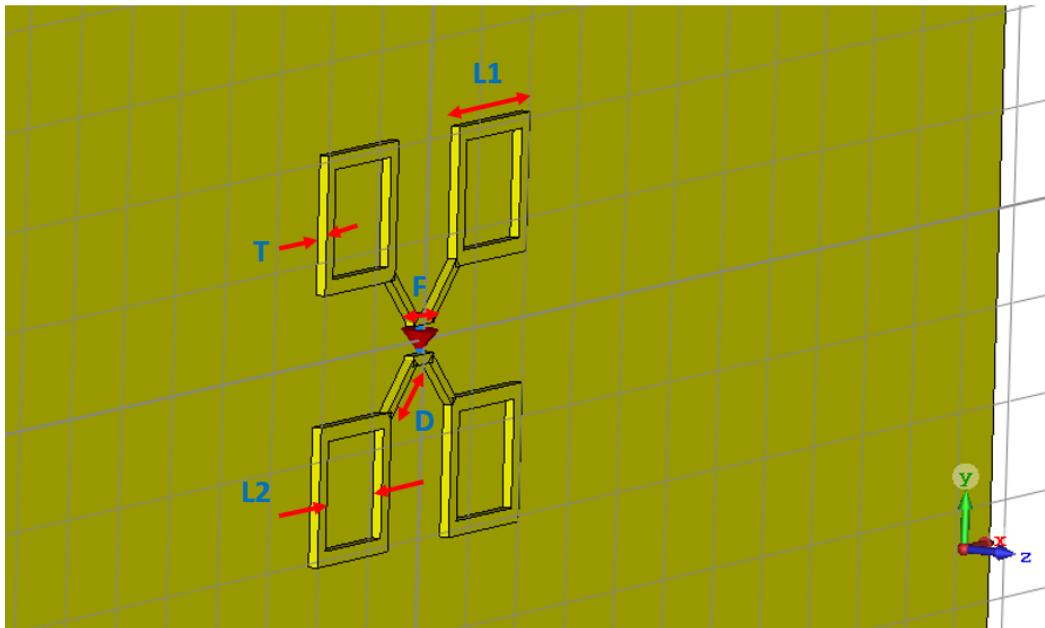


Figure 4.11: Driven antenna of ESPAR with a delta-gap feed (front view).

4.3.1 Driven antenna

First, a driven antenna has been designed similar to the single element of a BS antenna [3]. It is a cross dipole antenna with a back reflector. The antenna is fed with a SMA connector through a coax feed coming through a back reflector. Since the coax feed is single-ended and the antenna has a differential feed, a balun has been designed to feed the antenna properly.

The driven antenna designed at 1800 MHz with delta feed is shown in Fig. 4.11. There is gap of quarter wavelength $\lambda/4$ between the cross dipole and back reflector. The antenna dimensions are $L1 = 1.4$ cm, $L2 = 1.1$ cm, $T = 0.1$ cm, $F = 0.4$ cm, $D = 0.579$ cm.

The antenna has been designed using the CST software, the reflection coefficient (S_{11}) of antenna with a delta-gap feed is shown in Fig. 4.12. The antenna matching could have been improved but we intended to keep the antenna dimensions same as those of the BS antenna [3]. In order to feed the driven antenna practically with a coax cable [64], a balun has been designed. A balun forces an unbalanced transmission line to feed a balanced component. A folded balun, sometimes referred to as a quarter wavelength balun has been used. It consists of a quarter wavelength connection between

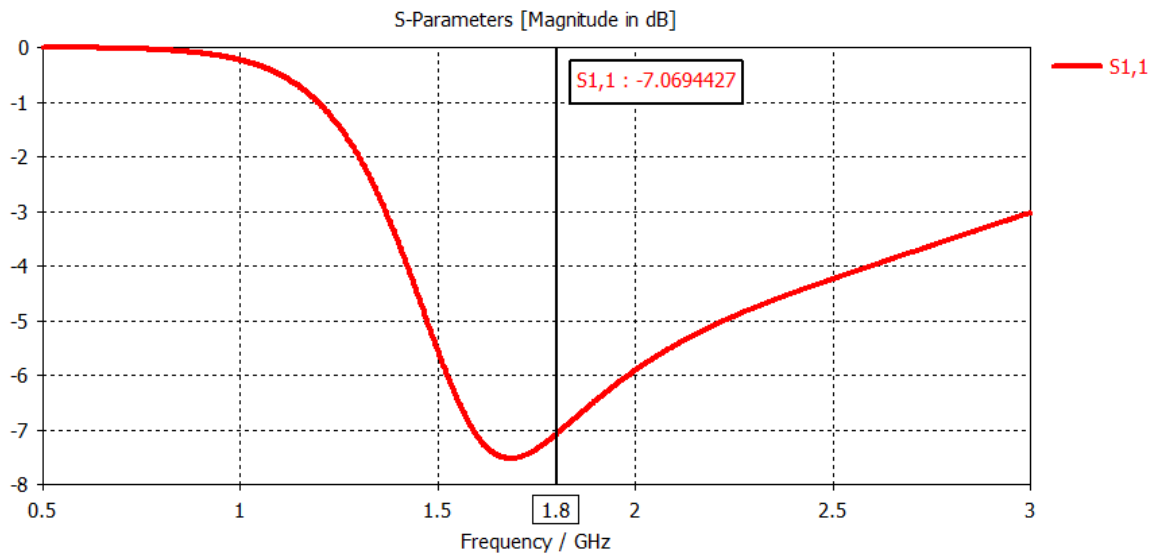


Figure 4.12: Reflection coefficient of the driven antenna with a delta-gap feed (CST simulation).

one of the feeding points of the antenna and the feeding coax cable, as shown in Fig. 4.13, it forces balanced currents on the coax cable.

It is found out with CST simulations that using the designed balun and coax cable the antenna impedance changes, which is not an ideal thing. The modified reflection coefficient of the designed driven antenna is shown in Fig. 4.14. The resonance has been clearly shifted towards lower frequencies. This shift in the resonance can be explained by the non-ideal balun. Since we are interested in adapting the radiation pattern of the antenna, we proceeded on with this non-perfect feeding. The driven antenna is fabricated and measured in an anechoic chamber. The simulated and measured radiation pattern of the driven antenna are shown in Fig. 4.15.

4.3.2 ESPAR antenna

A prototype, consisting of four printed parasitic dipoles is designed with the characterized variable impedance circuit placed at the terminals of the dipoles. The half-wavelength (8.3 cm) parasitic dipoles of width $\lambda/40$ (0.4 cm) are printed on the I-Tera substrate [58] with DC bias lines of 0.1 mm thickness, which are used to tune the impedance of the circuit as shown in Fig. 4.16. The parasitic elements are placed at half-wavelength

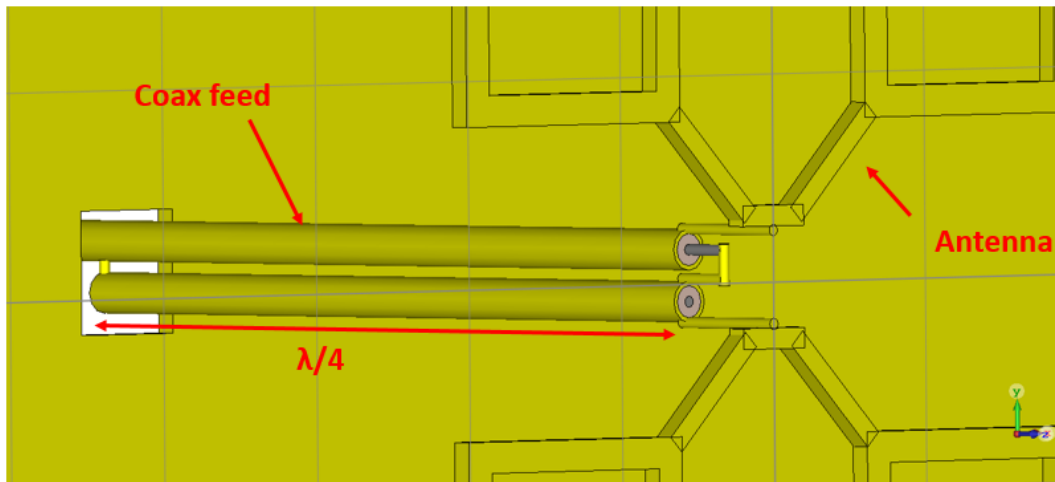


Figure 4.13: The balun feed from coax cable to the cross dipole antenna.

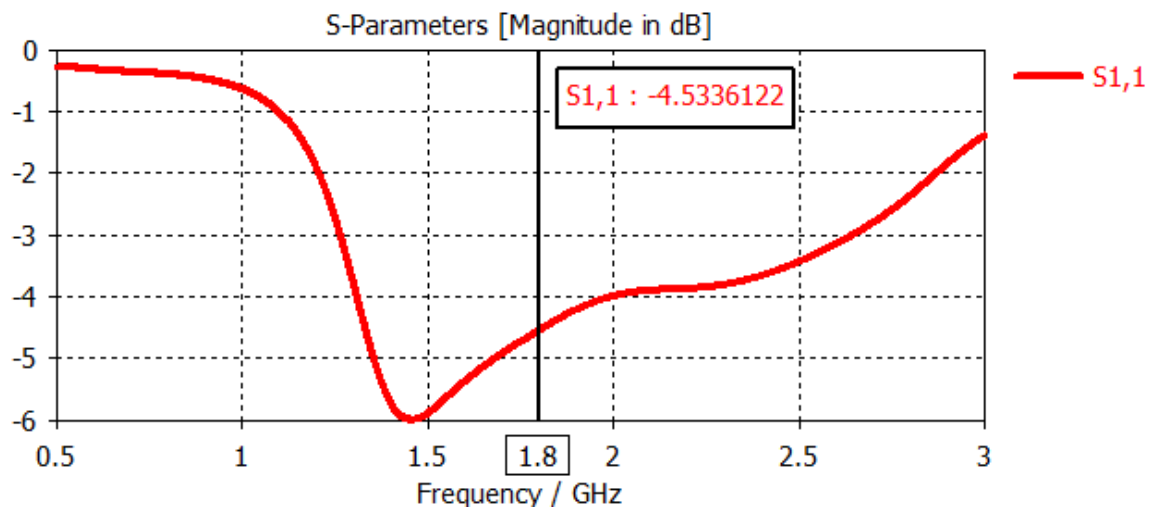


Figure 4.14: Reflection coefficient of the driven antenna with balun and coax feed (CST simulation).

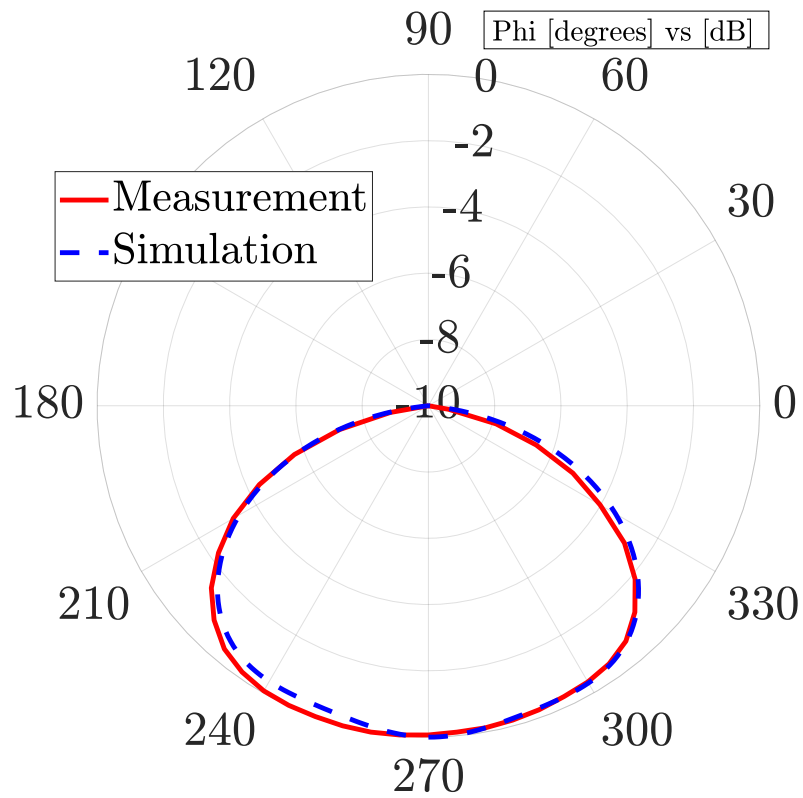


Figure 4.15: Azimuthal power pattern of the driven antenna, Frequency=1800 MHz (CST simulation vs measurement).

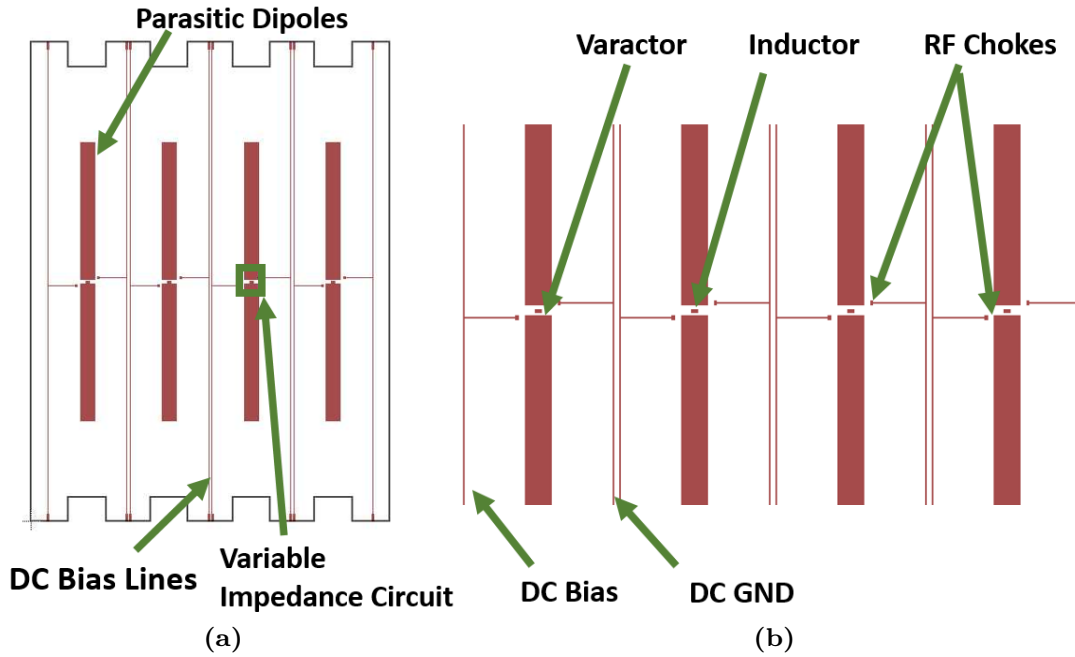


Figure 4.16: (a) Parasitic radiators with a biasing circuitry (b) zoom version.

distance from the driven antenna. The design of ESPAR antenna can be seen in Figs. 4.17 and 4.18.

Table 4.1: Parasitic reactances and DC biases for radiation pattern of ESPAR antenna prototype, Case I shown in Fig. 4.21.

Case I	
Parasitic Reactance (Ω)	DC Bias (V)
62i	2.5
-292i	6
51i	2.6
-282i	5.9

The parasitic loads are computed to obtain the desired patterns, they are given in Table 4.1 and Table 4.2. The EM model detailed in Section 2.2 along with harmonic optimization explained in Section 2.5.1 have been used to compute these loads. The ohmic part of the series impedance of the tunable impedance circuit incur losses, shown in Fig. 4.10. By including the losses, the maximum gain and efficiency computed from simulation are

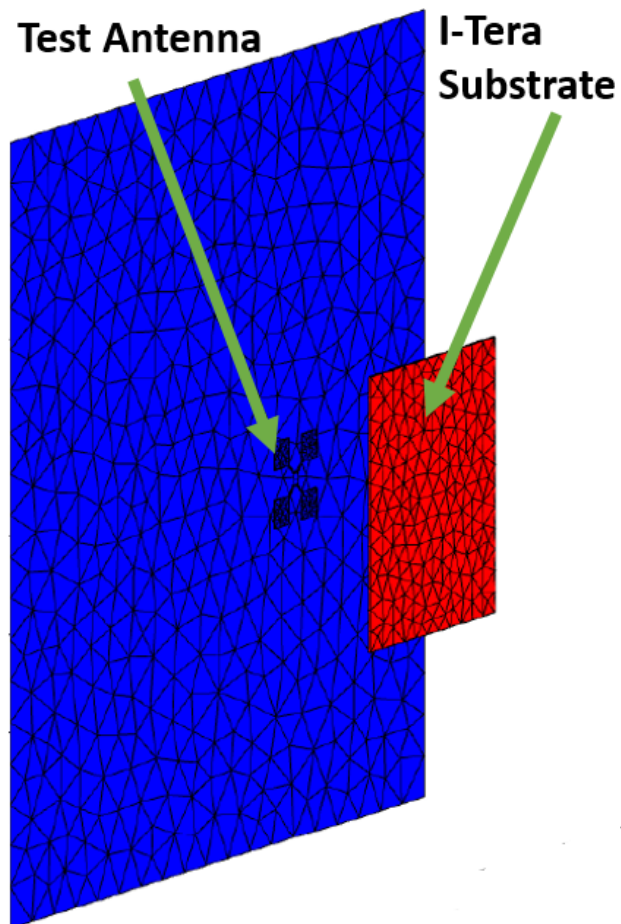


Figure 4.17: ESPAR antenna (Front view).

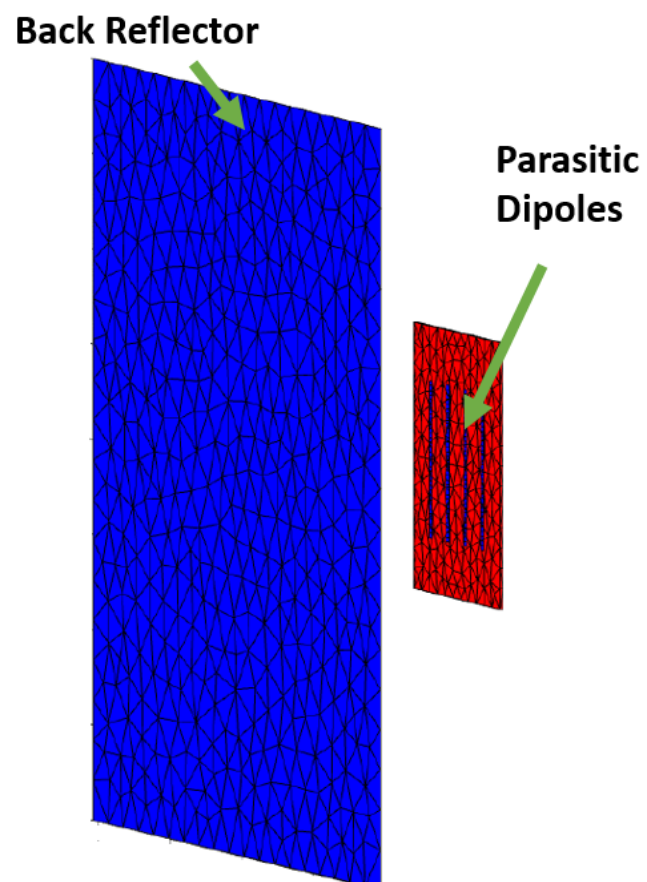


Figure 4.18: ESPAR antenna (Interior view).

Table 4.2: Parasitic reactances and DC biases for radiation pattern of ESPAR antenna prototype, Case II shown in Fig. 4.22.

Case II	
Parasitic Reactance (Ω)	DC Bias (V)
-253i	5.6
-536i	14
-315i	6.4
137i	1.6

Table 4.3: Maximum gain and efficiency of the test antenna with and without the parasitic elements, MoM simulation at 1800 MHz.

	Maximum Gain [dB]	Efficiency [%]
Test antenna	5.55	95
Test antenna Case-I	8.95	72
Test antenna Case-II	9.27	73

given in Table 4.3. The maximum antenna gain reduces with an increase in the ohmic losses of a tunable impedance circuit. The fabricated prototype is shown in Fig. 4.19.

The fabricated prototype is tested in an anechoic chamber to verify its beam scanning capabilities. The block diagram of the experimental set up is shown in Fig. 4.20. The variable impedances are tuned using a control signal from Digital-to-Analog Converter (DAC) programmed by a computer. The DAC produces the different DC bias voltages for each varactor to have the impedances given in Table 4.1 and Table 4.2. The two different radiation patterns of the Case I and Case II can be formed by just tuning the control signal from the computer.

Table 4.4: Maximum gain of the test antenna with and without the parasitic elements, measured at 1800 MHz.

	Maximum Gain [dB]
Test antenna	5.19
Test antenna Case-I	7.11
Test antenna Case-II	7.78

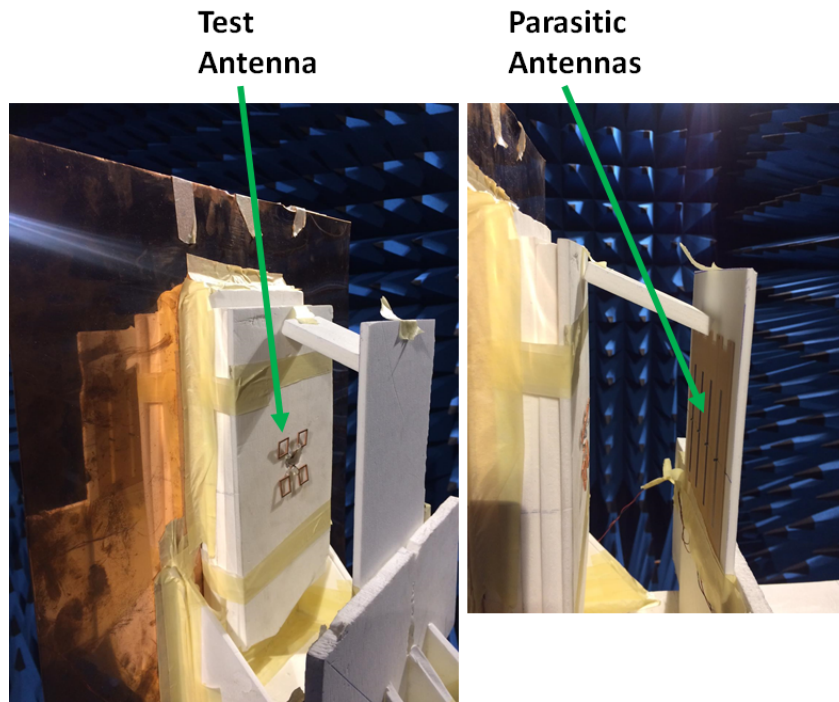


Figure 4.19: Fabricated ESPAR antenna.

The comparison between objective radiation patterns, simulated patterns (with and without varactor ohmic losses) and measured patterns for Case I and Case II are shown in Fig. 4.21 and Fig. 4.22, respectively. The two straight dotted lines in each plot delineate the widest angle $\pm\alpha$ at which the parasitic elements are placed from broadside. The antenna is oriented towards an angle of 270° , by just changing the DC bias voltages the main beam can be steered in either directions. The relative errors (3.11) between the objective and obtained patterns (simulations with varactor ohmic losses) are -4.82 dB and -4.85 dB for Case I and Case II, respectively. The obtained radiation patterns in simulations have higher side lobes as compared to the prototype with fixed loads described in Section 3.4. The reason is that fewer parasitic radiators are used to adapt the radiation pattern and hence they do not truly surround the driven antenna. This limited number of controllable loads prevented scanning of the beam at wider angles while maintain low SLLs. The results shown in Fig. 4.21 and Fig. 4.22 depict a good agreement between the simulation (with varactor ohmic losses) and experimental results, except for slightly higher SLLs in the measured patterns as compared

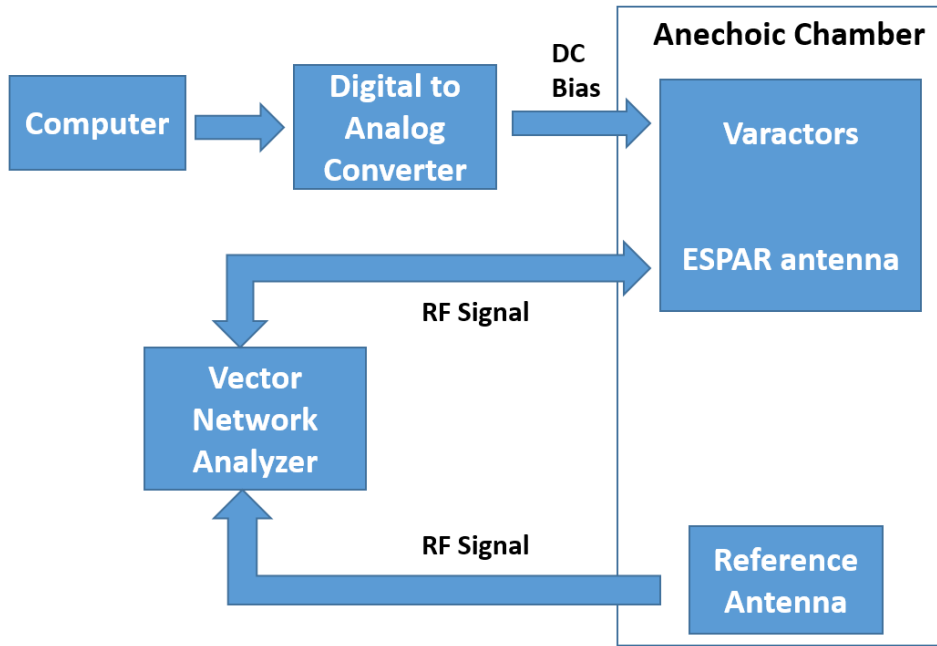


Figure 4.20: Experimental set up of the ESPAR antenna.

to the simulation (with varactor ohmic losses) results. The relative errors between the objective and obtained patterns (measurements) are -2.82 dB and -4.42 dB for Case I and Case II, respectively. The measured maximum gains of the ESPAR antenna are given in Table 4.4. The measured maximum gains are less than those of the simulations, already given in Table 4.3. However, there is a margin of error in the measured gain because of the inaccuracies in the link budget parameters. The small discrepancy in the measured patterns can be attributed to inaccuracies in the alignment of the parasitic elements with respect to the driven element. A comparison is made between the measured reflection coefficients of the only driven antenna (test antenna), ESPAR antenna Case I and ESPAR antenna Case II, it is displayed in Fig. 4.23. It shows that the matching of the driven antenna does not deteriorate significantly with the use of parasitic dipoles and loads for Case I and Case II.

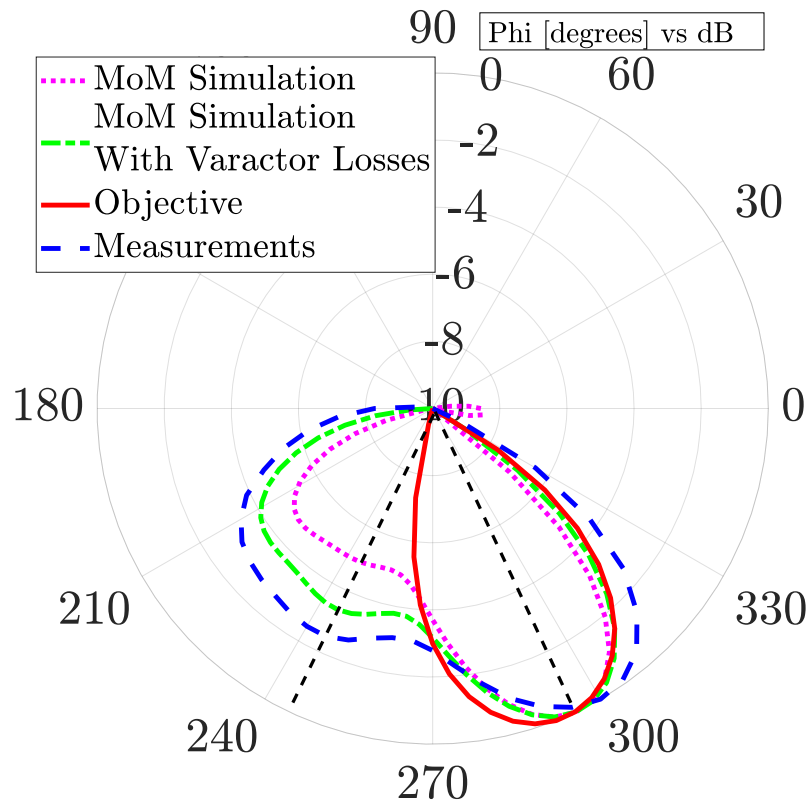


Figure 4.21: Comparison of azimuthal objective power pattern, obtained simulated (MoM) and measured power patterns from the ESPAR antenna, Case I, Frequency=1800 MHz.

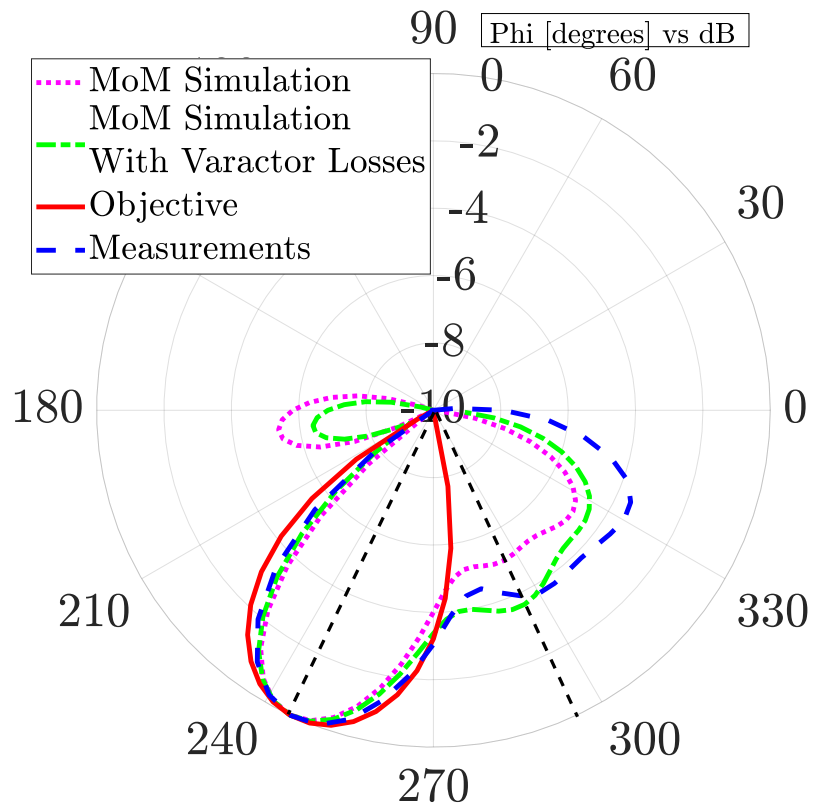


Figure 4.22: Comparison of azimuthal objective power pattern, obtained simulated (MoM) and measured power pattern from the ESAPR antenna, Case II, Frequency=1800 MHz.

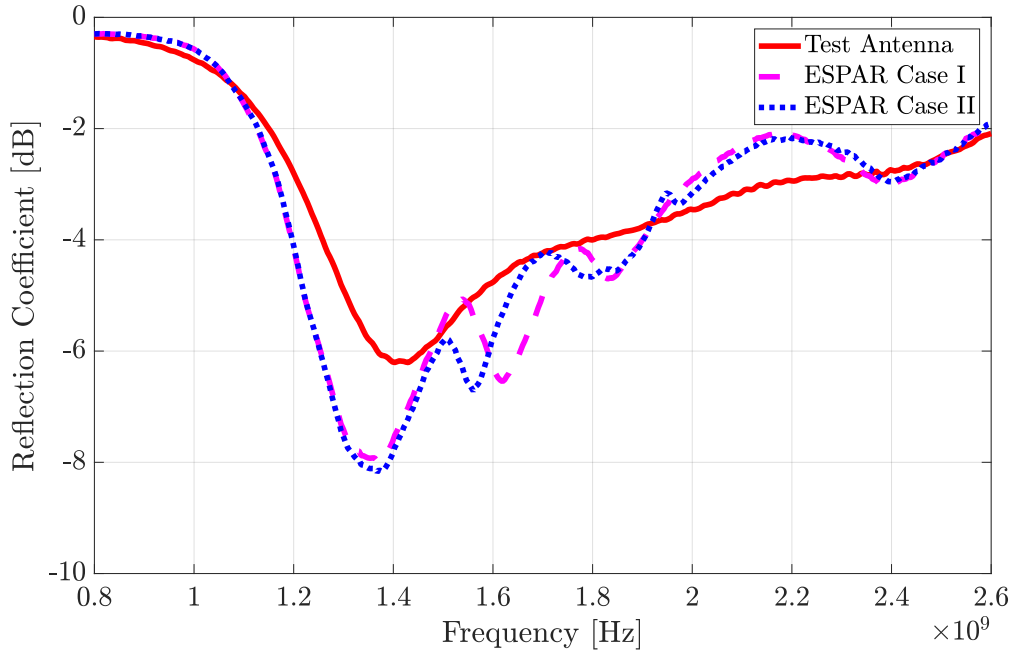


Figure 4.23: Measured reflection coefficient of Test Antenna, ESPAR antenna Case I and ESPAR antenna Case II.

4.4 ESPAR Antenna for a Radar

An ESPAR antenna printed on a layered medium has been designed for the radar at 24.5 GHz. In [10], [12], [28] commercial full-wave solvers have been utilized for the analysis and design of a ESPAR antenna on layered media. In this thesis, an efficient Method-of-Moments (MoM) code for layered media [65], [66], developed in the lab, has been utilized. The Green's function is the spatial impulse response of a given medium i.e. fields radiated by a point current source with a given polarization. In a layered medium, it is not straightforward to compute the Green's function of a point source in a spatial domain. However, the propagation of plane waves in a layered medium is a simpler problem and well known through a transmission line theory. The point source can be expressed as a spectrum of current sheets. Therefore, it becomes easier to compute the Green's function in the spectral domain. After computing the Green's function in a spectral domain, it is converted back to spatial domain in order to convolve with basis and testing functions in the method of moments. So, using the method of moments, the

currents are determined at a source layer which leads to the computation of electric fields at the same layer. By using the transmission line theory, the electric fields are computed at each layer of a multi-layered medium. Once the electric fields are known at the top or bottom layer, the radiated fields are computed. All the formulation has been detailed in the Appendix A.

4.4.1 Design of an ESPAR antenna

The ESPAR antenna considered here comprises three substrate layers and is shown in Fig. 4.24 and Fig. 4.25. The bottom layer of RO4350B ($\epsilon_r = 3.66$ from 8 to 40 GHz) contains the microstrip driven patch antenna and the top most layer, also made of RO4350B ($\epsilon_r = 3.66$ from 8 to 40 GHz), contains parasitic patches connected with each other via tunable reactive impedances. A substrate RO4350B of thickness 0.254 mm is considered here. A layer of Rohacell ($\epsilon_r = 1.04$ at 26.5 GHz) is used as a spacer of 6 mm thickness between the active layer and the parasitic layer. A driven patch antenna of dimension 2.95 mm \times 4.03 mm is designed to operate at 24.5 GHz as shown in Fig. 4.26. The square parasitic patches of size 3.3 mm \times 3.3 mm are placed on the top layer. The number of parasitic patches and spacing between them are optimized to obtain a maximum directivity. It has been noticed, after initial optimization, that 5 \times 5 parasitic patches with a spacing of 4 mm among them provide the maximum directivity. The configuration of parasitic patches is shown in Fig. 4.27.

The maximum directivity of the active patch antenna taken in isolation (i.e. without parasitic layer) was 6.75 dBi, which has been increased with the superstrate and the parasitic patches. After that, parasitic patches are connected with each other vertically via a tunable impedance circuit, as shown in Fig. 4.27. It leads to a total number of 5 \times 4 = 20 tunable parasitic impedances in the array. By tuning the parasitic impedances the directivity can be further enhanced and beam scanning can be carried out as well. In this work, we are interested to implement beam-scanning only along different elevation angles θ , while the azimuthal angle is set to $\phi = 0$ (H-plane), as shown in Fig. 4.24. Therefore, reactive elements are considered to be identical in one column, it results into total 5 independent tunable impedances.

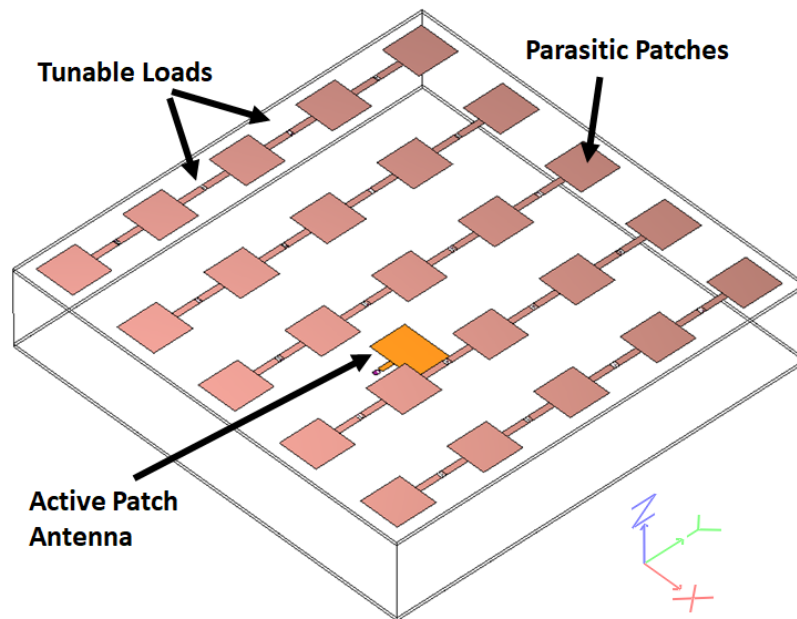


Figure 4.24: 3D figure of the printed ESPAR antenna designed at 24.125 GHz.

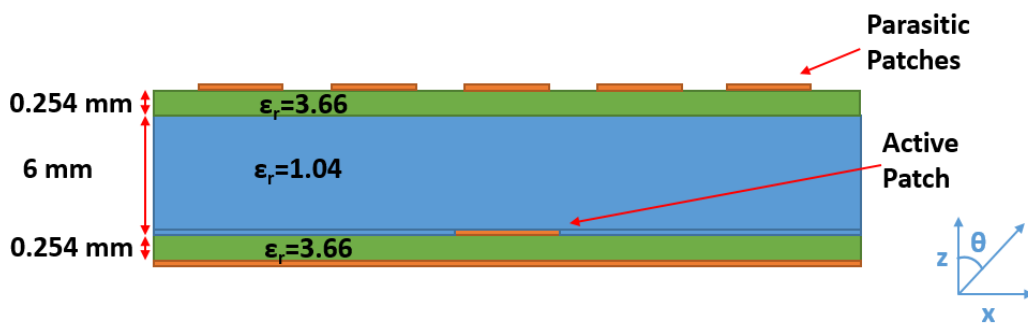


Figure 4.25: Cross section of the printed ESPAR antenna.

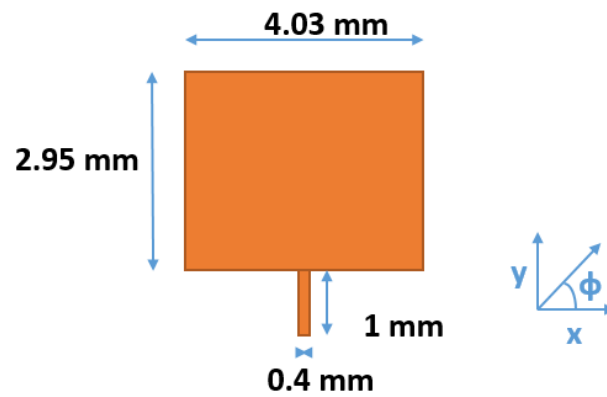


Figure 4.26: Active layer of the printed ESPAR antenna.

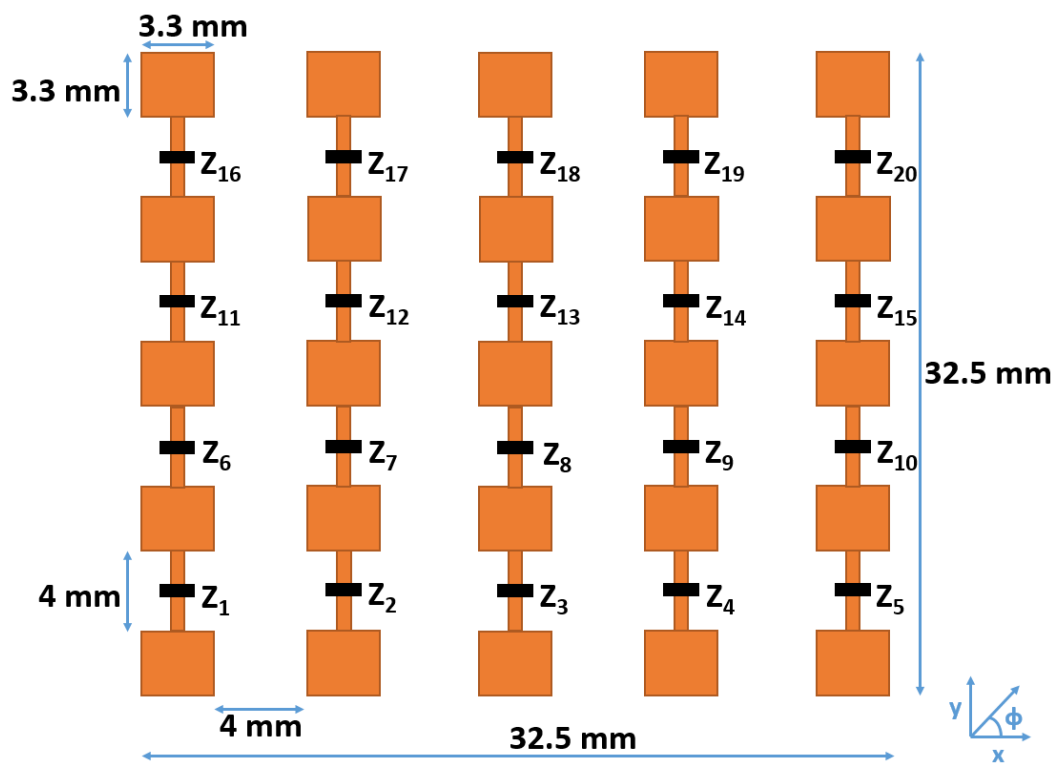


Figure 4.27: Parasitic layer of the printed ESPAR antenna.

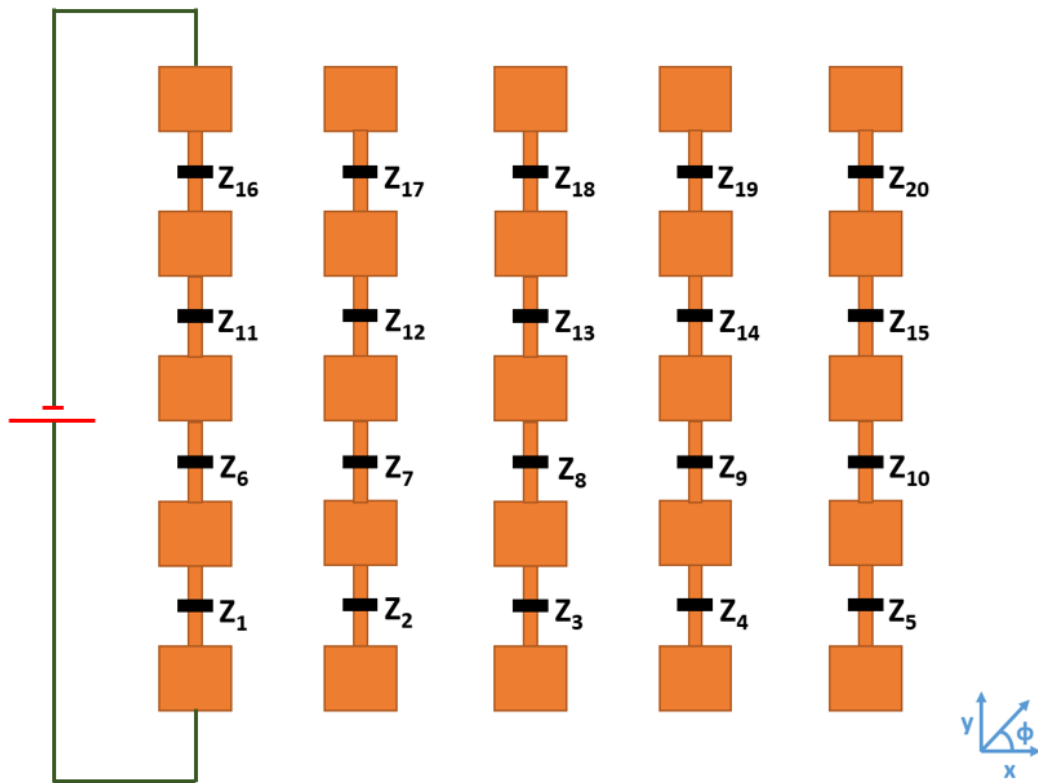


Figure 4.28: Biasing of tunable impedance circuit for the printed ESPAR antenna.

Some applications may require beam-scanning along the ϕ direction as well; in that case parasitic impedances would not be considered identical in a column. The varactor diode MAVR-011020-1411 [4] can provide tunable capacitive impedances at 24.5 GHz. For the biasing of a varactor diode, the DC bias lines can be connected through the parasitic patches themselves as shown in Fig. 4.28. This is made possible by the fact that an identical impedance is considered for all the varactors in a given column. This strongly reduces the potential impact of the biasing lines, since they only appear at the ends of the structure and so do not interfere with the array.

4.4.2 EM Model and Optimization

A computationally efficient Electromagnetic (EM) model which has been explained in Section 2.2 is utilized here for the design and analysis of the ESPAR antenna. A goal here is to maximize the directivity of the ESPAR

antenna in different directions along with different angles of θ , while $\phi = 0$ (H-plane). The cost function defined here is the inverse of the directivity in the direction of the main beam, as given below by (4.10). That is how beam-steering can be carried out while maintaining a high directivity. One of the challenges in ESPAR antennas is the deterioration of matching of the active antenna, while the beam-scanning is carried out. This problem is taken care off in the optimization process, by discarding the solutions which worsen the reflection coefficient of an active antenna. The solutions which give higher side-lobe levels (SLLs) are discarded as well, in the optimization procedure. In (4.10), A and B are the upper bounds of SLL and S_{11} , respectively. Here we have considered -9 dB as an upper bound for S_{11} and tried to achieve as small as possible SLLs.

$$\begin{aligned} \text{Cost Function} &= \arg \min_{\bar{Z}_1, \dots, \bar{Z}_N} \frac{1}{\text{Dir}(\theta, \phi)} \\ \text{Cond. 1 : SLL} &\leq A \\ \text{Cond. 2 : } |S_{11}| &\leq B \end{aligned} \tag{4.10}$$

The code [5] implementing the genetic algorithm [42] in MATLAB [37] is used in conjunction with the efficient electromagnetic model to optimize the parasitic reactive loads. For the genetic algorithm, the parameters used to reach the minima of a cost function are given in Table 4.5.

The simulations are executed on an i7 PC with 3.40 GHz processor,

Table 4.5: Genetic algorithm parameters.

Parameters	Values
Number of maximum generations (iterations)	400
Number of initial points	1200
Number of sons for each generation	700
Reproduction probability	0.8
Recombination Probability	0.9
Mutation Probability	0.05
Immigration Probability	0.8
Lower bound for initial points	-500 i Ω
Higher bound for initial points	500 i Ω

16 GB RAM and 64-bit operating system. The computation time needed for calculating all the open-circuit patterns is less than 3 minutes and more importantly, those patterns need to be computed only once. Using the open-circuit to embedded pattern approach, every iteration in the optimization takes a few milliseconds, essentially used to compute the total radiation pattern and the cost function. On the contrary, commercial software such as CST [38] takes 30-40 minutes to carry out one full-wave simulation. If parasitic loads are to be optimized using commercial softwares, they would run full-wave simulation in every iteration of the optimization process to compute the total radiation pattern. Therefore, it is computationally efficient to utilize this scheme. Although (3.9) or any equivalent formulation can be exploited with commercial software to accelerate the computation time, the open-circuit patterns calculation of all the elements would require multiple full-wave simulations. However, with the in-house method-of-moments code, all the open circuit patterns are computed very efficiently using the impedance matrix. The computation time for the optimization of parasitic impedances is of the order of 20 minutes.

4.4.3 Simulation Results

The method of moments (MoM) for layered media developed in [65] is used for the simulation of the proposed ESPAR antenna. The directivity of a simple patch antenna has been increased from 6.75 dBi to 11.5 dBi with the use of superstrate and parasitic patches on top of a microstrip patch antenna as shown in Figs. 4.29 and 4.30. A comparison is made with IE3D [39] simulations to validate the employed MoM formulation. For this purpose, the proposed antenna without any tunable impedance connected between parasitic patches is simulated with MoM and IE3D. A comparison is shown in Figs. 4.29 and 4.30, which depicts a very good agreement between MoM and IE3D results.

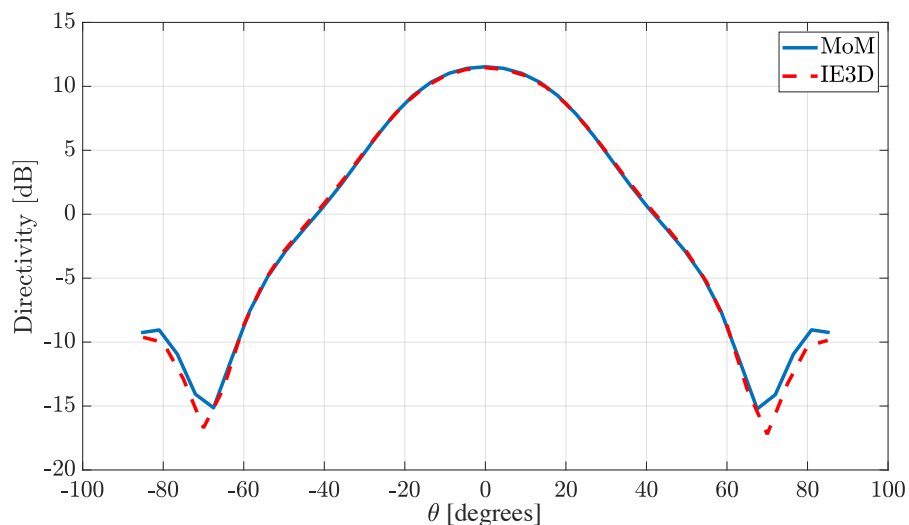


Figure 4.29: Directivity pattern of the printed ESPAR antenna without any tunable reactive elements, H-Plane $\Phi = 0^\circ$, Method of moments (MoM) vs IE3D simulations at 24.5 GHz.

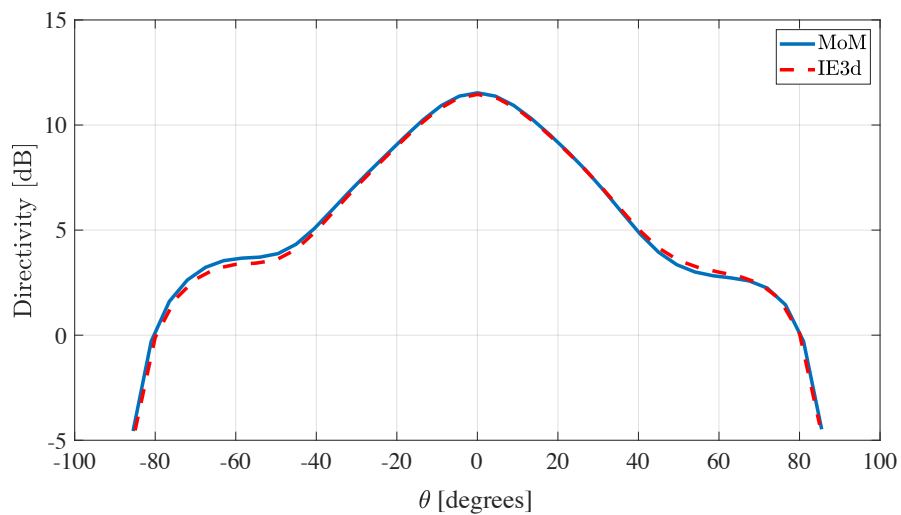


Figure 4.30: Directivity pattern of the printed ESPAR antenna without any tunable reactive elements, E-Plane $\Phi = 90^\circ$, Method of moments (MoM) vs IE3D simulations at 24.5 GHz.

Table 4.6: Parasitic loads for different beam scan angles.

Impedances	θ				
	0°	4.5°	9°	-4.5°	-9°
Z_1	+367i	+562i	+339i	+237i	+246i
Z_2	+261i	+262i	+268i	+308i	+308i
Z_3	+305i	+282i	+262i	+282i	+262i
Z_4	+255i	+308i	+308i	+262i	+268i
Z_5	+458i	+237i	+246i	+562i	+339i

Table 4.7: Radiation parameters for different beam scan angles.

Scan Angle($^\circ$)	D_{max} (dBi)	SLL $_{max}$ (dB)	S_{11} (dB)	e_a (%)
0	19.19	-14.3	-15.42	80.6
± 4.5	19.05	-11.10	-12.54	78
± 9	18.81	-11.52	-9.51	73.8

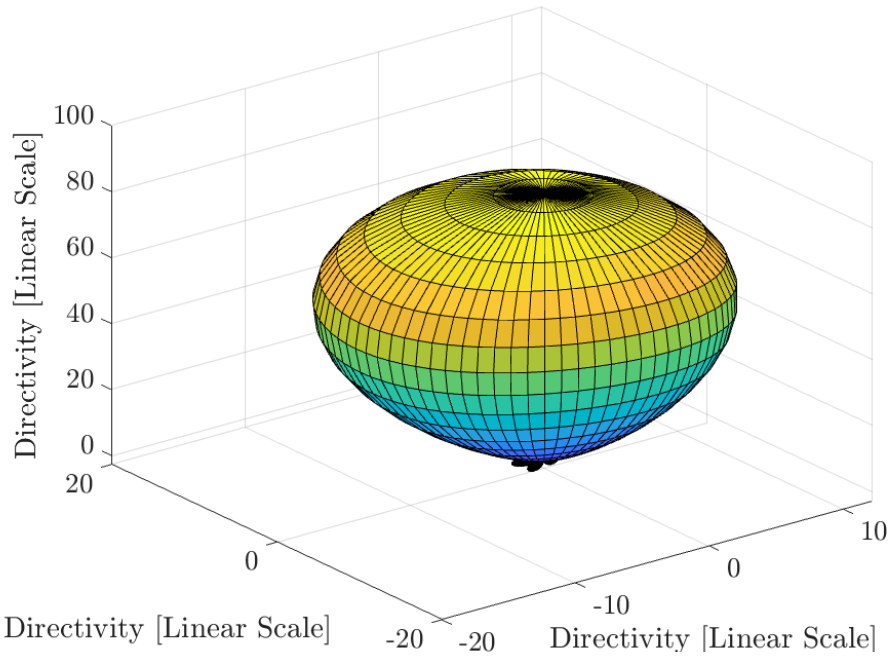


Figure 4.31: 3D radiation pattern of the printed ESPAR antenna, Beam scanned at $\theta = 0^\circ$, $\Phi = 0^\circ$, Method of moments (MoM) simulation at 24.5 GHz.

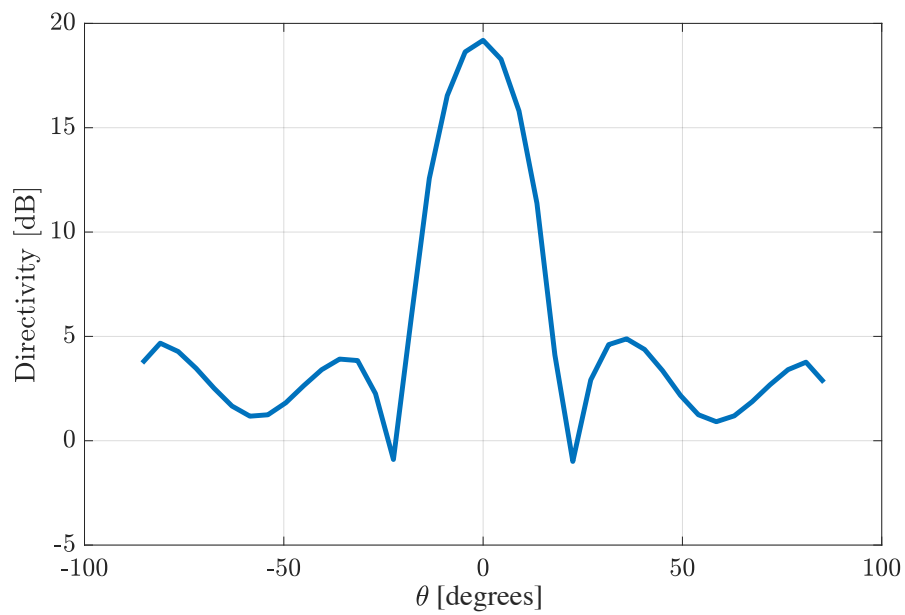


Figure 4.32: Directivity of the printed ESPAR antenna, Beam scanned at $\theta = 0^\circ$, H-Plane $\Phi = 0^\circ$, Method of moments (MoM) simulation at 24.5 GHz.

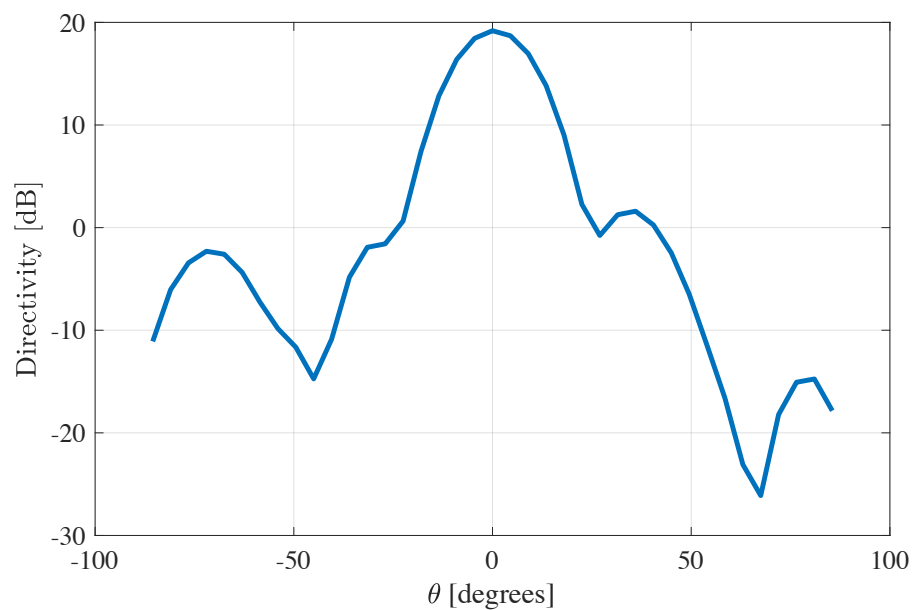


Figure 4.33: Directivity of the printed ESPAR antenna, Beam scanned at $\theta = 0^\circ$, E-Plane $\Phi = 90^\circ$, Method of moments (MoM) simulation at 24.5 GHz.

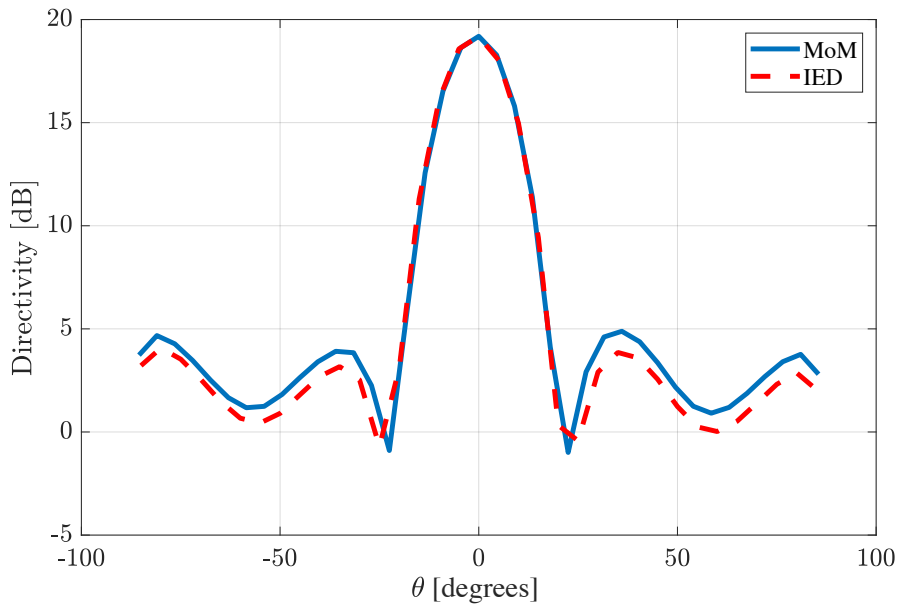


Figure 4.34: Directivity of the printed ESPAR antenna, Beam scanned at $\theta = 0^\circ$, H-Plane $\Phi = 0^\circ$, Method of moments (MoM) simulation at 24.5 GHz vs IE3D Simulation at 24.7 GHz.

By tuning the parasitic impedances, an even higher directivity can be achieved, along with a beam-steering capability. The directivity patterns of the ESPAR antenna are shown in Figs. 4.32, 4.36 and 4.39 with maxima of at least 18.5 dBi, oriented towards 0° , $\pm 4.5^\circ$ and $\pm 9^\circ$, and a side-lobe level maintained below -11 dB. Table 4.6 contains optimized reactances, computed to obtain a highly directive beam steered in respective directions. The radiation patterns are stable (within 1 dBi) over the variation of $\pm 10 i \Omega$ in the optimized parasitic loads. The side-lobe level becomes worse when the beam is scanned beyond $\pm 9^\circ$. The side-lobe levels are difficult to suppress in an ESPAR antenna, since the available range of tunable reactances provided by varactor diodes is limited.

It is noticed that the optimized loads obtained for the maximum directivity at broadside are non-symmetrical. It can be explained by an analogy with the phased arrays, a high broadside gain while minimizing SLL can be obtained in phased arrays with non-symmetrical amplitude (weighting) coefficients [67]. Since the configuration of the proposed ESPAR antenna

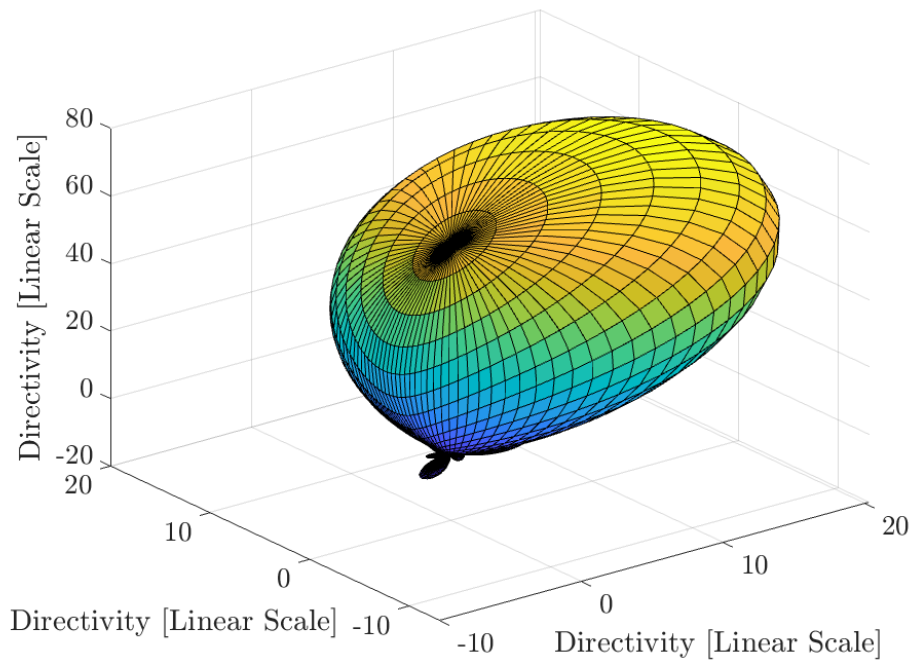


Figure 4.35: 3D radiation pattern of the printed ESPAR antenna, Beam scanned at $\theta = 4.5^\circ$, $\Phi = 0^\circ$, Method of moments (MoM) simulation at 24.5 GHz.

is symmetrical, identical impedance values in reverse order can be used to steer the beam at -4.5° and -9° .

The scanning of radiation patterns is also validated from the IE3D software [39]. However, the results from the IE3D simulations are shifted to 24.7 GHz. This shift in the frequency can be attributed to the difference in the modelling of the parasitic ports, between the in-house method-of-moments (MoM) code and the IE3D software. In MoM code, the impedances attached to the port of the parasitic elements are implemented by adding $-Z_{Li}W_i^2$ to the self-impedances of the corresponding basis functions in the MoM impedance matrix. The Z_{Li} is the impedance of the load attached to the terminals of the parasitic element i and W_i is the width of the basis function corresponding to that port (terminal). It is equivalent to the model given in (3.9). We are not aware of the implementation of the impedances attached to the ports of the parasitic elements in the IE3D software. The comparison of directivity computed from the MoM code at 24.5 GHz and the directivity computed from the IE3D software at 24.7 GHz, of different

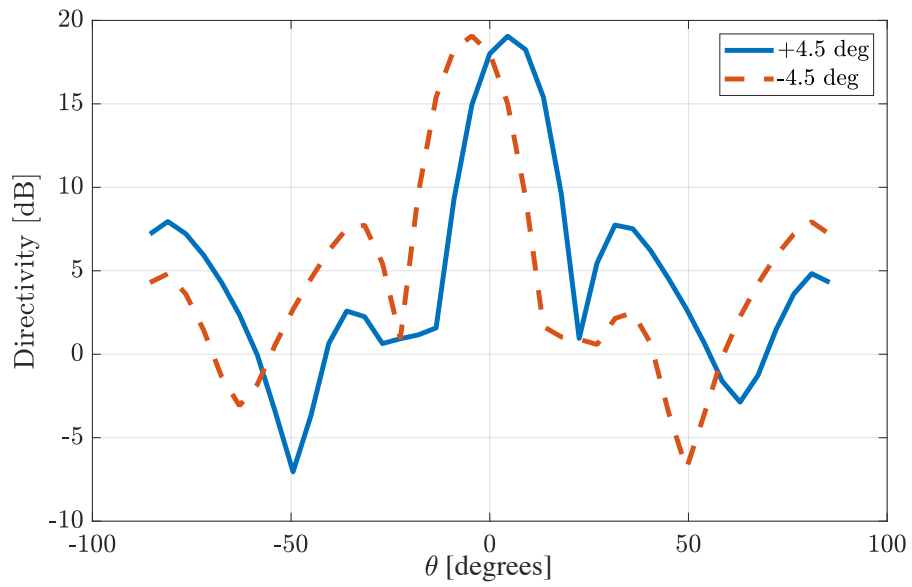


Figure 4.36: Directivity of the printed ESPAR antenna, Beam scanned at $\theta = \pm 4.5^\circ$, H-Plane $\Phi = 0^\circ$, Method of moments (MoM) simulation at 24.5 GHz.

scanned beams are shown in Fig. 4.34, 4.37 and 4.40.

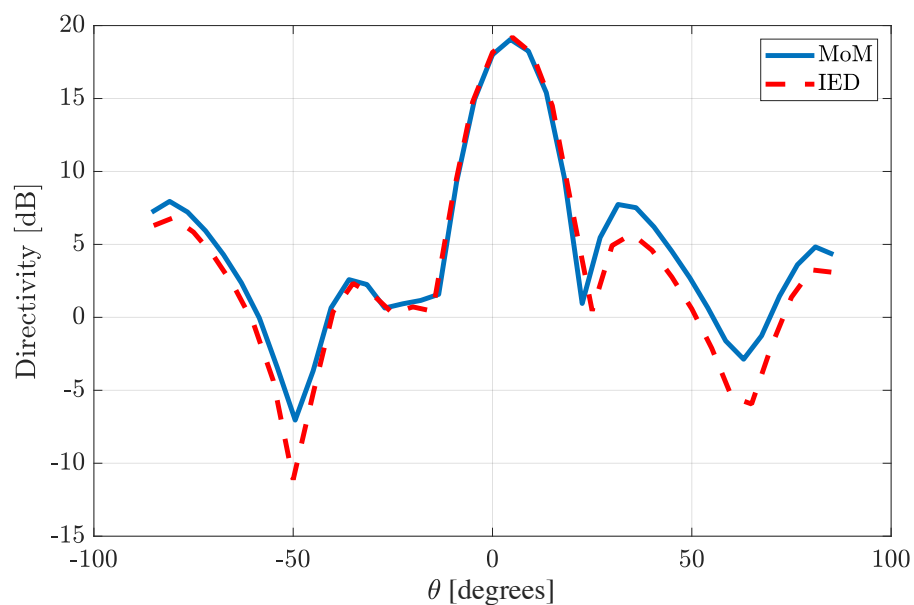


Figure 4.37: Directivity of the printed ESPAR antenna, Beam scanned at $\theta = 4.5^\circ$, H-Plane $\Phi = 0^\circ$, Method of moments (MoM) simulation at 24.5 GHz vs IE3D Simulation at 24.7 GHz.

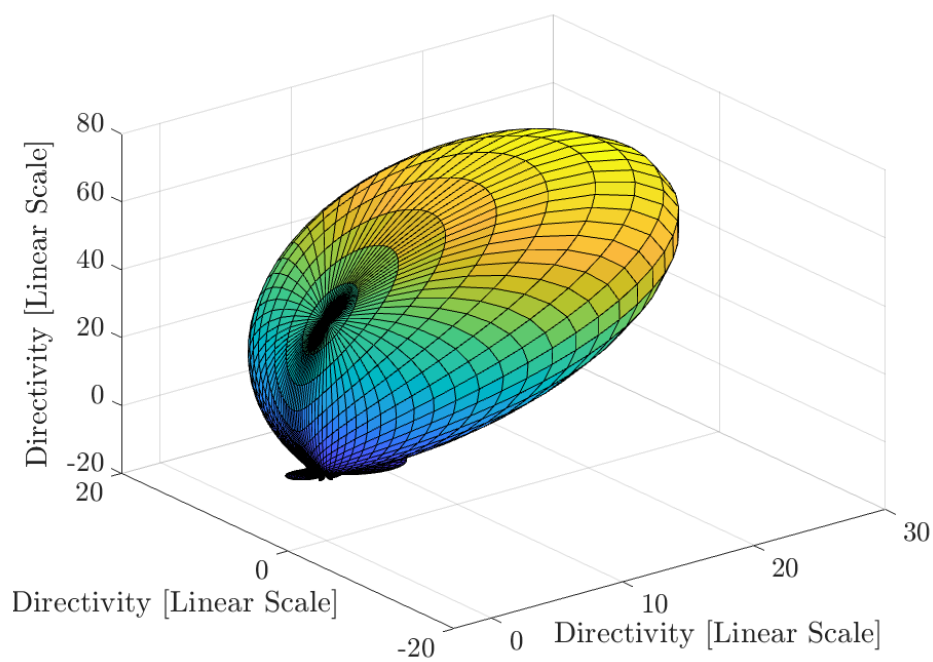


Figure 4.38: 3D radiation pattern of the printed ESPAR antenna, Beam scanned at $\theta = 9^\circ$, $\Phi = 0^\circ$, Method of moments (MoM) simulation at 24.5 GHz.

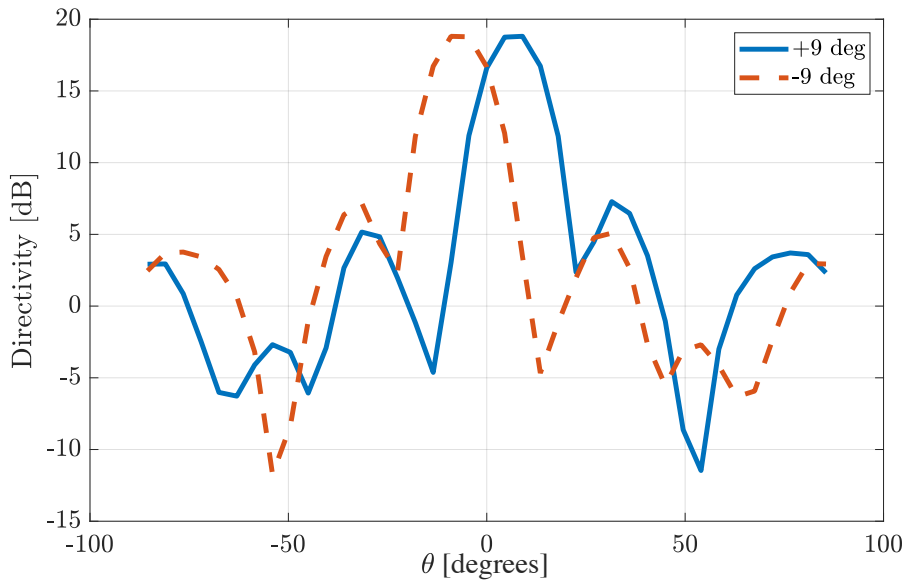


Figure 4.39: Directivity of the printed ESPAR antenna, Beam scanned at $\theta = \pm 9^\circ$, H-Plane $\Phi = 0^\circ$, Method of moments (MoM) simulation at 24.5 GHz.

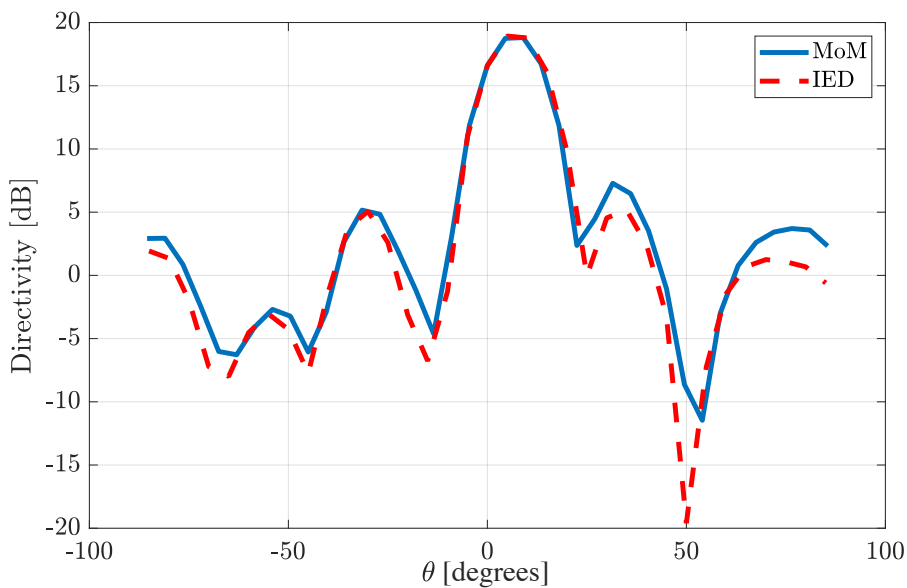


Figure 4.40: Directivity of the printed ESPAR antenna, Beam scanned at $\theta = 9^\circ$, H-Plane $\Phi = 0^\circ$, Method of moments (MoM) simulation at 24.5 GHz vs IE3D Simulation at 24.7 GHz.

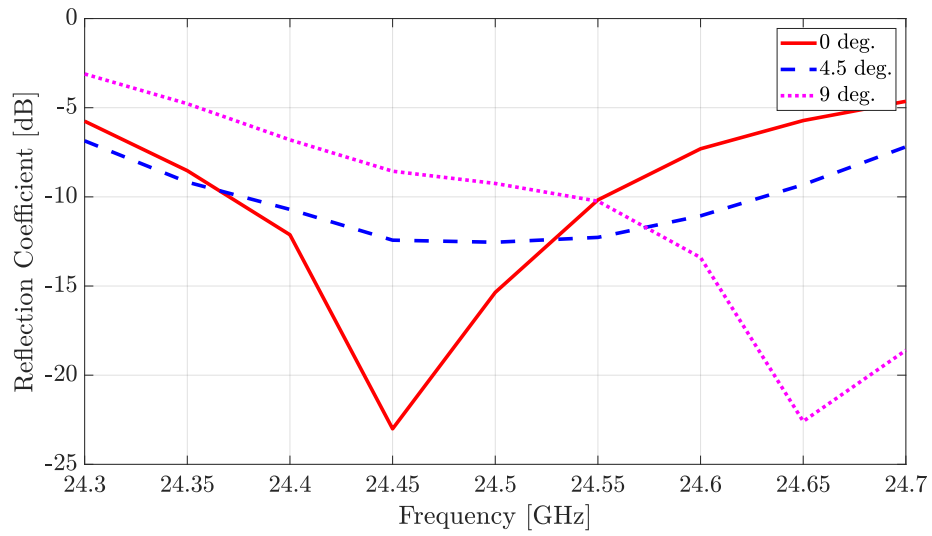


Figure 4.41: Reflection coefficient (S_{11}) vs frequency for beams scanned at $\theta = 0^\circ$, $\theta = 4.5^\circ$ and $\theta = 9^\circ$, Method of moments (MoM) simulation.

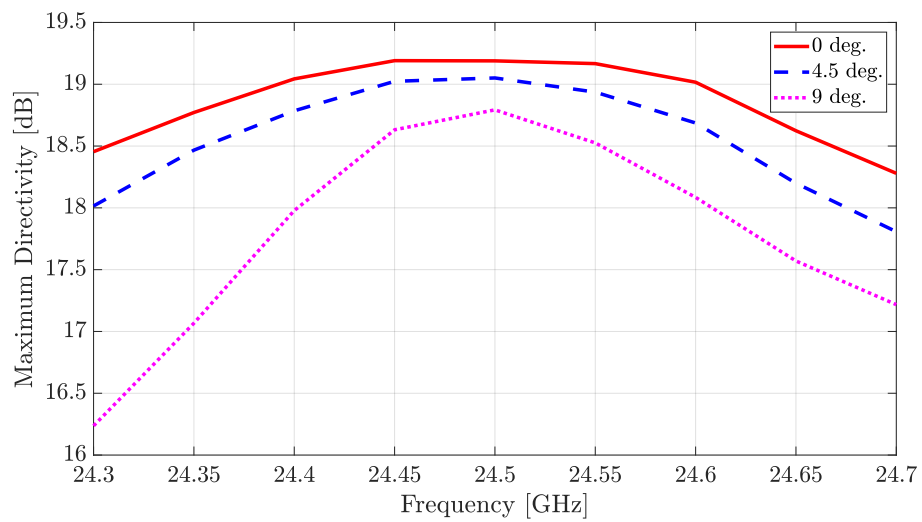


Figure 4.42: Maximum directivity vs frequency for beams scanned at $\theta = 0^\circ$, $\theta = 4.5^\circ$ and $\theta = 9^\circ$, Method of moments (MoM) simulation.

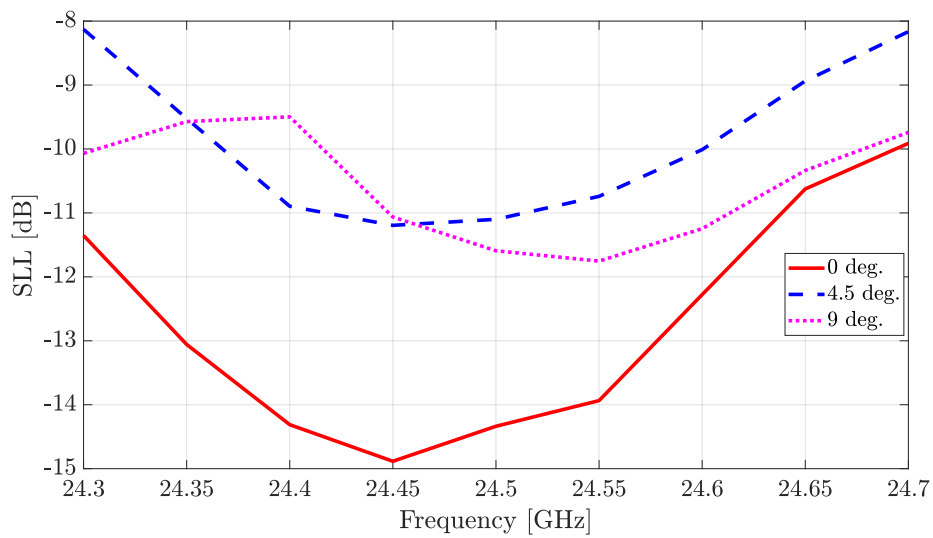


Figure 4.43: Side lobe level (SLL) vs frequency for beams scanned at $\theta = 0^\circ$, $\theta = 4.5^\circ$ and $\theta = 9^\circ$, Method of moments (MoM) simulation.

Table 4.8: Parasitic loads for different beam scan angles, considering dielectric and varactor ohmic losses.

Impedances	θ				
	0°	4.5°	9°	-4.5°	-9°
Z_1	+370i	+431i	+260i	+270i	+223i
Z_2	+260i	+261i	+265i	+286i	+297i
Z_3	+273i	+262i	+259i	+262i	+259i
Z_4	+260i	+286i	+297i	+261i	+265i
Z_5	-66i	+270i	+223i	+431i	+260i

Table 4.9: Radiation parameters for different beam scan angles, considering dielectric and varactor ohmic losses.

Scan Angle ($^\circ$)	G_{max} (dBi)	SLL_{max} (dB)	S_{11} (dB)	Efficiency (%)	e_a (%)
0	13.66	-11.24	-8.70	44.6	26.23
± 4.5	13.40	-9.54	-8.14	43.3	24.70
± 9	13.06	-9.28	-8.01	43.05	22.85

The reflection coefficient (S_{11}) of an active antenna, along with the maximum directivity (D_{max}), the side-lobe level (SLL) and the maximum aperture efficiency (e_a) of the array are given in the Table 4.7, for different scan angles. ESPAR antennas are narrow-band in nature. The bandwidth of the proposed ESPAR antenna is 150 MHz. The bandwidth can be improved, if it is included in the cost function. With the variation in frequency, the impedances of parasitic loads varies which impacts the behaviour of the parasitic layer and in turn the mutual coupling. It translates into a variation in the radiation characteristics of the ESPAR antenna. Such variations in the maximum directivity, matching (reflection coefficient) and side lobe levels (SLLs) of the ESPAR antenna for different scan angles are shown in Figs. 4.42, 4.41, 4.43, respectively. There is a significant shift in the resonance of the antenna when the beam is scanned at the angle of $\theta = 9^\circ$. The high directivity translates into higher aperture efficiencies of the ESPAR antenna, the decline in the aperture efficiency with the scan angle is related

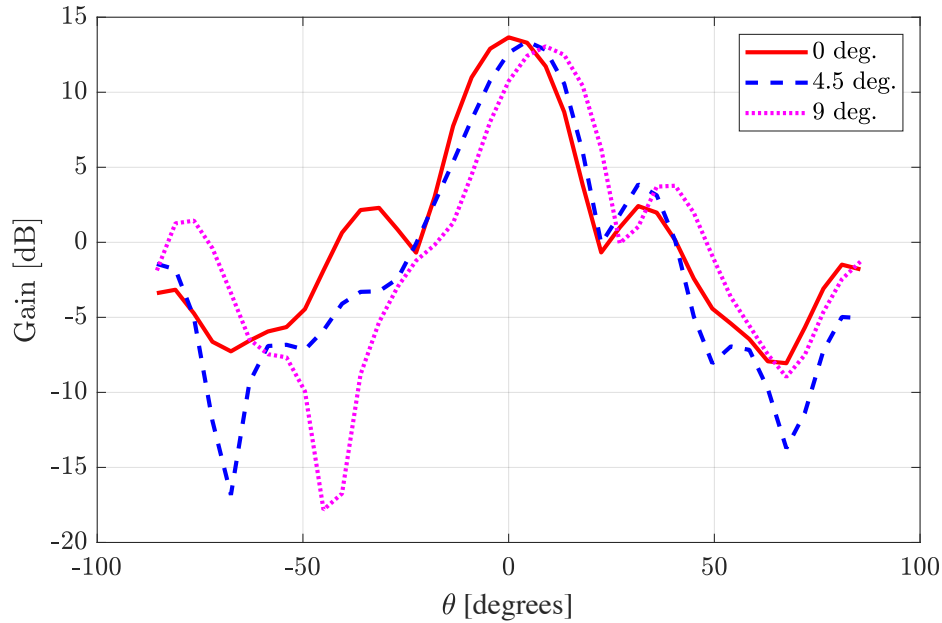


Figure 4.44: Gain comparison of the printed ESPAR antenna, Beams scanned at $\theta = 0^\circ$, $\theta = 4.5^\circ$, $\theta = 9^\circ$, H-Plane $\Phi = 0^\circ$, Method of moments (MoM) simulation at 24.5 GHz.

with the decrease in the maximum directivity. The side-lobe levels (SLLs) obtained from the proposed ESPAR antenna for scanned beams are not significantly low. The tunable capacitive and inductive reactances which are required to scan the beam can be obtained with the varactor diode MAVR-011020-1411 [4] (capacitance ranges from 0.095 pF to 0.0125 pF) and an inductor (e.g. 4.25 nH) connected in series. In order to make a working prototype at 24.5 GHz we will require an inductor with a Self Resonance Frequency (SRF) higher than 24.5 GHz. Currently available SMD inductors of 4.25 nH and 2.2 nH have a typical SRF of 10 GHz and 15 GHz, respectively. Therefore, we would need to wait for the inductors with SRF higher than 24.5 GHz to become available in the market.

If the dielectric losses (RO4350B; $\tan \delta = 0.0031$ at 2 GHz) and ohmic losses of the varactor shown in Fig. 4.9 are taken into consideration, the maximum gain will reduce. Moreover, the antenna matching and SLLs deteriorate significantly due to the inclusion of the dielectric and varactor ohmic losses. Therefore, a new optimization is carried out to maximize

the antenna gain while scanning the beam, the ohmic losses of varactor are included a priori in the optimization of the tunable loads. The varactor is characterized at 1800 MHz, the ohmic losses at 24.5 GHz could be different. Therefore, the use of varactor ohmic losses shown in Fig. 4.9 is an approximation. The gain patterns of the ESPAR antenna are shown in Figs. 4.44 with maxima of at least 13 dB, oriented towards 0° , 4.5° and 9° , and the side-lobe level maintained below -9 dB. Table 4.8 contains optimized reactances, computed to obtain a high gain beam steered in the respective directions, while considering dielectric and varactor ohmic losses. The reflection coefficient (S_{11}) of the active antenna, along with the maximum gain (G_{max}), the side-lobe level (SLL), antenna efficiency and the maximum aperture efficiency (e_a) of the array are given in Table 4.9, for different scan angles. A care must be taken while considering the dielectric losses because in reality dielectric losses are more as compared to the values given in data-sheets.

Table 4.10: Comparison of the parameters of the designed ESPAR antenna with the similar antennas presented in the literature.

Parameters	Designed Printed ESPAR Antenna	Printed ESPAR Antenna [10]	Pixel Antenna [28]
Maximum Gain	13 dB	6.5 dB	8 dB
Beam Scanning (H-plane)	$\pm 9^\circ$	Discrete angles ($+30^\circ, 0^\circ, -30^\circ$)	Discrete angles ($+30^\circ, 0^\circ, -30^\circ$)
SLLs	-9 dB	-3 dB	-7 dB
Bandwidth	<1%	4%	3%

A comparison of the parameters of the designed antenna with the similar antennas found in the literature is given in Table 4.10. The designed antenna has higher gain, better side lobe levels and continuous scanning range as compared to the similar antennas available in the literature. However, the beam scanning range is limited and the bandwidth of the designed ESPAR antenna is narrow as well which is less than 1%. The antennas proposed in [10] and [28] have a bandwidth of 3-4% because they use RF switches whose impedances do not vary with frequency. Moreover, in FPC based antennas, there is a trade-off between bandwidth and maximum gain, and

I have not considered the bandwidth in the cost function.

4.5 Conclusion

The ESPAR antenna has been developed for the beam-shaping with the base station antenna of a cellular communication. Varactor diodes are used as variable impedances to steer the beam electronically, as demonstrated with a small prototype. The simulation and experimental results of the designed ESPAR antenna are in a good agreement. Similarly, a highly directive ESPAR antenna has been proposed for radars. It can steer the beam without losing directivity, by just tuning the reactive elements attached between the parasitic patches, while biasing occurs from the ends of the structure. The non-intrusive way of biasing varactor diodes can help in suppressing spurious radiations from the biasing lines. The simulation results of the ESPAR antenna printed on a layered medium have been validated using the commercial software IE3D. The dielectric and varactor ohmic losses decrease the maximum gain and deteriorate the matching of a driven antenna. Another round of optimization is carried out to maximize the antenna gain while including dielectric and varactor ohmic losses. The simulations show that the designed ESPAR antenna can achieve a gain of at least 13 dB while carrying out a beam scanning in the range of $\pm 9^\circ$ with the side lobe level (SLLs) of -9 dB.

CHAPTER 5

Antenna Array for the Automotive Radar

This chapter is related to the work that has been carried out to develop the beamforming antenna arrays for the automotive radar. However, this chapter is confidential due to a non-disclosure agreement with an industrial partner.

CHAPTER 6

Conclusions and Future Works

6.1 Conclusions

Beam shaping antenna arrays are getting popular these days for use in commercial civilian applications. In that perspective, this thesis has been focused on the design, optimization, fabrication and measurements of such antenna arrays to implement beamforming and beam-shaping in 5G mobile communication systems and automotive radar applications.

An exact and computationally efficient EM model has been used in this thesis for the design of parasitic antenna arrays. An attempt has been made to analytically compute the loads, attached to the parasitic elements, to form the desired radiation patterns. However, it leads to unrealistic load values with the negative real parts. Therefore, an optimization algorithm needs to be used to determine the load values. Since different optimization algorithms have their own pros and cons, a spectral optimization method has been proposed to optimize the loads, so as to realize the objective radiation patterns. In a spectral optimization method, harmonic and Gaussian bases have been proposed and their comparison has been made with a genetic algorithm. The comparison suggests that the spectral method converges towards a better solution in a much shorter time than the genetic algorithm.

Parasitic antenna arrays are cheaper than the phased arrays, which has

motivated their use in non-military applications. In this thesis, parasitic antenna arrays have been designed for base station of a cellular communication system (4G or 5G) in order to improve coverage in an area. In order to enhance the throughput in a given area, the objective radiation patterns of base station antennas have been determined by Quentin Gueuning through ray-tracing simulation tools. Then, the objective radiation patterns are implemented by designing the parasitic antenna array at 1800 MHz. The design and optimization of a parasitic antenna array has been accelerated by the use of an EM model which utilizes the open-circuit patterns of all the antenna elements, as well as the array impedance matrix, to include all the mutual coupling information. Furthermore, a proposed harmonic optimization technique has been utilized to compute the dynamic loads of a parasitic antenna array to yield the objective (desired) radiation patterns. The parasitic antenna arrays have been fabricated and the measurement results show good agreement with the simulation results. The realistic example of given neighbourhood has been taken where coverage improvement has been shown by adapting the base station radiation pattern with the parasitic antenna array.

An ESPAR (Electronically Steerable Parasitic Array Radiator) antenna has been designed and implemented for a cellular communication system at 1800 MHz. Varactor diodes have been utilized to adapt the radiation pattern electronically. The measurement results are in good agreement with the simulation results. However, the adapting capability of the array can be further enhanced by increasing the number of parasitic elements. Similarly, an ESPAR antenna printed on a layered medium has been designed for a radar application at 24.5 GHz. It has an electronic beam steering capability while maintaining a high gain.

In recent years radars have found their way in the automotive sector. For that purpose, antenna arrays have been designed in the 24 GHz and 76 GHz band.

A summary of the original contributions is given below:

1. An attempt to analytically design a parasitic antenna array [Chapter 2].

2. A spectral optimization method to optimize the loads in a parasitic antenna array [Chapter 2].
3. A parasitic antenna array design for base stations to enhance the coverage in a cellular communication system. [Chapter 3].
4. An ESPAR antenna design for a cellular communication system [Chapter 4].
5. A design of an ESPAR antenna printed on a layered medium, for a radar application [Chapters 4].
6. A non-intrusive way of biasing varactor diodes in a printed ESPAR antenna [Chapters 4].
7. Confidential
8. Confidential
9. Confidential
10. Confidential

6.2 Future Works

This thesis work has led to new pathways to explore in the field of antenna arrays comprising parasitic elements. In particular, the future works include the improvement in the design methodology of a parasitic antenna array, the design of a dual band ESPAR antenna with a beam shaping capability.

The design of a parasitic antenna array entails solving a non-linear optimization problem which is computationally very expensive. Moreover, the array synthesis problem to shape a beam by phase-only control is a non-convex optimization problem. However, the array synthesis problem can be formulated as a convex one by relaxing the constraints which can help to solve the problem using a SemiDefinite Relaxation (SDR) technique [68].

In an ESPAR antenna, the behaviour of parasitic layer changes with frequency and hence the radiation pattern varies as well. ESPAR antennas comprising a parasitic pixel layer have been developed with simultaneous

reconfigurability in frequency, radiation pattern and polarization [9], [69]. They switch among different radiation patterns at different frequencies but in a same frequency band. However, we would like to develop dual band ESPAR antenna with a simultaneous beam shaping capability to cater different bands of a cellular communication system e.g. 900 MHz and 1800 MHz. Moreover, the parasitic radiating elements can be redesigned in order to achieve reconfigurability in terms of polarization as well.

APPENDIX A

Green's Functions in Layered Substrates

A.1 Introduction

In this appendix we present the rigorous development of the Green's functions for layered media used in this thesis. Most part of this appendix has been taken from the Appendix A of Simon Hubert's thesis [70]. Some detailed proofs and corrections have been introduced.

By definition, in electromagnetics, the Green's function is the spatial impulse response of a given medium; that is, the field radiated by a unitary point current source with given polarization. The field radiated by any current distribution in a given medium can then be obtained by a convolution with the pertaining Green's function.

In layered media, frontal analysis of fields radiated by point sources is not straightforward. However, the propagation of plane waves in such media is a simple problem that can be seen as a generalization of transmission lines theory. The traditional method (seeing [71], [72], [73]), which is recalled in detail in this appendix, thus consists of decomposing the source in a spectrum of planar current sheets, such that the Green's function (and thus

the radiated fields) is expressed as a spectrum of plane waves.

We begin by recalling the spectral decomposition of discrete and periodic sources in Section A.2. Then the propagation of plane waves in layered media is recalled in Section A.3, and finally in Section A.4 we derive the spectral Green's functions using the previously established tools, and present examples of remarkable media configurations.

A.2 Spectral analysis

To start with, a horizontal current point source with amplitude J and orientation \hat{a} in the (x, y) plane is assumed as

$$\mathbf{J}(x, y, z) = J \delta(x) \delta(y) \delta(z) \hat{a} \quad (\text{A.1})$$

This point source can be decomposed into an infinite constant spectrum of current sheets with linear phase progression, via a 2D Fourier transform in the (x, y) direction.

$$\mathbf{J}(x, y, z) = J \delta(z) \hat{a} \frac{1}{(2\pi)^2} \iint_{-\infty}^{\infty} e^{-jk_x x} e^{-jk_y y} dk_x dk_y \quad (\text{A.2})$$

Each current sheet component of (A.2) radiates an upward-propagating plane wave above itself, and a downward-propagating plane wave below it.

In the case of an infinitely periodic array of scatterers, the analysis of a single unit cell is enabled by the definition of a periodic Green's function. It is defined as the field radiated by an infinite array of point sources such as

$$\mathbf{J}^P(x, y, z) = J \delta(z) \hat{a} \sum_{m,n} \delta(x - m\Delta x) e^{-jm\phi_x} \delta(y - n\Delta y) e^{-jn\phi_y} \quad (\text{A.3})$$

with Δx , Δy and ϕ_x , ϕ_y the spacing and phase difference between two adjacent cells. Knowing that the Fourier transform of a Dirac comb function

is another Dirac comb function, that is

$$\sum_m \delta(x - am) = \frac{1}{2\pi} \int_{-\infty}^{\infty} \frac{2\pi}{a} \sum_p \delta\left(k_x - p\frac{2\pi}{a}\right) e^{-jk_x x} dk_x \quad (\text{A.4})$$

and replacing the discrete phase shift between unit cells $\exp(-jm\phi_x)$ by a linear phase function $\exp(-j\phi_x \frac{x}{\Delta x})$ sampled by the Dirac comb, and identifying that spatial complex modulation with a spectral shift, we can rewrite (A.3) as

$$\begin{aligned} \mathbf{J}^P(x, y, z) = J \delta(z) \hat{a} \frac{1}{(2\pi)^2} \iint_{-\infty}^{\infty} e^{-jk_x x} e^{-jk_y y} \\ \sum_{p,q} \delta\left(k_x - p\frac{2\pi}{\Delta x} - \frac{\phi_x}{\Delta x}\right) \delta\left(k_y - q\frac{2\pi}{\Delta y} - \frac{\phi_y}{\Delta y}\right) dk_x dk_y \end{aligned} \quad (\text{A.5})$$

which is simplified into a discrete spectrum of current sheets as

$$\mathbf{J}^P(x, y, z) = J \delta(z) \hat{a} \frac{1}{(2\pi)^2} \sum_{p,q} e^{-jk_x^p x} e^{-jk_y^q y} \quad (\text{A.6})$$

$$\text{with } \begin{cases} k_x^p = \frac{2\pi}{\Delta x} p + \frac{\phi_x}{\Delta x} \\ k_y^q = \frac{2\pi}{\Delta y} q + \frac{\phi_y}{\Delta y} \end{cases} \quad (\text{A.7})$$

The spectrum of plane waves radiated by a periodic array of point sources is thus also discrete, with transversal wavenumbers k_x^p and k_y^q defined in (A.7) and denoted as ‘‘Floquet harmonics’’ [74], [75].

A.3 Plane wave propagation

In this section, the propagation of plane waves under the influence of monotonic plane current sheets will be developed.

A.3.1 Definitions

Let us consider a homogeneous medium in the xy plane, and piecewise homogeneous in the z direction. That is, the medium is constituted of a number of homogeneous layers, each characterized by their own permittivity ϵ and impedance $\eta = \sqrt{\mu/\epsilon}$. In such a structure, the plane waves phase

progression along the x and y coordinates is preserved across the layers (only the propagation along z will be affected by the different media).

Plane waves propagating in layered media are generally described as

$$\mathbf{E}^\pm = (-\hat{m} E_{TE}^\pm + \hat{e}^\pm E_{TM}^\pm) e^{-jk_x x} e^{-jk_y y} e^{\mp jk_z z} \quad (\text{A.8})$$

$$\mathbf{H}^\pm = \frac{1}{\eta} (\hat{e}^\pm E_{TE}^\pm + \hat{m} E_{TM}^\pm) e^{-jk_x x} e^{-jk_y y} e^{\mp jk_z z} \quad (\text{A.9})$$

where the subscripts $+$ and $-$ denote respectively waves propagating upward and downward, and the wavenumber \mathbf{k} is defined as

$$\mathbf{k} = \begin{bmatrix} k_x \\ k_y \\ \pm k_z \end{bmatrix} \quad (\text{A.10})$$

with the following definitions

$$k \triangleq |\mathbf{k}| = \sqrt{k_x^2 + k_y^2 + k_z^2} \in \mathbf{C} \quad (\text{A.11})$$

$$\beta \triangleq k_x^2 + k_y^2 \in \mathbf{R} \quad (\text{A.12})$$

$$\Re\{k_z\} \leq 0 \quad (\text{A.13})$$

The characteristic directions used above are defined as

$$\hat{k} \triangleq \frac{\mathbf{k}}{k} \quad (\text{A.14})$$

$$\hat{m} \triangleq -\frac{\hat{k} \times \hat{z}}{\|\hat{k} \times \hat{z}\|} = \frac{1}{\beta} \begin{bmatrix} -k_y \\ k_x \\ 0 \end{bmatrix} \quad (\text{A.15})$$

$$\hat{e}^\pm \triangleq -\frac{\hat{k} \times \hat{m}}{\|\hat{k} \times \hat{m}\|} = \frac{1}{\beta k} \begin{bmatrix} \pm k_x k_z \\ \pm k_y k_z \\ -\beta^2 \end{bmatrix} \quad (\text{A.16})$$

These unit vectors are chosen according to the physics of the problem and form an orthonormal basis that satisfies

$$\hat{k} = \hat{e} \times \hat{m} \quad (\text{A.17})$$

This basis eases the analysis and leads to elegant formulations; it is illustrated in Figure A.1. It is indeed interesting to note that \hat{m} is always parallel to the interfaces between layers, which leads to define Transverse Electric (TE) components as waves which present an electric field solely along \hat{m} . In the same way, we define Transverse Magnetic (TM) components as waves which present a magnetic field solely along \hat{m} . In the literature, \hat{e} and \hat{m} are thus sometimes denoted respectively as $\hat{\theta}$ and $\hat{\phi}$, or \hat{e}_{TM} and \hat{e}_{TE} . In

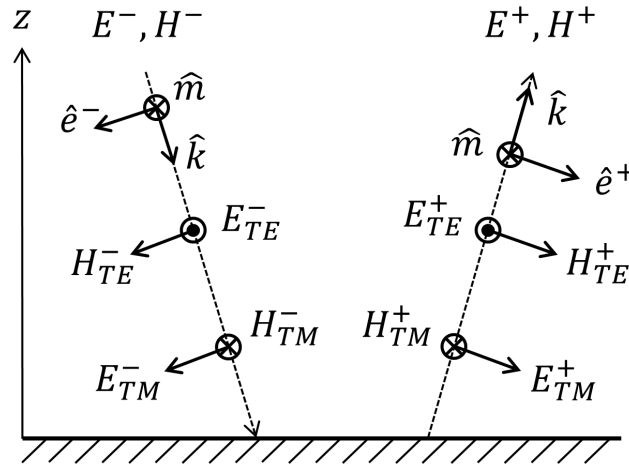


Figure A.1: Representation of the vector basis for the representation of plane waves in layered media. Note the difference for the \hat{e} and \hat{k} vectors for upward and downward waves.

the special case where $\beta = 0$, the formulation leads to an indetermination that we solve by defining the limit

$$\hat{m}\Big|_{\beta=0} \triangleq \begin{bmatrix} -\sin \phi \\ \cos \phi \\ 0 \end{bmatrix} \quad \hat{e}^{\pm}\Big|_{\beta=0} \triangleq \begin{bmatrix} \pm \cos \phi \\ \pm \sin \phi \\ 0 \end{bmatrix} \quad (\text{A.18})$$

Note that in this representation, $k_z = \sqrt{k^2 - \beta^2}$ does not change sign when considering upward or downward waves: instead the orientation of the transversal component of \hat{e} and the vertical component of \hat{k} changes.

In the remainder of this document, we will very often omit the complex exponentials in the developments and expressions to improve readability.

A.3.2 Reflection coefficients at a single interface

When a plane wave reaches an interface between two media with different characteristics, waves are reflected and transmitted. This section defines the reflection coefficients on a single interface between two semi-infinite media.

We define the reflection coefficients on both sides of this interface as the ratio between the coefficient of the wave incident to the interface and the coefficient of the reflected wave, that is

$$\Gamma^u \triangleq \frac{E^{u-}}{E^{u+}} \qquad \Gamma^d \triangleq \frac{E^{d+}}{E^{d-}} \qquad (\text{A.19})$$

with the subscripts u and d denoting the upper and lower media, as presented in Figure A.2. Since we showed that TE and TM waves are orthogo-

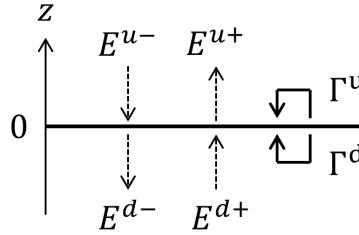


Figure A.2: Definition and notation of reflection coefficients in terms of upward and downward plane waves across a single interface.

nal to each other, it is possible to show that their analysis can be completely decoupled. That is, we can consider both contributions separately and then recombine them in the final solution. As an example, if the upper medium is a perfect electric conductor (PEC), then no waves are transmitted and everything is reflected, such that the tangential electric field on the interface vanishes. Since there are no fields in the upper medium, only Γ^d is relevant to determine and the aforementioned boundary condition is satisfied with

$$\Gamma_{TE}^d = -1 \qquad \Gamma_{TM}^d = 1 \qquad (\text{A.20})$$

We observe that the reflection coefficient is different for TE and TM waves. Moreover, the TM coefficient does not agree with usual transmission line

theory, which by convention shows negative reflection coefficients on short circuits¹. The (A.20) also holds for Γ^u with the PEC medium located below.

To determine these reflection coefficients on a general interface with no sources, the usual boundary conditions need to be satisfied on the interface, that is

$$\hat{z} \times \mathbf{E}^u = \hat{z} \times \mathbf{E}^d \quad (\text{A.21})$$

$$\hat{z} \times \mathbf{H}^u = \hat{z} \times \mathbf{H}^d \quad (\text{A.22})$$

which means respectively that the total tangential electric and magnetic fields have to be continuous across the interface. At this point, we note the following useful relations that we will extensively exploit in the development of the expressions

$$\hat{z} \times \hat{m} = \frac{1}{\beta} \begin{bmatrix} -k_x \\ -k_y \\ 0 \end{bmatrix} \quad (\text{A.23})$$

$$\hat{z} \times \hat{e}_u^+ = \frac{ct_u}{\beta} \begin{bmatrix} -k_y \\ k_x \\ 0 \end{bmatrix} = \pm \frac{ct_u}{ct_d} \hat{z} \times \hat{e}_d^\pm \quad (\text{A.24})$$

$$ct \triangleq \frac{k_z}{k} = \cos \theta \quad (\text{A.25})$$

with θ the angle from normal of \hat{k} in a given layer.

With a unit downward incoming wave from the upper medium, the amplitude of the reflected wave is $1/\Gamma^u$. Imposing (A.21) and (A.22) in the upper and lower media, we obtain the expressions of the reflection coefficients for a single interface between two semi-infinite media.

$$\Gamma_{TE}^u = \frac{ct_u \eta_d + ct_d \eta_u}{ct_u \eta_d - ct_d \eta_u} \quad \Gamma_{TM}^u = \frac{ct_u \eta_u + ct_d \eta_d}{ct_u \eta_u - ct_d \eta_d} \quad (\text{A.26})$$

$$\Gamma_{TE}^d = \frac{ct_d \eta_u + ct_u \eta_d}{ct_d \eta_u - ct_u \eta_d} \quad \Gamma_{TM}^d = \frac{ct_d \eta_d + ct_u \eta_u}{ct_d \eta_d - ct_u \eta_u} \quad (\text{A.27})$$

¹As a matter of fact there is no simple way to define a mathematical framework that suits both a convenient orthonormal basis for the fields and transmission line theory.

Finally, we note that (A.26) leads to (A.20) when $\eta_d = 0$, which is the case when the lower medium is a PEC and that (A.26) and (A.27) are consistent with the well-known Fresnel reflection coefficients [76].

A.3.3 Reflection coefficients on multiple interfaces

When the medium consists of a finite number of layers, waves are transmitted and reflected at each layer, which leads to more complex expressions for the reflection coefficients. Figure A.3 presents the notations we use for several layers. Interfaces are numbered from 0 to n and reflection coefficients are defined on both sides of each interface. We will now define the method-

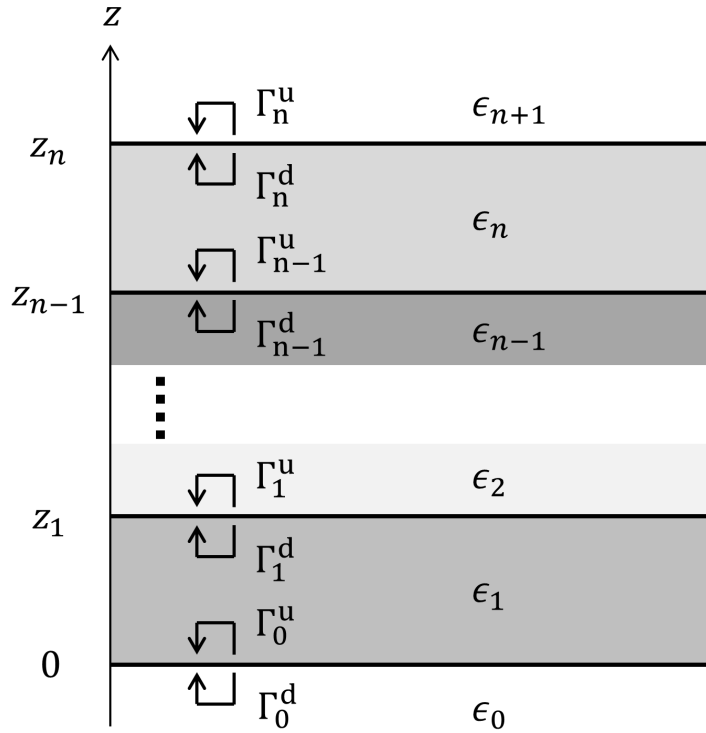


Figure A.3: Definition and numbering of the reflection coefficients in multilayer media.

ology to determine the reflection coefficients at each layer, for an incoming upward wave, similar to what is found in a number of classical references (see [72]). We start by showing that **the last reflection coefficient is obtained trivially**. If the last medium (above interface n) is a semi-infinite

dielectric or magnetic medium, waves going out of the last interface will never be reflected, which leads to $\Gamma_{n,TE}^u = \Gamma_{n,TM}^u = 0$. If the last medium is a PEC, (A.20) holds and we have $\Gamma_{n,TE}^d = -1$ and $\Gamma_{n,TM}^d = 1$.

We continue by deriving the relation between reflection coefficients as we go deeper into the layers. Across one (source free) interface, the boundary conditions (A.21) and (A.22) need to be satisfied, which leads to the transition rule across the interface. The transition rule is derived below for the interface between medium 0 (bottom layer) and medium 1 (top layer), referring to the interface 0 in Fig A.3. From Fig. A.1 and (A.15), (A.16), we can observe the following relations

$$\hat{m}^d = \hat{m}^u = \hat{m} \quad (\text{A.28})$$

$$\hat{e}_t^d = -\hat{e}_t^u \quad (\text{A.29})$$

where the t index refers to the component tangential to the XY plane. The continuity conditions of tangential electric and magnetic fields at the interface are applied below. For **TE waves**:

$$E_{TE}^{d-} [-\hat{m}_t^d + \Gamma_{0,TE}^d (-\hat{m}_t^u)] = E_{TE}^{u+} [-\hat{m}_t^u + \Gamma_{0,TE}^u (-\hat{m}_t^d)] \quad (\text{A.30})$$

$$E_{TE}^{d-} \left[\frac{\hat{e}_t^d}{\eta_d} + \Gamma_{0,TE}^d \left(\frac{\hat{e}_t^u}{\eta_d} \right) \right] = E_{TE}^{u+} \left[\frac{\hat{e}_t^u}{\eta_u} + \Gamma_{0,TE}^u \left(\frac{\hat{e}_t^d}{\eta_u} \right) \right] \quad (\text{A.31})$$

Using (A.28) and (A.29) provides us,

$$E_{TE}^{d-} [1 + \Gamma_{0,TE}^d] = E_{TE}^{u+} [1 + \Gamma_{0,TE}^u] \quad (\text{A.32})$$

$$-\frac{ct_d}{\eta_d} E_{TE}^{d-} [1 - \Gamma_{0,TE}^d] = \frac{ct_u}{\eta_u} E_{TE}^{u+} [1 - \Gamma_{0,TE}^u] \quad (\text{A.33})$$

Solving (A.32) and (A.33) simultaneously, leads to

$$-\frac{ct_d}{\eta_d} r_{0,TE}^d = \frac{ct_u}{\eta_u} r_{0,TE}^u \quad (\text{A.34})$$

where, to ease the notation we used the quantity r , which has a bilinear

relation with the reflection coefficient.

$$r \triangleq \frac{1 - \Gamma}{1 + \Gamma} \quad (\text{A.35})$$

Similarly, for **TM waves**:

$$E_{TM}^{d-} \left[\frac{\hat{m}_t^d}{\eta_d} + \Gamma_{0,TM}^d \left(\frac{\hat{m}_t^u}{\eta_d} \right) \right] = E_{TM}^{u+} \left[\frac{\hat{m}_t^u}{\eta_u} + \Gamma_{0,TM}^u \left(\frac{\hat{m}_t^d}{\eta_u} \right) \right] \quad (\text{A.36})$$

$$E_{TM}^{d-} [\hat{e}_t^d + \Gamma_{0,TM}^d (\hat{e}_t^u)] = E_{TM}^{u+} [\hat{e}_t^u + \Gamma_{0,TM}^u (\hat{e}_t^d)] \quad (\text{A.37})$$

Using (A.28) and (A.29) provides us,

$$\frac{E_{TM}^{d-}}{\eta_d} [1 + \Gamma_{0,TM}^d] = \frac{E_{TM}^{u+}}{\eta_u} [1 + \Gamma_{0,TM}^u] \quad (\text{A.38})$$

$$-E_{TM}^{d-} ct_d [1 - \Gamma_{0,TM}^d] = E_{TM}^{u+} ct_u [1 - \Gamma_{0,TM}^u] \quad (\text{A.39})$$

Solving (A.38) and (A.39) simultaneously, leads to

$$-ct_d \eta_d r_{0,TM}^d = ct_u \eta_u r_{0,TM}^u \quad (\text{A.40})$$

Hence, from (A.34) and (A.40), the general **transition rule across the interface i** are

$$\frac{ct_u}{\eta_u} r_{i,TE}^u = -\frac{ct_d}{\eta_d} r_{i,TE}^d \quad (\text{A.41})$$

$$ct_u \eta_u r_{i,TM}^u = -ct_d \eta_d r_{i,TM}^d \quad (\text{A.42})$$

Besides, following the definition of the reflection coefficients (A.19), we obtain the following **translation rule between two interfaces i and $i - 1$** , which holds both for TE and TM waves :

$$\Gamma_{i-1}^u = \frac{1}{\Gamma_i^d} \exp \left(-2j k_z^{i,d} (z_i - z_{i-1}) \right) \quad (\text{A.43})$$

where $k_z^{i,d}$ is defined by (A.11) and (A.13) just below interface i .

To summarize, here is the procedure to determine the reflection coefficients everywhere, starting from the upper interface :

1. Determine the first reflection coefficient directly, depending on whether the end boundary is a PEC or a semi-infinite medium.
2. Use the transition rule to determine the reflection coefficient just below the interface.
3. Use the translation rule to determine the reflection coefficient just above the next interface.
4. Repeat steps 2 and 3 until all reflection coefficients have been determined.

Note that if the medium is not backed by a ground plane, another set of reflection coefficients needs to be determined for an incoming downward wave, with the methodology described above. That is, the transition and translation rules remain rigorously the same, but the first coefficient now needs to be determined at the lower end of the medium and the iterative procedure needs to be applied going up the layers. We differentiate these different sets of reflection coefficients by a $+$ or $-$ superscript, denoting the direction of the original incoming wave.

A.3.4 Propagation of plane waves in a multilayer slab

Now the reflection coefficients have been determined, we focus on how to compute the electric and magnetic fields everywhere in the multi-layered medium in the presence of an incoming plane wave. As before, we take the example of an upward plane wave impinging on the lower interface, and we propagate the electric field across and between the interfaces.

Using again the continuity of the electric field (A.21) across interfaces, we obtain the relation between the upward waves just above and below the interface i

$$E_{TE}^{u+} = \frac{E_{TE}^{d+}}{\Gamma_{TE}^{d+}} \frac{1 + \Gamma_{TE}^{d+}}{1 + \Gamma_{TE}^{u+}} \quad E_{TM}^{u+} = -\frac{ct_d}{ct_u} \frac{E_{TM}^{d+}}{\Gamma_{TM}^{d+}} \frac{1 - \Gamma_{TM}^{d+}}{1 - \Gamma_{TM}^{u+}} \quad (\text{A.44})$$

where we omitted the subscript i for all quantities. Note that for two identical media (that is, no interface) we obtain $E^{u+} = E^{d+}$ because $\Gamma^u = 0$ and $\Gamma^d \rightarrow \infty$, for both TE and TM components.

The propagation of the electric field between interface i and $i + 1$ is obtained trivially through

$$E_{i+1}^{d\pm} = E_i^{u\pm} \exp(\mp j k_z [z_{i+1} - z_i]) \quad (\text{A.45})$$

which holds for both TE and TM components, with k_z defined between the two interfaces. Now, we can compute the total tangential electric field and magnetic field at the interface.

When several metallizations are present, it is necessary in a MoM scheme, to determine the field on layer 1 due to a current on layer 0. We will assume layer 1 is above layer 0. Fields on layer 0 from currents on layer 1 are obtained by reciprocity. As shown in Fig. A.4 with two layers, the transmitted E_0^+ and reflected E_0^- waves are known at layer 0. We would like to determine the transmitted E_1^+ and reflected E_1^- waves at layer 1. Consider E_0^- as the reflection of E_0^+ and E_1^+ as the reflection of E_1^- .

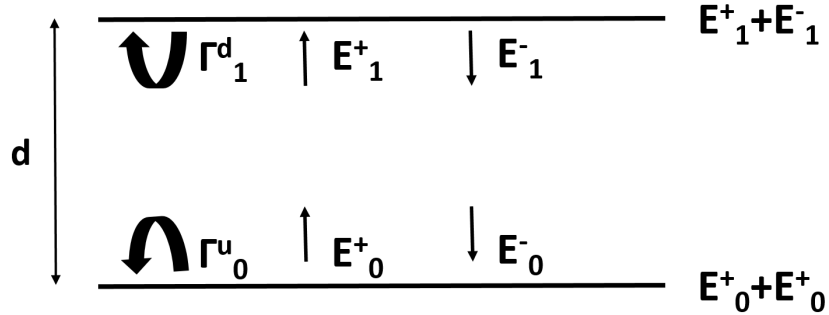


Figure A.4: Electric field translation in a multilayer medium.

$$E_0^- = \Gamma_0^u E_0^+ \quad (\text{A.46})$$

$$E_1^+ = \Gamma_1^d E_1^- \quad (\text{A.47})$$

After transfer of the reflection coefficient

$$\Gamma_0^u \Gamma_1^d = e^{-2jk_z d} \quad (\text{A.48})$$

From Fig. A.4, it appears that

$$E_0^+ = E_1^+ e^{jk_z d} \quad (\text{A.49})$$

$$E_0^- = E_1^- e^{-jk_z d} \quad (\text{A.50})$$

The total field on layer 0 is $E_0^+ + E_0^-$, and on layer 1 it is $E_1^+ + E_1^-$. For TE waves:

$$E_0^+ + E_0^- = E_1^+ \left(e^{jk_z d} + \frac{1}{\Gamma_1^d} e^{-jk_z d} \right) \quad (\text{A.51})$$

$$E_1^+ + E_1^- = \left(e^{jk_z d} + \frac{1}{\Gamma_1^d} e^{-jk_z d} \right) \left(1 + \frac{1}{\Gamma_1^d} \right) (E_0^+ + E_0^-) \quad (\text{A.52})$$

Similarly, for TM waves, with opposite signs of the reflection coefficients we can write the relation as below:

$$E_1^+ + E_1^- = \left(e^{jk_z d} - \frac{1}{\Gamma_1^d} e^{-jk_z d} \right) \left(1 - \frac{1}{\Gamma_1^d} \right) (E_0^+ + E_0^-) \quad (\text{A.53})$$

Relations (A.51) and (A.52) allow transferring total fields between consecutive layers, which is very useful when the MoM needs to be applied in layered media comprising metallization on different interfaces. In that case, it is important to be able to test on a given interface field radiated by currents on another interface.

A.3.5 Waves emitted by a monotonic current sheet

We now consider the same multi-layered medium as in the previous section, but with a planar monotonic current sheet lying on one interface at $z = 0$ for simplicity. That current sheet is thus expressed as

$$\tilde{\mathbf{J}} = J \hat{a} e^{-jk_x x} e^{-jk_y y} \quad (\text{A.54})$$

with J the amplitude of the current and \hat{a} a unit vector. These sources will emit upward plane waves above the source interface and downward plane waves below it. We will now derive the expression of these waves first for the simple case of a single interface, and then in a general multi-layered

medium. The described approach is similar to that found in [77].

A.3.5.1 On a single interface

First we express the current sheet into an orthonormal basis $(\hat{J}_{TE}, \hat{J}_{TM})$ where each component emits only TE or TM waves respectively.

$$\begin{aligned}\tilde{\mathbf{J}} &= J_x \hat{x} + J_y \hat{y} \\ &= J_{TE} \hat{J}_{TE} + J_{TM} \hat{J}_{TM}\end{aligned}\quad (\text{A.55})$$

with the orthonormal basis defined by

$$\hat{J}_{TE} \triangleq \frac{\hat{z} \times \hat{e}_u^+}{ct_u} = -\frac{\hat{z} \times \hat{e}_d^-}{ct_u} = \frac{1}{\beta} \begin{bmatrix} -k_y \\ k_x \\ 0 \end{bmatrix} \quad (\text{A.56})$$

$$\hat{J}_{TM} \triangleq \hat{z} \times \hat{m} = \frac{1}{\beta} \begin{bmatrix} -k_x \\ -k_y \\ 0 \end{bmatrix} \quad (\text{A.57})$$

which in the case of normal incidence reduces to

$$\hat{J}_{TE} \Big|_{\beta=0} \triangleq \begin{bmatrix} -\sin \phi \\ \cos \phi \\ 0 \end{bmatrix} \quad (\text{A.58})$$

$$\hat{J}_{TM} \Big|_{\beta=0} \triangleq \begin{bmatrix} -\cos \phi \\ -\sin \phi \\ 0 \end{bmatrix} \quad (\text{A.59})$$

In that way we easily determine the amplitudes and phases of the emitted waves on both sides of the source for each component.

The boundary conditions to be enforced on the interface with sources now are

$$\hat{z} \times \mathbf{E}^u = \hat{z} \times \mathbf{E}^d \quad (\text{A.60})$$

$$\hat{z} \times (\mathbf{H}^u - \mathbf{H}^d) = \tilde{\mathbf{J}} \quad (\text{A.61})$$

The proof is similar to the one explained in Section A.3.3 except, there is a jump condition in the H-field given in (A.61). The proof leads to the expressions of the electric field plane waves emitted on both sides of the interface

$$E_{TE}^{u+} = \frac{1}{D_{TE}} \quad E_{TM}^{u+} = \frac{1}{ct_u D_{TM}} \quad (\text{A.62})$$

$$E_{TE}^{d-} = E_{TE}^{u+} \quad E_{TM}^{d-} = -\frac{ct_u}{ct_d} E_{TM}^{u+} \quad (\text{A.63})$$

with the coefficients D defined as follows to simplify the notation.

$$D_{TE} \triangleq \frac{ct_u}{\eta_u} r_{TE}^{u+} + \frac{ct_d}{\eta_d} r_{TE}^{d-} \quad D_{TM} \triangleq \frac{1}{\eta_u ct_u r_{TM}^{u+}} + \frac{1}{\eta_d ct_d r_{TM}^{d-}} \quad (\text{A.64})$$

To obtain the total field radiated by a monotonic current sheet with an arbitrary orientation, one just needs to vectorially sum up the fields of either (A.62) or (A.63). As an example, for the wave emitted just above the interface we have

$$\mathbf{E}^{u+} = -\hat{m} J_{TE} E_{TE}^{u+} + \hat{e}_u^+ J_{TM} E_{TM}^{u+} \quad (\text{A.65})$$

with the coefficients J obtained through the projection

$$J_{TE} = \tilde{\mathbf{J}} \cdot \hat{J}_{TE} \quad J_{TM} = \tilde{\mathbf{J}} \cdot \hat{J}_{TM} \quad (\text{A.66})$$

A.3.5.2 In a multilayered medium

If, in a multilayer substrate consisting of n interfaces, there is a monotonic current sheet defined by (A.55) at the interface c , that is at $z = z_c$, waves emitted by the sources are reflected on both sides.

Let us start from the boundary conditions expressed in (A.60) and (A.61); this time, the total tangential field on both sides of the interface at $z = z_c$ must be the sum of the outgoing emitted wave and the incident reflected wave. This means that we need the expression of the reflection coefficients at the level of the source, looking upward and downward, that is Γ_c^{u+} and Γ_c^{d-} , which can both be obtained using the procedure detailed in

Section A.3.3. Imposing the continuity of tangential electric and magnetic fields leads to

$$E_{TE}^{u+} = \frac{1}{1 + \Gamma_{TE}^{u+}} \frac{1}{D_{TE}} \quad E_{TM}^{u+} = \frac{1}{1 - \Gamma_{TM}^{u+}} \frac{1}{ct_u D_{TM}} \quad (\text{A.67})$$

$$E_{TE}^{d-} = \frac{1 + \Gamma_{TE}^{u+}}{1 + \Gamma_{TE}^{d-}} E_{TE}^{u+} \quad E_{TM}^{d-} = -\frac{ct_u}{ct_d} \frac{1 - \Gamma_{TM}^{u+}}{1 - \Gamma_{TM}^{d-}} E_{TM}^{u+} \quad (\text{A.68})$$

with the coefficients D_{TE} and D_{TM} still defined in (A.64).

A.4 Green's functions in the spectral domain

The spectral Green's function can be seen as the amplitude of the tangential field radiated by a monotonic unit current sheet with given spectral components k_x , k_y , and given polarization vector. In its most general form, the spectral Green's functions is dyadic and can be written as the Fourier transform of the dyadic Green's function.

$$\tilde{\mathbf{E}}(k_x, k_y) = \tilde{\mathbf{G}}(k_x, k_y) \tilde{\mathbf{J}}(k_x, k_y) \quad (\text{A.69})$$

In the free-space case,

$$\mathbf{G}(\mathbf{r}, \mathbf{r}') = -j\omega\mu \left(G(\mathbf{r}, \mathbf{r}') + \frac{1}{k^2} \nabla \nabla \cdot G(\mathbf{r}, \mathbf{r}') \right) \quad (\text{A.70})$$

Starting from (A.67), we will first derive the total tangential field on any interface. For convenience, we will express it as a function of the Cartesian (x, y) components of the source current \mathbf{J} . On a particular layer i above or on the level of the source, the total tangential field can be expressed as

$$\mathbf{E}_t = \mathbf{E}_{TE}^{u+} (1 + \Gamma_{TE}^{u+}) + \mathbf{E}_{TM}^{u+} \Big|_t (1 - \Gamma_{TM}^{u+}) \quad (\text{A.71})$$

where we omitted the subscript i for conciseness, and the subscript t stands for dumping the z component of the vector. Similarly, the total tangential field on a layer i below or on the source interface can be expressed as

$$\mathbf{E}_t = \mathbf{E}_{TE}^{d-} (1 + \Gamma_{TE}^{d-}) + \mathbf{E}_{TM}^{d-} \Big|_t (1 - \Gamma_{TM}^{d-}) \quad (\text{A.72})$$

A.4.1 Interaction on the same layer

In the case where observation and source planes coincide, (A.71) reduces to the closed-form expression

$$\begin{bmatrix} E_x \\ E_y \end{bmatrix} = -\hat{n} \frac{J_{TE}}{D_{TE}} + \hat{e}_u^+ \Big|_t \frac{J_{TM}}{ct_u D_{TM}} \quad (\text{A.73})$$

$$= \frac{1}{\beta^2} \begin{bmatrix} -k_y^2 & k_x k_y \\ k_x k_y & -k_x^2 \end{bmatrix} \frac{1}{D_{TE}} \begin{bmatrix} J_x \\ J_y \end{bmatrix} + \frac{1}{\beta^2} \begin{bmatrix} -k_x^2 & -k_x k_y \\ -k_x k_y & -k_y^2 \end{bmatrix} \frac{1}{D_{TM}} \begin{bmatrix} J_x \\ J_y \end{bmatrix} \quad (\text{A.74})$$

which can be rewritten in this final formulation :

$$\mathbf{E}_t = -\frac{1}{D_{TE}} \tilde{\mathbf{J}} + \frac{1}{\beta^2} \left(\frac{1}{D_{TE}} - \frac{1}{D_{TM}} \right) \begin{bmatrix} k_x^2 & k_x k_y \\ k_x k_y & k_y^2 \end{bmatrix} \tilde{\mathbf{J}} \quad (\text{A.75})$$

We then define the spectral **scalar Green's functions** \tilde{G}_A and \tilde{G}_V as

$$\tilde{G}_A(\beta) = -\frac{1}{D_{TE}} \quad \tilde{G}_V(\beta) = \frac{1}{\beta^2} \left(\frac{1}{D_{TE}} - \frac{1}{D_{TM}} \right) \quad (\text{A.76})$$

such that, by identification, the spectral dyadic Green's function is expressed as

$$\tilde{\mathbf{G}}(k_x, k_y) = \tilde{G}_A \mathbf{I} + \tilde{G}_V \begin{bmatrix} k_x^2 & k_x k_y \\ k_x k_y & k_y^2 \end{bmatrix} \quad (\text{A.77})$$

with \mathbf{I} the identity matrix, (A.77) allows one to conclude that the tensor is a $\text{grad}\{\text{div}\{\}\}$ operator in the XY plane. This means that, upon convolution with source currents, the second term can be written (with change of sign) as $\text{grad}\{\text{div}\{\mathbf{P}\}\}$ where \mathbf{P} is the convolution between G_V and source currents as given in (A.78). When computing elements of the impedance matrix, the above property will allow a simplification which is also used in free-space MoM (i.e. transferring the $\text{grad}\{\text{div}\{\}\}$ operator onto basis and testing functions) in Section 3.4.3.

$$\mathbf{E}(\mathbf{r}) = \iint G_A(\mathbf{r}, \mathbf{r}') \mathbf{J}(\mathbf{r}') d\mathbf{r}' + \nabla \nabla \cdot \iint G_V(\mathbf{r}, \mathbf{r}') \mathbf{J}(\mathbf{r}') d\mathbf{r}' \quad (\text{A.78})$$

A.4.2 Special cases

A.4.2.1 Homogeneous medium

In the particular case where the medium is homogeneous (or, equivalently, all the layers are made of the same material), we obtain the following remarkable functions

$$\tilde{G}_A^{hom}(\beta) = -\frac{k_0 \eta_0}{2k_z} \quad \tilde{G}_V^{hom}(\beta) = \frac{\eta_0}{k_0} \frac{1}{2\epsilon_r k_z} \quad (\text{A.79})$$

with ϵ_r the relative permittivity of the homogeneous medium, and k_z the unique transversal wavenumber. In the homogeneous case, their inverse Fourier transform is known analytically as

$$\begin{aligned} G_A^{hom}(R) &= \frac{1}{(2\pi)^2} \iint_{-\infty}^{\infty} \frac{-k_0 \eta_0}{2k_z} e^{-j(k_x(x-x') + k_y(y-y') + k_z|z-z'|)} dk_x dk_y \\ &= -jk_0 \eta_0 \frac{e^{-jkR}}{4\pi R} \end{aligned} \quad (\text{A.80})$$

$$G_V^{hom}(R) = -j \frac{\eta_0}{k_0 \epsilon_r} \frac{e^{-jkR}}{4\pi R} \quad (\text{A.81})$$

with $R = \sqrt{(x-x')^2 + (y-y')^2 + (z-z')^2}$ the distance between the source and observation points. The latter expressions may be used for homogeneous medium extraction to improve speed and accuracy in the numerical integration of the spectral Green's functions. This well known numerical optimization does not depend on the Green's function formulation and won't be detailed here.

A.4.2.2 Single layer substrate

In this section we discuss the very simple yet practical and common case where the antennas are printed on a single layer dielectric substrate backed by a perfect electric conductor. The structure is thus composed of 3 medi-

ums (PEC, substrate and air) separated by two interfaces (the ground plane, and plane containing the antennas, as depicted in Figure A.5. It is often not

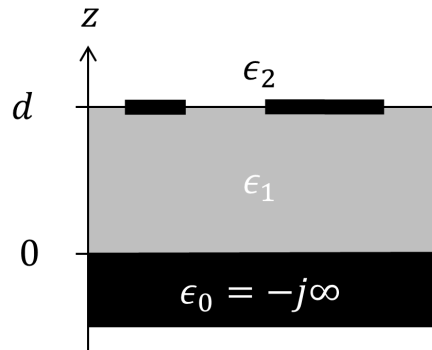


Figure A.5: Structure of the single layer substrate. The perfect electric conductors are marked with thick black lines.

practical to analytically develop the expressions of \tilde{G}_A and \tilde{G}_V , which leads to cumbersome expressions after a fastidious derivation. However, in this case the commonness of the example justifies the effort, and the expressions are reasonably compact.

The resulting expressions of the spectral **scalar Green's functions for a single layer substrate** are

$$\tilde{G}_A(\beta) = -j k_0 \eta_0 \frac{\sin(k_{z,1}d)}{\mathcal{T}_e} \quad (\text{A.82})$$

$$\tilde{G}_V(\beta) = j \frac{\eta_0}{k_0} \frac{\sin(k_{z,1}d)}{\beta^2} \left(\frac{k_0^2}{\mathcal{T}_e} - \frac{k_{z,1}k_{z,2}}{\mathcal{T}_m} \right) \quad (\text{A.83})$$

with

$$\mathcal{T}_e = j k_{z,2} \sin(k_{z,1}d) + k_{z,1} \cos(k_{z,1}d) \quad (\text{A.84})$$

$$\mathcal{T}_m = \epsilon_{r,1} k_{z,2} \cos(k_{z,1}d) + j \epsilon_{r,2} k_{z,1} \sin(k_{z,1}d) \quad (\text{A.85})$$

as can be found in [74, 78].

APPENDIX **B**

Working Principle of the
Antenna for the Automotive
Radar

Confidential

List of Publications and Research Talk

Journal Paper

- J1.** H. A. Kayani, Q. Gueuning, N. Goreux, D. Vanhoenacker-Janvier, C. Oestges and C. Craeye, "Reconfigurable Cellular Base Station Antenna Consisting of Parasitic Radiators," in IEEE Transactions on Industrial Electronics, vol. 67, no. 8, pp. 7083-7093, Aug. 2020.

Conference Papers

- C1.** H. A. Kayani, K. Alkhalifeh and C. Craeye, "Open-circuit to embedded pattern approach with harmonic optimization in ESPAR," 2017 IEEE MTT-S International Conference on Numerical Electromagnetic and Multiphysics Modeling and Optimization for RF, Microwave, and Terahertz Applications (NEMO), Seville, 2017, pp. 31-33.
- C2.** H. A. Kayani and C. Craeye, "A High Directivity Beam-Steering Parasitic Antenna Array," 2019 49th European Microwave Conference (EuMC), Paris, France, 2019, pp. 29-32.

- C3.** D. Tihon, H. B. Van, **H. Ali Kayani** and C. Craeye, "Simplified treatment of three-media junctions using the Method of Moments," 2018 International Conference on Electromagnetics in Advanced Applications (ICEAA), Cartagena des Indias, 2018, pp. 244-246.
- C4.** M. Bodehou, S. Hubert, **H. Ali Kayani**, C. Craeye and I. Huynen, "Analysis of Elliptical Aperture Metasurface Antennas," 2018 12th International Congress on Artificial Materials for Novel Wave Phenomena (Metamaterials), Espoo, 2018, pp. 84-86.

Bibliography

- [1] [Online]. Available: <https://www.airforce-technology.com/news/newsfrench-dga-aesa-rafale>
- [2] [Online]. Available: <https://pedroc.co.uk/content/ee-three-modern-masts>
- [3] KATHREIN Antennen Electronics, “2-multi-band F-panel dual polarization half-power beam width adjust. electr. downtilt,” 2017, Data Sheet. [Online]. Available: https://www.kathrein.com/en/products/antennas-accessories/outdoor-antennas/?L=&id=&tx_solr%5Bq%5D=742236
- [4] MACOM, “Solderable GaAs constant gamma flip-chip varactor diode MAVR-011020-1411,” 2017, Data Sheet. [Online]. Available: <http://cdn.macom.com/datasheets/mavr-011020-1141.pdf>
- [5] “MathWorks, Simple example of genetic algorithm for optimization problems, Dec. 2011.”
- [6] A. H. Naqvi and S. Lim, “Review of recent phased arrays for millimeter-wave wireless communication,” *Sensors*, vol. 18, no. 10, p. 3194, 2018.
- [7] R. Harrington, “Reactively controlled directive arrays,” *IEEE Trans. Antennas Propag.*, vol. 26, no. 3, pp. 390–395, May 1978.

- [8] T. Ohira and K. Iigusa, "Electronically steerable parasitic array radiator antenna," *Electronics and Comm. in Japan (Part II: Electronics)*, vol. 87, no. 10, pp. 25–45, 2004.
- [9] D. Rodrigo, B. A. Cetiner, and L. Jofre, "Frequency, radiation pattern and polarization reconfigurable antenna using a parasitic pixel layer," *IEEE Transactions on Antennas and Propagation*, vol. 62, no. 6, pp. 3422–3427, 2014.
- [10] Z. Li, E. Ahmed, A. M. Eltawil, and B. A. Cetiner, "A beam-steering reconfigurable antenna for WLAN applications," *IEEE Trans. Antennas Propag.*, vol. 63, no. 1, pp. 24–32, Jan. 2015.
- [11] P. Lotfi, S. Soltani, and R. D. Murch, "Printed endfire beam-steerable pixel antenna," *IEEE Trans. Antennas Propag.*, vol. 65, no. 8, pp. 3913–3923, Aug 2017.
- [12] J. J. Luther, S. Ebadi, and X. Gong, "A microstrip patch electronically steerable parasitic array radiator (espar) antenna with reactance-tuned coupling and maintained resonance," *IEEE Trans. Antennas Propag.*, vol. 60, no. 4, pp. 1803–1813, April 2012.
- [13] B. Schaer, K. Rambabu, J. Bornemann, and R. Vahldieck, "Design of reactive parasitic elements in electronic beam steering arrays," *IEEE Trans. Antennas Propag.*, vol. 53, no. 6, pp. 1998–2003, Jun. 2005.
- [14] C. Craeye and D. Gonzalez-Ovejero, "A review on array mutual coupling analysis," *Radio Science*, vol. 46, no. 2, pp. 1–25, Apr. 2011.
- [15] I. Gupta and A. Ksienski, "Effect of mutual coupling on the performance of adaptive arrays," *IEEE Trans. Antennas Propag.*, vol. 31, no. 5, pp. 785–791, Sep. 1983.
- [16] M. Ohira, A. Miura, M. Taromaru, and M. Ueba, "Efficient gain optimization techniques for azimuth beam/null steering of inverted-F multipoint parasitic array radiator (MuPAR) antenna," *IEEE Trans. Antennas Propag.*, vol. 60, no. 3, pp. 1352–1361, Mar. 2012.
- [17] R. Islam and R. Adve, "Beam-forming by mutual coupling effects of parasitic elements in antenna arrays," in *Proc. IEEE Int. Symp. Antennas Propag. Soc.*, vol. 1, San Antonio June 2002, pp. 126–129 vol.1.

- [18] J. Aelterman, R. Goossens, F. Declercq, and H. Rogier, "Ant colony optimisation-based radiation pattern manipulation algorithm for electronically steerable array radiator antennas," *IET Sci. Meas. Tech.*, vol. 3, no. 4, pp. 302–311, Jul. 2009.
- [19] H. A. Kayani, K. Alkhalifeh, and C. Craeye, "Open-circuit to embedded pattern approach with harmonic optimization in ESPAR," in *Proc. IEEE MTT-S Int. Conf. Num. Electromag. Multiphys. Model. Optim. RF, Microw. Terah. App. (NEMO)*, Sevilla May 2017, pp. 31–33.
- [20] D. R. Jackson and A. A. Oliner, "A leaky-wave analysis of the high-gain printed antenna configuration," *IEEE Trans. Antennas Propag.*, vol. 36, no. 7, pp. 905–910, July 1988.
- [21] D. R. Jackson, A. A. Oliner, and A. Ip, "Leaky-wave propagation and radiation for a narrow-beam multiple-layer dielectric structure," *IEEE Trans. Antennas Propag.*, vol. 41, no. 3, pp. 344–348, March 1993.
- [22] H. Ostner, J. Detlerfsen, and D. R. Jackson, "Radiation from one-dimensional dielectric leaky-wave antennas," *IEEE Trans. Antennas Propag.*, vol. 43, no. 4, pp. 331–339, April 1995.
- [23] A. P. Feresidis and J. C. Vardaxoglou, "High gain planar antenna using optimised partially reflective surfaces," *IEE Proceedings - Microwaves, Antennas and Propagation*, vol. 148, no. 6, pp. 345–350, Dec 2001.
- [24] R. Gardelli, M. Albani, and F. Capolino, "Array thinning by using antennas in a Fabry Perot cavity for gain enhancement," *IEEE Trans. Antennas Propag.*, vol. 54, no. 7, pp. 1979–1990, July 2006.
- [25] G. V. Trentini, "Partially reflecting sheet arrays," *IRE Trans. Antennas Propag.*, vol. 4, no. 4, pp. 666–671, October 1956.
- [26] K. Konstantinidis, A. P. Feresidis, and P. S. Hall, "Multilayer partially reflective surfaces for broadband Fabry-Perot cavity antennas," *IEEE Trans. Antennas Propag.*, vol. 62, no. 7, pp. 3474–3481, July 2014.
- [27] D. Kim and J.-I. Choi, "Analysis of a high-gain Fabry-Perot cavity antenna with an fss superstrate: effective medium approach," *Progress In Electromagnetics Research*, vol. 7, pp. 59–68, 2009.

- [28] X. Yuan, Z. Li, D. Rodrigo, H. S. Mopidevi, O. Kaynar, L. Jofre, and B. A. Cetiner, "A parasitic layer-based reconfigurable antenna design by multi-objective optimization," *IEEE Trans. Antennas Propag.*, vol. 60, no. 6, pp. 2690–2701, Jun. 2012.
- [29] A. R. Weily, T. S. Bird, and Y. J. Guo, "A reconfigurable high-gain partially reflecting surface antenna," *IEEE Trans. Antennas Propag.*, vol. 56, no. 11, pp. 3382–3390, Nov 2008.
- [30] "8 ghz to 16 ghz, 4-channel, x band and ku band beamformer," 2019, Data Sheet. [Online]. Available: <https://www.analog.com/media/en/technical-documentation/data-sheets/ADAR1000.pdf>
- [31] L. Ge, X. Yang, Z. Dong, D. Zhang, and X. Zeng, "Reconfigurable magneto-electric dipole antennas for base stations in modern wireless communication systems," *Wireless Comm. Mobile Comput.*, 2018.
- [32] A. Edalati and T. A. Denidni, "High-gain reconfigurable sectoral antenna using an active cylindrical FSS structure," *IEEE Trans. Antennas Propag.*, vol. 59, no. 7, pp. 2464–2472, Jul. 2011.
- [33] M. Bouslama, M. Traii, T. A. Denidni, and A. Gharsallah, "Beam-switching antenna with a new reconfigurable frequency selective surface," *IEEE Antennas Wireless Propag. Lett.*, vol. 15, pp. 1159–1162, 2016.
- [34] J. Lau and S. Hum, "Reconfigurable transmitarray design approaches for beamforming applications," *IEEE Trans. Antennas Propag.*, vol. 60, no. 12, pp. 5679–5689, Dec 2012.
- [35] H. A. Kayani, Q. Gueuning, N. Goreux, D. Vanhoenacker-Janvier, C. Oestges, and C. Craeye, "Reconfigurable cellular base station antenna consisting of parasitic radiators," *IEEE Transactions on Industrial Electronics*, vol. 67, no. 8, pp. 7083–7093, 2020.
- [36] H. A. Kayani and C. Craeye, "A high directivity beam-steering parasitic antenna array," in *2019 49th European Microwave Conference (EuMC)*, 2019, pp. 29–32.

- [37] “MATLAB 2014a, The MathWorks, Natick.” [Online]. Available: <https://mathworks.com/products/matlab.html>
- [38] “CST studio suite 2017, CST-computer simulation technology AG.” [Online]. Available: <https://www.cst.com/solutions/markets/antennas>
- [39] “IE3D, Hyperlynx, 3D EM, Release 15.2, 2012, Mentor Graphics, Wilsonville, OR, USA.”
- [40] “Advance Design System 2016, Keysight EEsof EDA.” [Online]. Available: <https://www.keysight.com/main/software>
- [41] D. Rodrigo and L. Jofre, “Frequency and radiation pattern reconfigurability of a multi-size pixel antenna,” *IEEE Trans. Antennas Propag.*, vol. 60, no. 5, pp. 2219–2225, May 2012.
- [42] M. Mitchell, *An introduction to genetic algorithms*. MIT press, 1998.
- [43] D. F. Kelley, “Relationships between active element patterns and mutual impedance matrices in phased array antennas,” in *IEEE Antennas Propag. Soc. Int. Symp.*, vol. 1, San Antonio June 2002, pp. 524–527.
- [44] E. Suter and J. R. Mosig, “A subdomain multilevel approach for the efficient mom analysis of large planar antennas,” *Microwave Optical Techn. Lett.*, vol. 26, no. 4, pp. 270–277, 2000.
- [45] G. Cui, S.-G. Zhou, G. Zhao, and S.-X. Gong, “A compact dual-band dual-polarized antenna for base station application,” *Progress In Electromagne. Rese.*, vol. 64, pp. 61–70, May 2016.
- [46] A. Ahlbom, U. Bergqvist, J. Bernhardt, J. Cesarini, M. Grandolfo, M. Hietanen, A. Mckinlay, M. Repacholi, D. H. Sliney, J. A. Stolwijk *et al.*, “Guidelines for limiting exposure to time-varying electric, magnetic, and electromagnetic fields (up to 300 GHz),” *Health physics*, vol. 74, no. 4, pp. 494–521, 1998.
- [47] Z. Zaharis, “Radiation pattern shaping of a mobile base station antenna array using a particle swarm optimization based technique,” *Electrical Engineering*, vol. 90, no. 4, pp. 301–311, 2008.

- [48] V. Degli-Esposti, G. Riva, and N. Binucci, "Derivation of antenna pattern shaping criteria for urban base stations using ray tracing," *IEEE Trans. Vehicular Techn.*, vol. 52, no. 6, pp. 1686–1688, Nov. 2003.
- [49] X. Dardenne, "Method of moments simulation of infinite and finite periodic structures and application to high-gain metamaterial antennas," *PhD Thesis*, 2007.
- [50] J. Hansen, *Spherical near-field antenna measurements*. London, U.K.: P. Peregrinus on behalf of the Institution of Electrical Engineers, 1988.
- [51] J. Laviada, M. R. Pino, and F. Las-Heras, "Characteristic spherical wave expansion with application to scattering and radiation problems," *IEEE Antennas and Wireless Propagation Letters*, vol. 8, pp. 599–602, 2009.
- [52] H. Gauthier, "Auxiliary radiators for human exposure reduction in cellular networks," Master's thesis, UCLouvain, Belgium, 2015.
- [53] M. F. Catedra, J. Perez, F. S. de Adana, and O. Gutierrez, "Efficient ray-tracing techniques for three-dimensional analyses of propagation in mobile communications: application to picocell and microcell scenarios," *IEEE Antennas Propag. Mag.*, vol. 40, no. 2, pp. 15–28, Apr. 1998.
- [54] M. Nohrborg, "LTE." [Online]. Available: <http://www.3gpp.org/technologies/keywords-acronyms/98-lte>
- [55] E. Arvas, A. Rahhal Arabi, A. Sadigh, and S. M. Rao, "Scattering from multiple conducting and dielectric bodies of arbitrary shape," *IEEE Antennas and Propagation Magazine*, vol. 33, no. 2, pp. 29–36, April 1991.
- [56] A. Guissard, "On the surface field integral equations," *IEEE Transactions on Education*, vol. 46, no. 4, pp. 486–496, 2003.
- [57] C. Geuzaine and J.-F. Remacle, "Gmsh." [Online]. Available: <https://gmsh.info>

- [58] isola, “I-Tera MT RF very low-loss laminate material,” 2018, Data Sheet. [Online]. Available: <https://www.isola-group.com/wp-content/uploads/data-sheets/i-tera-mt40-rfmw.pdf>
- [59] Y. Miao, Q. Gueuning, and C. Oestges, “Modeling the phase correlation of effective diffuse scattering from surfaces for radio propagation prediction with antennas at refined separation,” *IEEE Trans. Antennas Propag.*, vol. 66, no. 3, pp. 1427–1435, March 2018.
- [60] A. Kausar, H. Mehrpouyan, M. Sellathurai, R. Qian, and S. Kausar, “Energy efficient switched parasitic array antenna for 5G networks and IoT,” in *Loughborough Antennas Propag. Conf. (LAPC)*, Nov. 2016, pp. 1–5.
- [61] P. Lotfi, S. Soltani, and R. D. Murch, “Broadside beam-steerable planar parasitic pixel patch antenna,” *IEEE Transactions on Antennas and Propagation*, vol. 64, no. 10, pp. 4519–4524, 2016.
- [62] A. Foroozesh and L. Shafai, “Investigation into the effects of the patch-type FSS superstrate on the high-gain cavity resonance antenna design,” *IEEE Trans. Antennas Propag.*, vol. 58, no. 2, pp. 258–270, Feb. 2010.
- [63] M. Kirschning, R. H. Jansen, and N. H. L. Koster, “Accurate model for open end effect of microstrip lines,” *Electronics Letters*, vol. 17, no. 3, pp. 123–125, February 1981.
- [64] HUBER+SUHNER, “Flexible RF cable RG316/U,” 2019, Data Sheet. [Online]. Available: <https://ecatalog.hubersuhner.com/product/E-Catalog/Radio-frequency/Cables/RG.316.-U>
- [65] B. V. Ha, C. Craeye, and S. N. Jha, “A fast full-wave analysis scheme of high-gain superstrate antennas,” in *IEEE Int. Symp. Antennas Propag.*, Jul. 2015, pp. 969–970.
- [66] S. N. Jha, B. V. Ha, and C. Craeye, “Fast MBF analysis of printed FSS structures,” in *IEEE Int. Symp. Antennas Propag.*, Jul. 2015, pp. 959–960.

- [67] J. I. Echeveste, “New methods for the synthesis of radiation patterns of coupled antenna arrays,” *PhD Thesis*, 2016.
- [68] B. Fuchs, “Application of convex relaxation to array synthesis problems,” *IEEE Trans. Antennas Propag.*, vol. 62, no. 2, pp. 634–640, Feb 2014.
- [69] D. Rodrigo, E. Diaz, and L. Jofre, “Reconfigurable pixel-layer isolator for frequency-tunable on-frequency repeaters,” *IEEE Antennas and Wireless Propagation Letters*, vol. 13, pp. 475–478, 2014.
- [70] S. Hubert, “Numerical analysis of strongly coupled antenna arrays,” *PhD Thesis*, 2018.
- [71] K. A. Michalski and D. Zheng, “Electromagnetic scattering and radiation by surfaces of arbitrary shape in layered media. i. theory,” *IEEE Trans. Antennas Propag.*, vol. 38, no. 3, pp. 335–344, March 1990.
- [72] K. A. Michalski and J. R. Mosig, “Multilayered media green’s functions in integral equation formulations,” *IEEE Trans. Antennas Propag.*, vol. 45, no. 3, pp. 508–519, March 1997.
- [73] D. M. Pozar and D. H. Schaubert, “The analysis and design of microstrip antennas and arrays,” *A Selected Reprint Volume. IEEE Antennas and Propagation Society Sponsor. New York*, 1995.
- [74] D. Pozar and D. Schaubert, “Analysis of an infinite array of rectangular microstrip patches with idealized probe feeds,” *IEEE Trans. Antennas Propag.*, vol. 32, no. 10, pp. 1101–1107, October 1984.
- [75] ———, “Scan blindness in infinite phased arrays of printed dipoles,” *IEEE Trans. Antennas Propag.*, vol. 32, no. 6, pp. 602–610, June 1984.
- [76] H. D. Young and R. A. Freedman, “Sears and zemansky’s university physics (vol. 1),” 2008.
- [77] Z. Sipus, P.-S. Kildal, R. Leijon, and M. Johansson, “An algorithm for calculating green’s functions of planar, circular cylindrical, and spherical multilayer substrates,” *Applied Computational Electromagnetics Society Journal*, vol. 13, pp. 243–254, 1998.

- [78] D. Pozar and S. Voda, "A rigorous analysis of a microstripline fed patch antenna," *IEEE Trans. Antennas Propag.*, vol. 35, no. 12, pp. 1343–1350, December 1987.